Electron Spin Resonance of Molecular Magnets for Quantum Information Processing

Danielle Kaminski
Magdalen College

A thesis submitted for the degree of Doctor of Philosophy
at the University of Oxford
Trinity Term 2015

Electron Spin Resonance of Molecular Magnets for Quantum Information Processing

DANIELLE KAMINSKI
Magdalen College, University of Oxford
D.Phil Thesis, Trinity Term 2015

Abstract

Quantum information processors have been shown theoretically to outperform their classical counterparts at certain tasks. They comprise two level systems, which can exist in an arbitrary superposition of states: qubits. A strong candidate qubit is the molecular nanomagnet (MNM). In this thesis, electron spin resonance is used to explore the potential of Cr_7M based MNMs as elements of a quantum information processor.

We explore the possibility and effect of replacing H atoms with D or a halogen atom in a $S = 1/2$ Cr_7Ni ring. Decoherence mechanisms in the resulting compounds are found to be dominated by structural effects. We conclude that halogenation does not seem to be a productive strategy for extension of coherence times in Cr_7Ni based compounds.

We examine an asymmetric dimer, in which a Cr_7Ni ring is linked to a highly coherent nitrogen atom within a carbon cage. Measurement of phase memory time across a range of temperatures for the N spin, provides insight into the ring's spin dynamics. At high temperature, fluctuations on the ring are so rapid that the N spin appears magnetically disconnected; as they slow, we see a sharp rise in the decoherence rate of the N spin. At the lowest temperatures, a recovery of the decoherence rate reflects the onset of the ring's coherent ground state.

A group of symmetric Cr_7Ni-Cr_7Ni dimers is investigated. Through use of double electron-electron resonance, the strength of the ring-ring dipolar interaction, governing the two qubit gate time, is estimated for each. It is found that many exhibit the hierarchy of timescales required for implementation of a two qubit gate: a short single qubit manipulation time, intermediate two-qubit gate time and long phase coherence time. A possible scheme for the future implementation of a CNOT gate is presented.

The final study explore rings of spin, $S > 1/2$. We present the first ever coherent measurements on a dilute oriented ensemble of the $S = 3/2$ rings, Cr_7Zn, performing nutations at various powers. In addition, we investigate the anisotropic Mn^{2+} ($s = 5/2$, $I = 5/2$) defect in ZnO. We develop the 'echo kill' method for identification of a three level subsystem whose transition frequencies both fall within the cavity bandwidth. Such a subsystem is then used to perform indirectly detected nutations between the upper two levels over a range of applied powers. Finally, a method for initialisation of the subsystem into a pseudopure state is presented and shown to enhance nutation amplitude.

Acknowledgements

There are so many people who have contributed so much to my time in Oxford that I cannot possibly name them all. But, I will try to make a start.

I would like to thank my supervisor, Arzhang, for first sparking my interest in this project and for inspiring me to come to Oxford. I thank him for being a constant source of insight, ideas, and enthusiasm, and for teaching me so much about so many things. Without him, this thesis would not have been possible.

I thank everyone who has taken the time to help and teach me in the lab. For sharing their vast knowledge on the Bruker spectrometers, I thank Jeffrey Harmer and Will Myers and for introducing me to the Chemistry lab I thank Ben Farrington. I would not have survived any of my experiments in the first year without Amy Webber, whose support, encouragement and guidance was invaluable. I thank Junjie Liu who has helped me with so many aspects of my work, both in and out of the lab. He has been a great source of support over the last three years. For teaching me how to run a DEER experiment, and for her support in the lab, I thank Alice Bowen.

For the beautiful samples, I am grateful to Grigore Timco and I thank both Richard Winpenny and Eric McInnes for answering all my questions about molecular magnets and for making me feel so welcome in Manchester.

Life in the Clarendon has been made by the people around me. Firstly, I thank 'the lads' in 106, who have made it such a great place to be: Dave Keen, for supplying us all with his wisdom, Jack, for the 'football phrases', Sungkyun for the 'zingers', Alun, for the tasteful postcards, triolade and endless life advice, Franz, for the salsa and Craig, for showing so much enthusiasm for my page count commentary. I am grateful to Jordan Thompson for coming to my rescue in times of moths, melting, sample loss and chocolate shortage and to everyone who helped on my infamous 'day in the trash'. I thank Maria, Jorge and Paulo for many interesting discussions and for keeping my Spanish in good practice. For making the many tea times, lunches and pub trips so special I am grateful to everyone I have shared these with, in particular, Ben, Liam, Matt, Tash, Sam, Arjun,

Alex, Marein, James, Ivelisse, Paul, Rog, Pete, Steve, Bill, Andrew, Moon-Sun, and so many more who I hope will forgive me for not naming them. For the thesis playlist, I thank Beyoncé and Rihanna (and Franz for putting up with it!).

I would not have made it through the last four years without my friends and family. For the Maxwells nights and Holywell dinners, I thank the 'Magdalen crew'. For so many fun escapes, I am grateful to Hayley, Fran, Tom and 'the girls'. Oxford would not have been the same without my fellow Northerner, Heather and our many hot chocolate, macaron and Nando's nights. Finally, I thank Noah, for making my final year in Oxford the happiest, and my Mum and Dad, without whose love and support I wouldn't have even made it here.

Contents

Chapter 1

Introduction

Since its initial development during World War II, the electronic digital computer has gone from occupying an entire room to a circuit board on the order of square centimetres, and has revolutionised almost every aspect of our lives. As its components reach ever shorter length scales, the effects of quantum mechanics are becoming increasingly important. Many modern devices utilise these to their advantage, however, the algorithms they perform are still classical. Theoretical proposals have demonstrated the potential power of quantum algorithms to solve some problems more efficiently and work is now underway to build instead a quantum computer: the main motivation for this thesis.

1.1 Quantum Information Processing (QIP)

A classical computer is composed of bits: two level systems, which occupy either state, for example $|0\rangle$ or $|1\rangle$, at a given time. A quantum computer, on the other hand, is composed of qubits: two level systems, which as well as either state, can occupy a superposition of the two, giving

$$|\psi\rangle = \alpha|0\rangle + \beta|1\rangle, \tag{1.1}$$

where α and β are complex coefficients and $|\alpha|^2 + |\beta|^2 = 1$. Figure 1.1 allows us to visualise this difference; a bit can access only the poles ($|0\rangle$ or $|1\rangle$) whereas to a qubit,

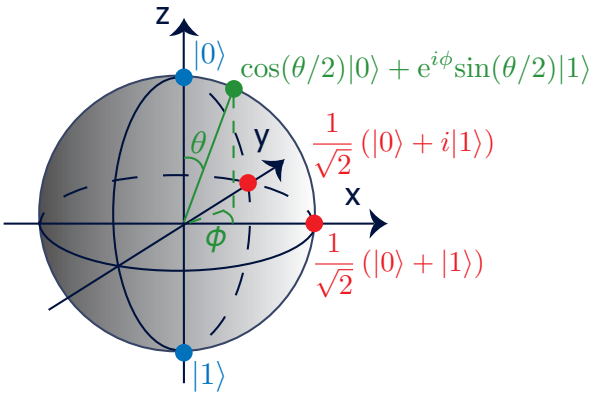

FIGURE 1.1: Visualisation of a two level system of states $|0\rangle$ and $|1\rangle$ on the Bloch sphere.

the Bloch sphere's entire surface is opened up. For a given θ and ϕ, the qubit's state is then described by

$$|\psi\rangle = \cos(\theta/2)|0\rangle + \mathrm{e}^{i\phi}\sin(\theta/2)|1\rangle. \tag{1.2}$$

If we now consider two bits or qubits, the former can occupy any of the four states $|00\rangle$, $|01\rangle$, $|10\rangle$, $|11\rangle$, whereas the latter can also occupy a superposition of these, such that the general state is

$$|\psi\rangle = \alpha_{00}|00\rangle + \alpha_{01}|01\rangle + \alpha_{10}|10\rangle + \alpha_{11}|11\rangle. \tag{1.3}$$

Here, α_x are complex coefficients and $\sum_{x\in\{0,1\}^2} |\alpha_x|^2 = 1$. A notable example is one of the so-called Bell states:

$$|\psi\rangle = \frac{|00\rangle + |11\rangle}{\sqrt{2}}. \tag{1.4}$$

In this case, collapse of the wavefunction ensures that if we measure the first qubit and obtain a 0, we will also obtain a 0 from an immediately subsequent measurement of the second qubit; we say that measurement of their states is correlated or that they are *entangled*. This is a uniquely quantum phenomenon, of central importance to many

proposed quantum algorithms. More generally, an n-qubit system is described by 2^n complex coefficients [1].

The first theoretical model of a quantum computer, utilising these properties, was proposed by Deutsch in 1985 [2]. Subsequently, Shor demonstrated its theoretical ability to provide efficient (requiring time which scales polynomially with input size) solution to two problems in particular: that of prime factorisation and the 'discrete logarithm' problem [3]. With these classically intractable problems at the core of many widely used systems of public key encryption, for example RSA, the consequences of a successful physical implementation of this work, would be huge [4]. Grover has further shown a quantum computer to search more efficiently through an unsorted data set, something of increasing importance as we enter the era of 'big data' [5]. The quantum computer would, in addition, be an invaluable tool with which to simulate complex quantum systems, as envisaged by Feynman in 1982 [6, 7].

1.1.1 Physical Implementation

In order to build successfully a quantum computer, we need a system of well defined qubits enabling us to satisfy certain key physical requirements [8, 9]:

1. Scalability; a linear increase in system size must not necessitate an exponential increase in resources.
2. Ability to initialise the system into a known state.
3. Coherence; the system must remain coherent for a time significantly longer than both the single qubit manipulation time and the two qubit gate time.
4. Existence of a universal set of quantum gates.
5. Capability to perform qubit specific measurements.

Exploration of these has led to the proposal of a wide range of physical architectures, exhibiting varied combinations of strengths [1, 10]. However, one must often make a trade-off between different requirements, for example strong coupling to the environment

offers a pathway for manipulation, but can at the same time increase decoherence. With the relative importance of each physical requirement dependent upon specific component function, for example memory in particular requiring a very long coherence time, we can imagine any functional quantum computer might readily comprise several different physical implementations of the qubit.

Potential architectures include trapped ions, with which the formation of entangled states with >99% fidelity is now possible but for which scalability remains challenging [11]; photons, making use of their orthogonal polarisation states [12–14]; and, although still mainly consisting of theoretical research, certain topological states of matter, for example, the Majorana fermion [15, 16]. In recent years, particular promise has been shown by superconducting circuits. These are based on the electrical LC harmonic oscillator, with a degree of anharmonicity introduced by a Josephson tunnel junction to allow transition selective excitation [17]. Modification of both the circuit components and their configuration provides flexibility and superconducting circuits show coherence times on the order of 100 μs [18]. Their progress is aided by an existing wealth of circuit fabrication techniques developed by the semiconductor industry. Perhaps the most obvious choice of qubit, and one of the first systems to be investigated, is spin: the subject of the next section.

1.1.2 Spin as a Qubit

Spin first found use in computers with the discovery of the giant magnetoresistive (GMR) effect: that the electrical resistance met by current passing through two ferromagnetic (FM) layers separated by a non magnetic spacer (figure 1.2a), is dependent upon the relative FM magnetisation direction. This arises due to spin dependent scattering; in the antiparallel configuration, both up and down spins are scattered, whereas the parallel configuration allows the spin component aligned with the layers to pass relatively unhindered, leading to a lower overall resistance [19]. Antiparallel resistance values up to 110% higher than their parallel counterparts have been observed at room temperature [20]. The configuration shown in figure 1.2a is known as a 'spin valve' and is used in read heads to detect small magnetic fields [21]. With one FM layer 'pinned' and the

other field dependent, the relative magnetisation direction and resistance are determined by the magnetic field, allowing the device to act as a detector. A similar effect is observed with an insulting spacer, in the tunnel magnetoresistance (TMR) configuration (fig 1.2b) [22]. In this case, the probability of quantum tunnelling depends upon the relative FM orientation and has led to antiparallel resistances up to 600% higher than their parallel counterparts at room temperature [23]. Utilisation of the spin degree of freedom became known as 'spintronics' and the field was opened up by these devices [21, 24].

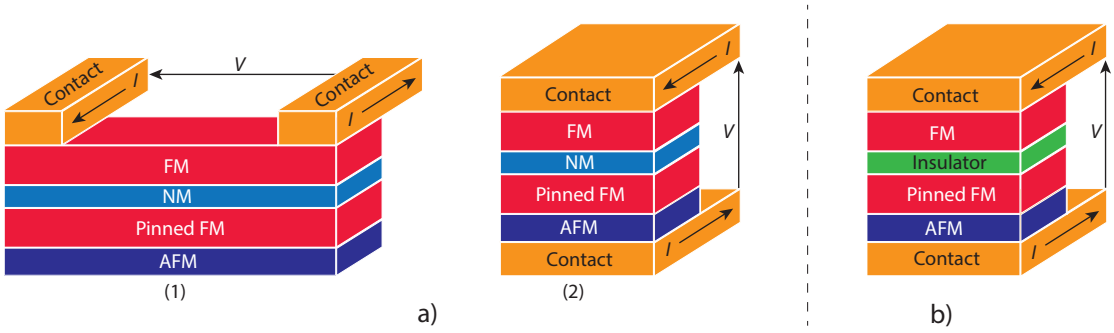

FIGURE 1.2: Schematics of GMR (a) and TMR (b) devices. Layers are ferromagnetic (FM), non magnetic (NM), insulating, anti ferromagnetic (AFM) or ferromagnetic and pinned to the AFM layer (Pinned FM). For a GMR device, two configurations are possible, with current either parallel (1) or perpendicular (2) to the layers.

Use of spin as a qubit requires utilisation not only of the spin up and down states but also their coherent superpositions: 'quantum spintronics'. A number of candidate spin qubits has been explored, for example quantum dots, for which a universal set of quantum gates was first proposed in 1998 [25]. These are zero dimensional systems on the mesoscopic length scale (typically ∼10-100 nm), in which electrons can be confined [26]. The confining potential results in a spectrum of allowed energy levels such that they are often referred to as 'artificial atoms' [9, 10]. Quantum dots fall into two main categories: those grown by the 'bottom up' approach of self assembly, such as InGaAs dots on GaAs (self assembled QDs), and those lithographically defined by electrical gates on the surface of a semiconductor heterostructure, for example GaAs/AlGaAs, containing a two dimensional electron gas (lateral QDs). Self assembled QDs are controlled optically and with both electron and hole spins, have been initialised with ≥99% fidelity [27–29]. They provide confinement on length scales shorter than lateral QDs, but are difficult to scale due to their random positions, resulting from the method of growth [30]. In contrast,

lateral QDs are controlled via magnetic resonance techniques and are in principle more scalable. Both types show coherence times on the order of microseconds [26].

Nuclear spin populations, manipulated by nuclear magnetic resonance (NMR), were one of the first systems to be explored [31]. A static magnetic field is applied in order to Zeeman split the nuclear energy levels and radio frequency pulses drive transitions between them. Spins residing on different nuclei or in differing chemical environments, have different resonant frequencies and are therefore in principle individually addressable. The plethora of existing NMR techniques made progress rapid and by 1998, NMR had been successfully used to implement two qubit quantum algorithms [32, 33]. Nuclear spins offer the advantage that they have minimal interaction with the environment and therefore show very long coherence times, often on the order of seconds at room temperature [33, 34]. However, their low magnetic moments, resulting in level splittings on the order of 100 MHz with a typical NMR Zeeman field of 10 T, lead to a very small population excess in the lower energy spin state, such that signals are very weak [35]. This further limits their potential for entanglement [36–38]. Additionally, in order to address individual qubits, the bandwidth of each pulse must be sufficiently narrow that it does not excite multiple spins. With a finite width of potential resonant frequencies, and a maximal length and hence minimal width of applied pulses, a limit on scalability is encountered [39].

Eager to overcome the problems associated with NMR, researchers turned instead to electron spin resonance (ESR), discussed in detail in chapter 2. With the electron's approximately 10^3 times larger magnetic moment, spin population differences in a typical ESR Zeeman field of 1 T are much greater than in an NMR experiment and can be manipulated on a timescale approximately 10^3 times faster. Given their stronger interaction with the environment, however, electron spins in general show coherence times shorter than nuclear spins.

Offering populations of identical qubits and accessible modelling, a strong category of electron spin qubit candidate is atomic defects. An example, motivated by the potential for integration into existing silicon-based technologies, is the ^{31}P donor in silicon. Silicon's low spin-orbit coupling and naturally low abundance of nuclear spin carrying

isotopes, result in long coherence times, reaching 10 s at 1.8 K [40]. Recent advances have coherently transferred a superposition state from the ^{31}P electron to its nuclear spin, aiming to take advantage of the nuclear spin's extended coherence time for storage, and have entangled the ^{31}P electron and nuclear spins [36, 41]. A further example is the Mn(II) defect in ZnO, whose electric field dependent zero field splitting has allowed it to be addressed not only magnetically, but also electrically [42]. Some defects even show promise of operation at room temperature, for example the optically addressable nitrogen-vacancy centre (a missing carbon adjacent to one replaced with a nitrogen atom), in diamond [43, 44]. An emerging cheaper alternative is the divacancy in silicon carbide [45, 46].

While the above atomic defects offer nominally identical qubits with long coherence times, they do not have structural degrees of freedom, therefore, modification is difficult. In addition, their length scale is such that gating to individual qubits would be extremely challenging and scalability is brought into question. In 2001, a scheme was proposed for the implementation of Grover's search algorithm on a different type of electron spin, that of a molecular magnet, a highly tuneable mesoscopic spin, to be examined in the next section [47].

1.2 Molecular Magnetism

It was first thought that magnetism was confined to metallic or ionic solids, involving d- and f- block electrons. When the first demonstration of electrical conduction through an organic molecule was made, it was asked whether such molecules might also show magnetic effects [48, 49]. While most organic radicals, which carry at least one unpaired electron, are unstable, the nitroxide radical ($ONCNO^-$), with its single unpaired spin delocalised over all five atoms, is not and it was the nitroxide based molecule shown in figure 1.3, which, at temperatures below 0.65 K, became the first compound involving only s- and p- electrons to show ferromagnetism [50].

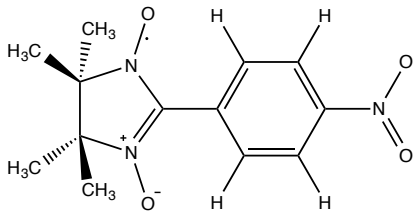

FIGURE 1.3: The first purely organic molecule, para-nitrophenyl nitronyl nitroxide (NIT_pNO_2Ph), to show ferromagnetism, evident at temperatures below 0.65 K [50].

It is also possible to combine organic molecules with the d- and f- block elements more traditionally associated with magnetism, utilising the tunability arising from the chemical synthesis of the former and the magnetic properties of the latter, between which an exchange interaction is mediated by organic 'linkers'. A wide range of compounds has resulted, including many of quasi low dimensionality, in which the exchange interaction between magnetic elements is much stronger in one (quasi 1D) or two (quasi 2D) dimension(s) than the other(s) [51–56]. They are often easier to synthesise than molecular materials with strong interactions in three dimensions due to the low symmetry and weak intermolecular interactions of the organic building blocks [48]. In some cases, dimensionality can even be tuned, modifying chemically the organic linkers thereby tuning the exchange interaction [57]. Such quasi low dimensional compounds are highly useful in testing aspects of the quantum theory of magnetism such as the so-called Goodenough-Kanamori-Anderson rules, and act as a test bed for examining strongly correlated physics such as that underlying high T_c superconductivity [58–60].

1.2.1 Molecular Nanomagnets

The molecular magnets of most interest to us in QIP are those of zero dimension, known as molecular nanomagnets (MNMs). MNMs are clusters of exchange coupled metal ions in an organic framework, on a typical length scale of ∼1-4 nm [61]. They often carry a large effective spin and show a substantial Ising type anisotropy (figure 1.4). As a result, with thermal activation frozen out, the magnetisation relaxes very slowly at low temperature. This occurs via quantum tunnelling of the magnetisation (QTM) through the anisotropy barrier (figure 1.4(a)), making MNMs one of the largest objects to exhibit this purely quantum mechanical effect [62–64]. As such, they have gained

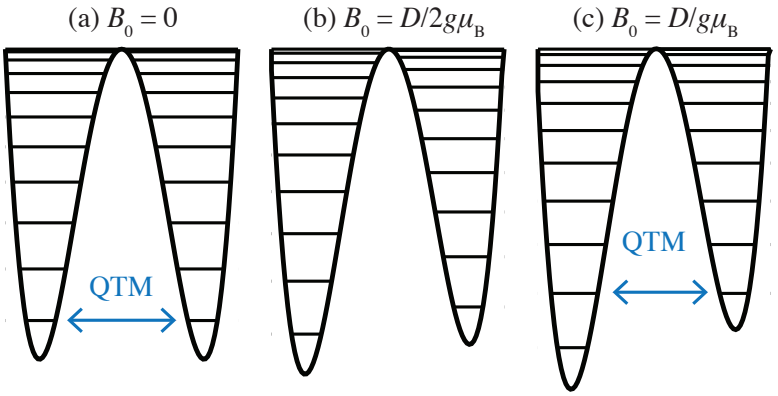

FIGURE 1.4: Energy levels for a MNM in magnetic field, B_0, with Hamiltonian $H = DS_z^2 + g\mu_B B_0 S_z$ and $D < 0$. The blue arrow shows the path of quantum tunnelling of the magnetisation (QTM) when $B_0 = 0$. Adapted from [49].

additional interest as probes of the quantum to classical crossover regime. Figure 1.5 shows the Mn_{12} based core of the first MNM in which QTM was observed. The eight Mn^{3+} ions of spin $s = 2$ (red) couple antiferromagnetically to the four Mn^{4+} ions (green) of spin $s = 3/2$. The type of exchange interaction within each group has been the subject of debate, however recent work has provided evidence in support of an antiferromagnetic interaction [67–69]. The molecule has a resulting total ground state spin of $S = 10$ and an anisotropy barrier of about 1,500 GHz [65, 66].

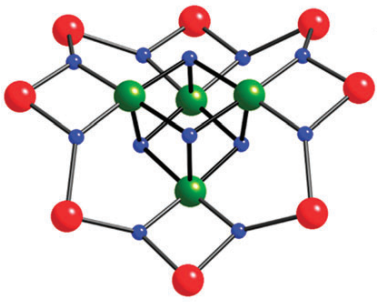

FIGURE 1.5: Mn_{12} core of the compound $[Mn_{12}O_{12}(O_2CMe)_{16}(H_2O)_4]$. The coloured balls represent either Mn^{3+} (red), Mn^{4+} (green) or O (blue). Adapted from [66].

There has also been synthesised a number of molecular MNMs consisting of a single magnetic ion in an organic framework, known as 'single-ion magnets', which exhibit the same slow relaxation of magnetisation as the polynuclear clusters [70–72]. Of particular interest are those based on the lanthanide ion, whose unquenched orbital degree of freedom leads to a high anisotropy barrier [73].

1.2.2 Spin Hamiltonians

Even the smallest of MNMs are highly complex to model, comprising large numbers of both magnetic and non magnetic constituents, often both contributing to the resulting magnetic properties of the molecule. Some small examples, in which symmetry permits simplification of the problem, can be modelled via ab initio methods, for example density functional theory, however in most cases this would require computational power beyond that available [74].

Simplification is provided by the 'Spin Hamiltonian Formalism', a very useful tool, which allows us to interpret data from MNMs. Within this framework, we consider the system's spin degrees of freedom only, with all other effects, including orbital degrees of freedom and electrostatic interactions with neighbouring atoms, absorbed into a set of phenomenological parameters. The model makes a number of assumptions, in particular that the orbital moment of magnetic constituents is essentially quenched and can be treated as a perturbation, and while these are often fair, leading to successful data interpretation, we must bear in mind that this is not always the case [48]. For a system of N individual electron spins, $\boldsymbol{s}_i$, the resulting Hamiltonian is given by equation 1.5.

$$H = \sum_{i=1}^{N} \boldsymbol{s}_i \cdot \boldsymbol{D}_i \cdot \boldsymbol{s}_i + \sum_{i<j} \boldsymbol{s}_i \cdot \boldsymbol{J}_{ij} \cdot \boldsymbol{s}_j + \mu_{\mathrm{B}} \boldsymbol{B}_0 \cdot \sum_{i=1}^{N} \boldsymbol{g}_i \cdot \boldsymbol{s}_i \tag{1.5}$$

The first term sums the individual zero field splittings, reflecting the strength and symmetry of the crystal field experienced by each spin. The splitting for spin, $\boldsymbol{s}_i$ is characterised by the rank two tensor, $\boldsymbol{D}_i$, and by choice of suitable axes can be expressed in the alternative form $D_i s_{z,i}^2 + E_i(s_{x,i}^2 - s_{y,i}^2)$, where $-1/3 < E_i/D_i < 1/3$. In the case of axial symmetry, $E_i = 0$. $D_i < 0$ then indicates an easy axis 'Ising type' anisotropy, such that $m_{s,i}$ states of greater magnitude are energetically preferable and $D_i > 0$ points to an easy plane anisotropy, such that the converse is true.

The second term accounts for interaction between spins, with $\boldsymbol{J}_{ij}$ a rank two tensor. It can be broken up conveniently into the sum of three parts: the 'isotropic exchange' or 'Heisenberg' interaction, $\sum_{i<j} -J_{i,j} \boldsymbol{s}_i \cdot \boldsymbol{s}_j$, which acts to align the two relevant

spins either parallel or antiparallel to each other; the 'anisotropic symmetric' term, $\sum_{i<j} \boldsymbol{s}_i \cdot \boldsymbol{D}_{i,j} \cdot \boldsymbol{s}_j$, with $\boldsymbol{D}_{i,j}$ diagonal for suitably chosen axes, which states a directional preference for the axis of alignment in space; and the 'anisotropic antisymmetric' or 'Dzyaloshinskii-Moriya' interaction, $\sum_{i<j} \boldsymbol{d}_{i,j} \cdot \boldsymbol{s}_i \times \boldsymbol{s}_j$, which acts to tip the spins by 90° to each other.

The final term represents the electron Zeeman interaction, which gives an energetic preference to the alignment of the spin magnetic moment with the applied magnetic field, $\boldsymbol{B}_0$. The rank two tensor $\boldsymbol{g}_i$, which is usually symmetric and therefore diagonalisable, quantifies the strength of this, taking account both of spin-orbit coupling and the spin's magnetic environment.

We have neglected here the effect of hyperfine interaction with nuclear spins. For most MNMs, this manifests itself in ESR spectra in two main ways: the first is a broadening in energy of the resonant transition, which we term 'unresolved hyperfine broadening'. Line splittings are not observable directly due to the strength of the anisotropy being greater than that of any hyperfine interaction. The second is the effect known as electron spin echo envelope modulation, which will be introduced in section 2.2.7.

Despite vast simplification of the problem, the spin Hamiltonian is by no means easy to solve. With $(2s_i + 1)$ energy levels per spin, the Hamiltonian spans a Hilbert space of $\prod_{i=1}^{N}(2s_i + 1)$ dimensions. However, in the 'strong exchange' limit (frequently valid for MNMs), where the isotropic exchange term is dominant, we can simplify it further. Given that the total spin operator $\boldsymbol{S}^2$, where $\boldsymbol{S} = \sum_{i=1}^{N} \boldsymbol{s}_i$, commutes with the isotropic exchange term, we find that, in the first approximation, S is a good quantum number [75]. This allows us to group eigenstates into 'exchange multiplets' of well defined S, treating all other terms as perturbations, which act within the multiplet. In the case that exchange is strong, giving a separation of the two lowest energy multiplets of greater than the splittings within them, we may at low enough temperature assume that the ground state only is populated. The entire system may now be represented by the Hamiltonian,

$$H = DS_z^2 + E(S_x^2 - S_y^2) + \mu_{\mathrm{B}} \boldsymbol{B}_0 \cdot \boldsymbol{g} \cdot \boldsymbol{S}, \tag{1.6}$$

in which S is the spin of the ground state multiplet, and we assume levels within it to be thermally populated. The first two terms represent the axial and rhombic zero field splittings respectively, and the final term the electron Zeeman interaction. We have neglected higher order spin anisotropy terms, which are sometimes necessary, for example to account for mixing with spin states of different S due to the anisotropic interactions [76]. This is the 'giant spin approximation' (GSA), highly applicable for many MNMs, and will be used frequently throughout this thesis.

1.2.3 Cr_7M Antiferromagnetic Rings

The set of compounds upon which this thesis will focus are based on the parent compound, Cr_8 (figure 1.6(a)) [77, 78]. This has a magnetic core consisting of a ring of eight antiferromagnetically coupled Cr^{3+} ions, each of spin $s_i = 3/2$, such that in the ground state, within the GSA, the total spin, $S = 0$ and the compound is diamagnetic (figure 1.6(b)). Each magnetic ion is octahedrally coordinated, bridged to each neighbouring ion by one fluoride and two bulky carboxylate ligands, such as the pivalate ($(CH_3)_3CCO_2^-$) or acetate ($CH_3CO_2^-$) variants (figure 1.6(a)). These provide both structure and rigidity to the molecule and mediate the exchange interaction. However, with a ground state $S = 0$, the ring does not provide any spin from which to form our qubit.

The solution to this problem is provided by the daughter class of compounds based instead on the magnetic ring Cr_7M, where M is a divalent metal ion (figure 1.6(c, d)). Synthesised from $Cr_8F_8Piv_{16}$, the ring inherits the parent structure, but with an additional central 'templating cation' in order to neutralise the ring's charge of -1 (figure 1.6(c)) [79, 80]. Exchange coupling within the ring remains antiferromagnetic, leading to a range of potential ground state spins, governed by the choice of M. Table 1.1 presents a selection of these.

Figure 1.7 shows the zero field energy spectrum of the twelve lowest lying exchange multiplets for each of the tabulated rings (assuming Cr_7Zn to be magnetically equivalent to Cr_7Cd), derived from measurement of magnetic susceptibility as a function of temperature. We note that there is in all cases a large energy separation between the ground and first excited states, thereby validating our use of the GSA at sufficiently low temperature

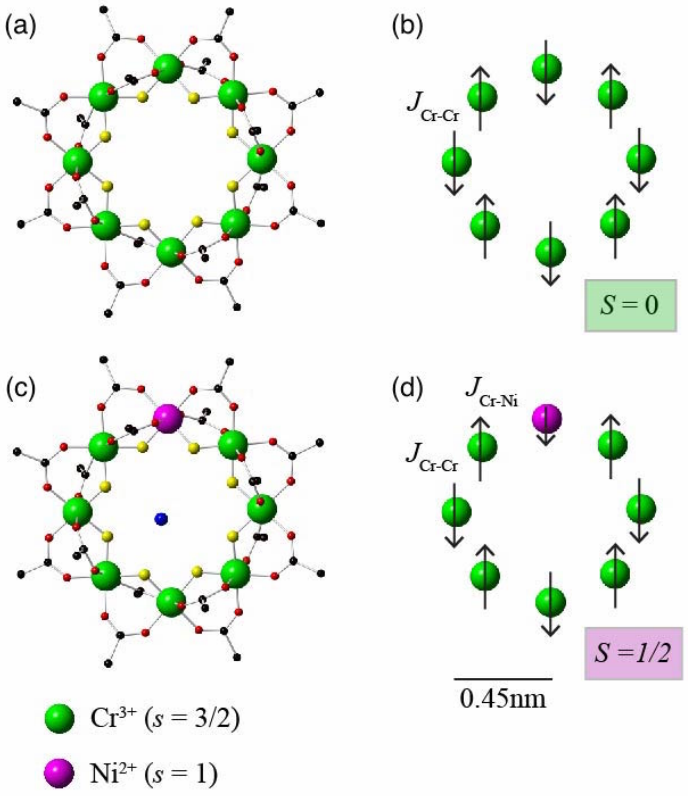

FIGURE 1.6: (a) and (c) show the structures of the MNMs $Cr_8F_8Ac_{16}$ and $Cr_7NiF_8Ac_{16}Cs$ respectively. The coloured balls represent Cs (green), Ni (pink), F (yellow), O (red), C (black) and Cs (blue). Hydrogen atoms are omitted for clarity. (b) and (d) show the respective magnetic cores of effective spin S, governed by the isotropic exchange constants, J_{ij}.

TABLE 1.1: Example ground state spins of a Cr_7M ring [81].

Metal, M	Electron Spin of M^{2+}	Ground State Spin of Cr_7M
Cd	0	3/2
Zn	0	3/2
Mn	5/2	1
Ni	1	1/2

and applied magnetic field. The spectrum can be verified and refined through use of inelastic neutron scattering, which probes directly the energy gaps [82, 83]. A beam of monochromatic neutrons is incident upon the sample and scattered in accordance with the selection rules $\Delta S = 0, \pm 1$ and $m_S = 0, \pm 1$. This can be done at either zero or finite applied static magnetic field. Parameters within the ground and first few excited state multiplets can be obtained via multi frequency electron spin resonance (the subject of chapter 2), fitting each multiplet to equation 1.6.

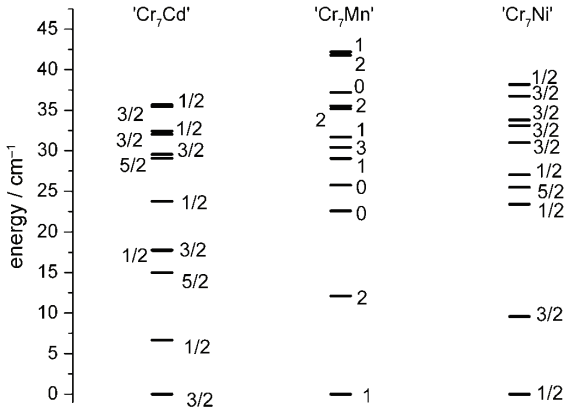

FIGURE 1.7: The zero field energy spectrum of the twelve lowest lying exchange multiplets for Cr_7Cd (magnetically equivalent to Cr_7Zn), Cr_7Mn and Cr_7Ni. This was calculated using a spin Hamiltonian approach, assuming validity of the strong isotropic exchange limit. Isotropic exchange parameters used were $J_{Cr-Cd} = 0$ (since Cd^{2+} is diamagnetic) and $J_{Cr-Cr} = J_{Cr-Mn} = J_{Cr-Ni} = -173.1$ GHz as determined from variable temperature magnetic susceptibility data. Taken from [81, 83].

The chemical structure of Cr_7M rings is such that they can also be adapted to form two ring molecules or 'dimers', in which the rings are either chemically linked or 'threaded' onto a rigid axle to form a structure known as a rotaxane [84–86]. This type of molecule and the resulting coupling between the rings will be the subject of chapter 5. It has also been possible to link chemically a Cr_7Ni ring to a different type of spin: a nitrogen atom contained within a C_{60} or 'bucky ball' cage ($N@C_{60}$). This alternative type of dimer will be examined in chapter 4.

1.3 Molecular Nanomagnets as Qubits

The use of high spin, high anisotropy MNMs in quantum information processing was first proposed in 2001, when theoreticians recognised their potential to form dense quantum memories and proposed a scheme within which Grover's algorithm could be implemented [47, 87]. Instead of scaling the system to comprise multiple two-level qubits, this utilises the full ladder of m_S levels, split by a static magnetic field, B_0, in the ground state exchange multiplet of a MNM. Multiple coherent superposition states are formed within the ladder using coherent microwave pulses of varied frequency, which target specific 'rung to rung' transitions. This is made possible by the molecule's anisotropy, which lifts the degeneracy of transition energies for spins $S > 1/2$ (figure 1.8).

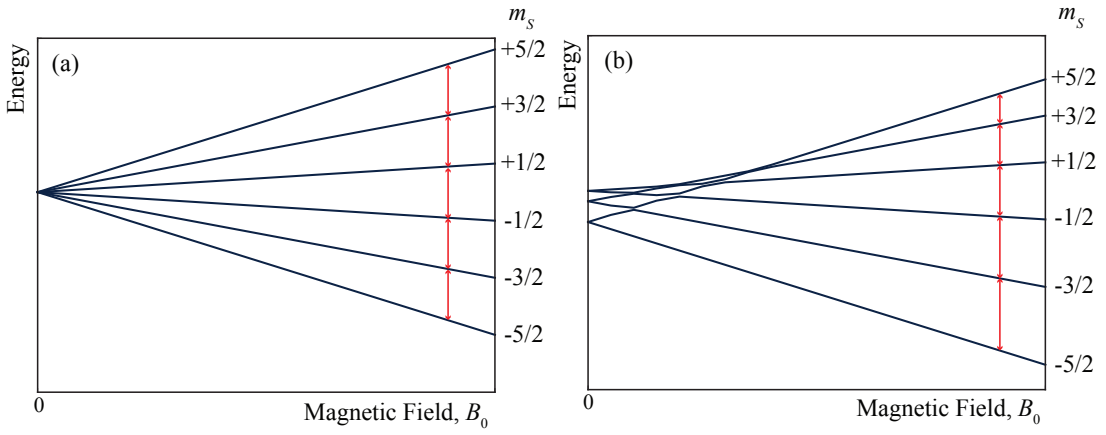

FIGURE 1.8: Energy levels for a MNM of ground state spin, $S = 5/2$ and Hamiltonian, $H = DS_z^2 + g\mu_B B_0 S_z$. In (a) $D = 0$ and in (b) $D < 0$. Allowed magnetic dipole transitions are marked in red, highlighting the lift in transition energy degeneracy from (a) to (b).

As discussed in section 1.1.1, a key requirement for any qubit is that it remains coherent on a timescale much greater than that required to perform both single qubit manipulations and two qubit gates. Despite much excitement about the potential use of MNMs in QIP, it was not until 2007 that this criterion was shown to be satisfied. ESR experiments revealed that the ground state spins of both Cr_7Ni and Cr_7Mn do in fact, at low temperature, have a coherence time greater than the single qubit manipulation time of approximately 10 ns [88]. The coherence time reached 3.8μs at 1.8 K for one Cr_7Ni based compound, in which the highly magnetic H nuclei had been replaced with D, in order to reduce decoherence. Decoherence mechanisms in Cr_7Ni rings will be examined in detail in chapter 3.

A major advantage of molecular systems in the field of QIP, is the ability we have to adapt chemically their structure, thereby fine tuning their properties [48]. Within the Cr_7M class of compounds alone, this has allowed us: to understand mechanisms of decoherence and extend coherence times; to build a group of structurally identical compounds within which spin is varied; and to form multiple ring 'superstructures' with the potential to act as multi qubit systems [79, 80, 83–86, 88, 89]. Furthermore, given the method of chemical synthesis used to construct molecular qubits, we obtain with ease a population of identical units, which was challenging in the field of quantum dots. Their mesoscopic length scale in addition gives promise for future single molecule manipulation.

1.4 Outline of Thesis

Throughout this thesis, electron spin resonance (ESR) will be used to explore the potential use of MNMs in the field of quantum information processing. Chapter 2 will begin by examining the technique itself, including both the relevant experimental and theoretical backgrounds. In chapter 3, the possibility and effect of replacing H atoms with D or a halogen atom in a Cr_7Ni ring will be examined in order to elucidate decoherence mechanisms. Chapter 4 will examine the fluctuations on a Cr_7Ni ring through the transition to order, by use of a $N@C_{60}$ probe spin. In chapter 5, measurements of the dipolar coupling between two Cr_7Ni rings in dimers will be presented. Chapter 6 will present the first coherent measurements on a dilute oriented ensemble of Cr_7Zn molecules. It will then present experimental measurements on a test system: Mn(II):ZnO, extending experimentation across three energy levels. Chapter 7 will conclude with a summary of the contributions this thesis makes to the use of single molecule magnets for quantum information processing.

Chapter 2

Electron Spin Resonance

Electron spin resonance (ESR) is a powerful technique applicable to compounds with an unpaired electron spin. It is used both to gain structural and dynamic information by probing the spin's energy level structure, and to manipulate spins within this structure, for purposes such as quantum information processing. In this chapter, we will explore the key principles behind the two main types of ESR experiment: continuous wave (CW) and pulsed, both of which will be used throughout this thesis.

2.1 Continuous Wave ESR

2.1.1 General Principles

Figure 2.1 shows the major components of a CW ESR experiment. We begin by applying a static magnetic field, B_0, in what we will define as the laboratory z-direction. All experiments in this thesis were carried out at 'X-band', such that this field was on the order 0.5 T and it was supplied by an electromagnet. Its effect is to add the Zeeman term,

$$H_{\mathrm{EZ}} = \mu_{\mathrm{B}} \boldsymbol{B}_0 \cdot \boldsymbol{g} \cdot \boldsymbol{s} \tag{2.1}$$

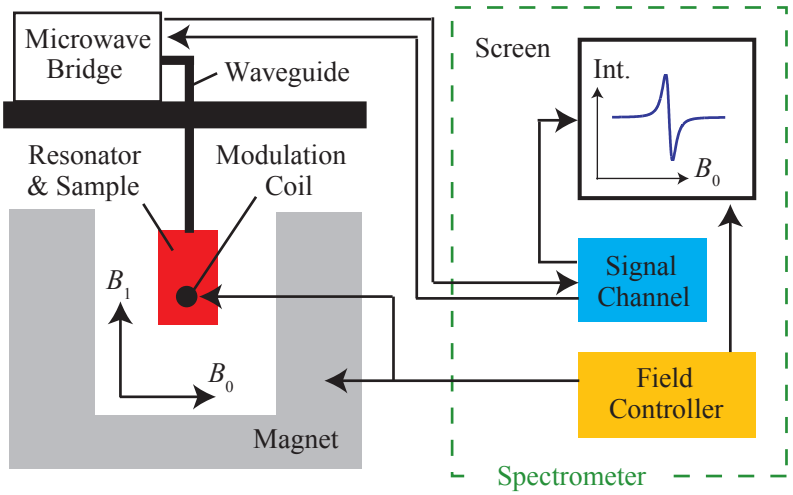

FIGURE 2.1: Schematic showing the major components of a CW ESR experiment.

to the spin Hamiltonian, splitting the energy levels of the electron spin, as discussed in section 1.2.2. In the case that nuclear spins are present, their energy levels are similarly split, as will be introduced in chapter 4. Figure 2.2 shows the energy level structure for a spin, $s = 1/2$. As a result of this splitting, there is a difference in occupation, $n(E_i)$ of each energy level, E_i, proportional to the Boltzmann factor

$$n(E_i) \propto \exp\left(-E_i/k_{\mathrm{B}}T\right), \tag{2.2}$$

where k_{B} is the Boltzmann constant and T the temperature. Consequently, we have net population of the lower energy level, and a resultant net magnetic moment.

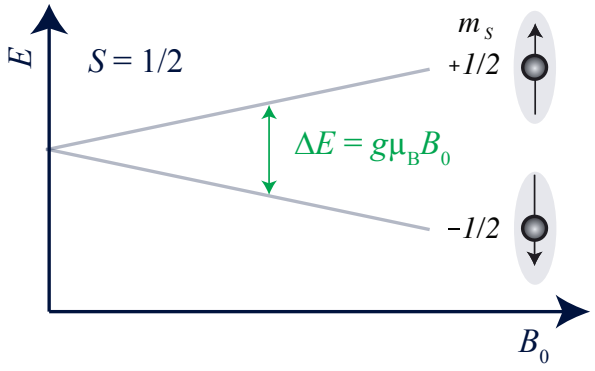

FIGURE 2.2: Energy level structure for a spin, $s = 1/2$, with isotropic g-factor, g, in magnetic field B_0. In green is marked a magnetic dipole transition, resonant when the applied microwave field is of frequency ν such that $h\nu = g\mu_{\mathrm{B}}B_0$.

Now, in order to probe the energy level structure, we apply a second magnetic field, B_1, perpendicular to B_0, in the x-direction, say, oscillating at microwave frequency, ν. This introduces an oscillatory component in the Hamiltonian,

$$H_1(t) = \mu_{\mathrm{B}} B_1(t) g_x s_x. \tag{2.3}$$

When the microwave frequency is such that the single photon energy is resonant with the energy level splitting, for our spin, $s = 1/2$,

$$h\nu = g\mu_{\mathrm{B}} B_0, \tag{2.4}$$

photons are absorbed and we see a transition from the lower to upper energy level, of intensity

$$|a_{ij}|^2 \propto (n(E_i) - n(E_j))| \langle \psi_i | H_1 | \psi_j \rangle |^2, \tag{2.5}$$

where $|\psi_i\rangle$ and $|\psi_j\rangle$ are the initial and final states respectively. From this, we expect transition intensity to be proportional to $|B_1|^2$, that's to say, to the applied microwave power. In the case that m_{S} remains a good quantum number, the resulting magnetic dipole transition rules, corresponding to the nominally 'allowed' transitions, are given by

$$\Delta m_S = \pm 1. \tag{2.6}$$

2.1.2 Microwave Cavity and Q-Factor

In order to apply the required B_1 field, microwaves are generated by a Gunn diode in the microwave bridge, passed along a waveguide and entered into a resonant microwave cavity, essentially a metal 'box', in which a standing wave mode is formed (figure 2.3). The cavity mode has a resonant frequency, ν_0, and quality (Q-) factor, defined by

$$Q = 2\pi \frac{\text{Energy Stored}}{\text{Energy dissipated per cycle}}. \tag{2.7}$$

The sample is placed at a magnetic field antinode in the cavity. The strength of the coupling of the waveguide to the cavity can be controlled by a small screw known as the 'iris', at the entrance to the cavity. When the impedances of the waveguide and cavity are matched, all energy is transferred to the cavity mode and dissipated internally such that no microwaves are reflected back. This is known as the 'critically coupled' regime and it is how we begin a CW experiment. When electron spins in the sample undergo a resonant ESR transition, the cavity Q-factor and impedance are changed. This means that the coupling is no longer critical, and there is some reflected microwave power. It is this reflected power that is measured by a detector diode and gives the CW ESR 'signal'.

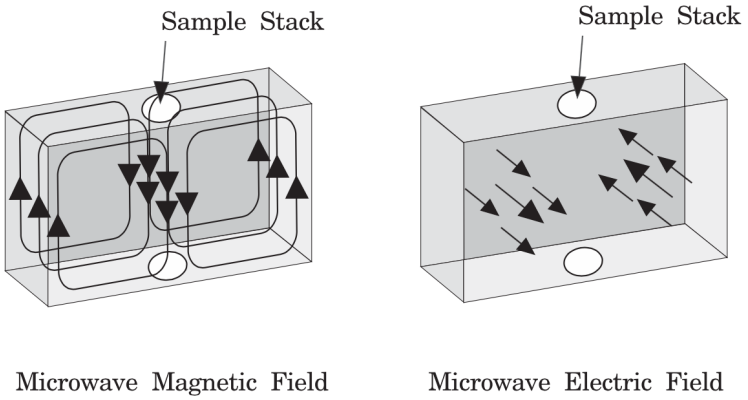

FIGURE 2.3: Magnetic and electric field distributions in the TE_{102} mode of a rectangular resonant cavity. The 'sample stack' shows where the sample is inserted. Taken from [90].

2.1.3 Running an Experiment

In an ESR experiment, we want to explore the whole spectrum. We do this by tuning ν and the iris, such that the cavity is on resonance and critically coupled, and sweep the magnitude of B_0. Now, in many cases, signal to noise can be poor, therefore, in order to improve it, we apply 'field modulation'. What this means is that at every nominal B_0, the applied field is modulated sinusoidally about that value, usually at a frequency $\sim$ 100 kHz. Figure 2.4 illustrates the effect of field modulation. The resulting signal oscillates at the modulation frequency with amplitude proportional to the gradient of

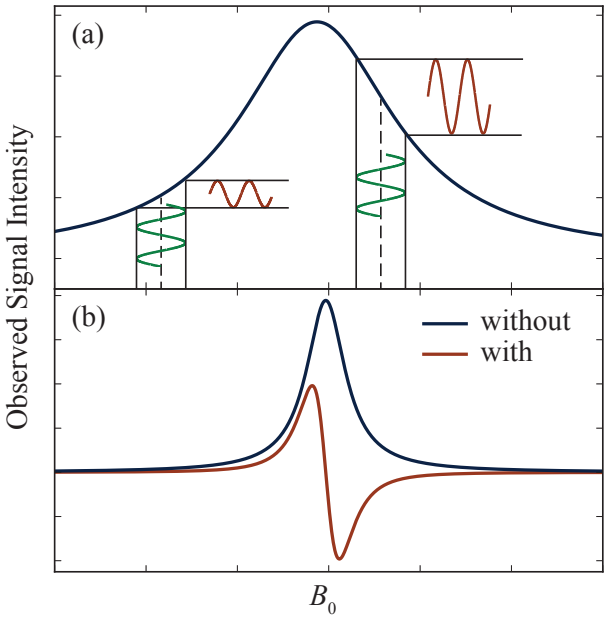

FIGURE 2.4: (a) Gaussian absorption line probed using a modulated B_0 field (green). The amplitude of the observed signal (red) is proportional to the gradient of the line. (b) The signal observed with (red) and without (dark blue) field modulation.

the spectrum at the relevant point. This allows effective signal isolation by eliminating noise components away from the desired frequency, through use of a lock-in amplifier. The resulting spectrum is the derivative of the measured resonance line. The amplitude of the modulation is chosen such that it is small enough that it does not 'smooth' any features of the spectrum but large enough that the signal amplitude is sufficient. In a CW experiment, care must also be taken to apply a power low enough that the populations are only weakly perturbed. This can be verified by checking one is in the regime where signal amplitude is linearly dependent upon B_1 [91]. A power too high 'saturates' the signal.

We often want to look at properties of a sample as a function of temperature. Control of this is achieved through use of a helium flow cryostat. All CW spectra presented in this thesis were measured using a commercial X-band Bruker EMX spectrometer. This makes use of a rectangular TE_{102} mode resonator, with Q-factor values up to 5000.

2.2 Pulsed ESR

2.2.1 General Principles

In a pulsed experiment, we begin again by applying a static magnetic field, B_0, in the laboratory z-direction. This Zeeman splits the electron energy levels and gives net occupation of the lowest energy state such that we have a net magnetic moment, M_0. It is this net moment, the macroscopic property resulting from an ensemble of spins, that we manipulate in a pulsed experiment. In a classical picture, for the model $s = 1/2$ system introduced in section 2.1.1, the magnetisation vector, $\boldsymbol{M}$ precesses about the applied $\boldsymbol{B}_0$ such that

$$\frac{\mathrm{d}\boldsymbol{M}}{\mathrm{d}t} = \boldsymbol{M} \times \frac{-g\mu_{\mathrm{B}}}{\hbar}\boldsymbol{B}_0 \tag{2.8}$$

and the angular frequency of precession, known as the 'Larmor frequency', is given by

$$\omega_L = \frac{g\mu_B B_0}{\hbar}. \tag{2.9}$$

Viewed in a frame rotating about z at ω_L, which we will refer to as 'the rotating frame', $\boldsymbol{M}$ is constant.

We then apply a second magnetic field, B_1, perpendicular to B_0. As discussed in section 2.1.1, if resonant with the transition and allowed by the magnetic dipole selection rules, this will induce a net transition from the lower to upper energy level. In a pulsed experiment, however, the B_1 field applied is of much higher power than its CW counterpart. This is achieved by the addition of a high power amplifier to the set up shown in figure 2.1.

In the lab frame, the linearly polarised B_1 field experienced at the sample's resonant cavity antinode, can be viewed as the superposition of two circularly polarised waves of angular frequency $2\pi\nu$ and opposite senses of rotation. When resonant, $\nu = \omega_{\mathrm{L}}/2\pi$, such that in the rotating frame there is a component at $2\omega_L$, which we ignore and a

stationary component, of magnitude B_1, in the x-y plane, along an an axis dependent upon its phase. For B_1 in the x-direction, $\boldsymbol{M}$ precesses about this, towards the $-y$ axis.

In general we apply B_1 as a pulse of duration T_p. This 'tips' our state towards $-y$ by angle,

$$\xi = \omega_L T_p = g\mu_B B_1 T_p. \tag{2.10}$$

A '$\xi = \pi/2$' pulse tips $\boldsymbol{M}$ such that it is aligned with the $-y$ axis and a $\xi = \pi$ pulse inverts it. We note that ξ can be increased by increasing the microwave power, thereby increasing B_1^2, or by applying a longer pulse. In general, for B_1 along x, the resulting components of $\boldsymbol{M}$ in the rotating frame are

$$\begin{aligned} M_x &= 0 \\ M_y &= -M_0 \sin\xi \\ M_z &= M_0 \cos\xi. \end{aligned} \tag{2.11}$$

For B_1 in the y-direction, these become

$$\begin{aligned} M_x &= M_0 \sin\xi \\ M_y &= 0 \\ M_z &= M_0 \cos\xi. \end{aligned} \tag{2.12}$$

In the lab frame, immediately after removal of B_1, equation 2.11 becomes

$$\begin{aligned} M_x &= M_0 \sin\xi \sin(\omega_{\mathrm{L}} t) \\ M_y &= -M_0 \sin\xi \cos(\omega_{\mathrm{L}} t) \\ M_z &= M_0 \cos\xi. \end{aligned} \tag{2.13}$$

The oscillating components M_x and M_y radiate back into the cavity, to which they are weakly coupled, and are measured simultaneously using a 'quadrature detection' scheme. Two reference signals, 90° out of phase with each other, are mixed with the signal in order to measure the two orthogonal components. These are often referred to as the 'real' and 'imaginary' signals, as the in plane magnetisation can be conveniently represented as an imaginary number, with real and imaginary parts corresponding to $-M_y$ and M_x respectively.

2.2.2 Relaxation

Upon removal of B_1, the signal decays via two mechanisms. On timescale T_1, the z magnetisation is restored and we return to thermal equilibrium:

$$\frac{\mathrm{d}M_z}{\mathrm{d}t} = \frac{-(M_z - M_0)}{T_1} \tag{2.14}$$

This is 'spin-lattice' relaxation as energy is transferred to the lattice, for example via excitation of phonon modes.

The second class of signal decay, as characterised by T_2^* and T_2, results from the loss of phase coherence, and does not involve a transfer of energy. Both environmental variation and inhomogeneity in B_0 mean ω_L is not constant across the population but rather forms a distribution of finite width. After a $\pi/2$ pulse, we see our spins 'fan out' in the rotating frame (figure 2.5(a)(3)). There is a corresponding decay in signal, known as the 'free induction decay' (FID), which occurs on timescale T_2^*. We can also consider the T_2 time. This is the time taken for spins to lose coherence as a result of fluctuations in B_z,

rather than static inhomogeneity. If fluctuations occur on a timescale rapid with the respect to that over which we are observing, their effect will be averaged out. However, if they occur at a lower frequency, they will cause a change in the precessional rate of the affected spin, such that it acquires some additional phase, or rather its phase is scattered. T_2 characterises the rate at which decoherence due to such fluctuations takes place. In order to measure T_2, we form what is known as a 'echo': the subject of the next section.

2.2.3 Hahn Echo

Figure 2.5(a) illustrates the simplest 'Hahn echo' sequence, with pulses applied in the x-direction. A $\pi/2$-pulse is applied to 'tip' $\boldsymbol{M}$ to lie along the $-y$-axis. When this is removed, the spins 'fan out' about the $-y$-axis due to the distribution of ω_{L} values. After time τ, a π-pulse is applied, to invert the component along y. This means that spins of resonant frequency closer to ω_{L} now lie closer to the y-axis and more off resonance spins further from it. The result is that at time τ after the π-pulse they come back together along y and the magnetisation is refocussed. It is this refocussed magnetisation that is known as the 'echo' and it can be thought of as two FIDs back-to-back. We record its integrated intensity, known as the electron spin echo intensity (ESE). Similar to a CW experiment, it is common to sweep the magnitude of B_0, this time measuring the integrated echo intensity for a chosen value of τ, at each point. The resulting spectrum is known as an echo detected field sweep (EFS).

Given that a Hahn echo refocusses time-independent contributions to decoherence in the FID, we can use it to measure T_2. This is done by incrementing τ as shown in 2.5(a). The resulting curve is often a simple exponential decay although different decoherence processes, as will be discussed in chapter 3, can affect its shape as well as the rate of decay. In the field of quantum information processing and in this thesis, T_2 is often referred to as the 'phase memory time', T_{m}.

A related experiment, used to measure T_1, is known as the 'inversion recovery' sequence. In this case, the sequence '$\pi - T - \pi/2 - \pi$' is applied, with the value of T incremented. By inverting $\boldsymbol{M}$ and waiting for time T, before using a Hahn echo sequence to measure the

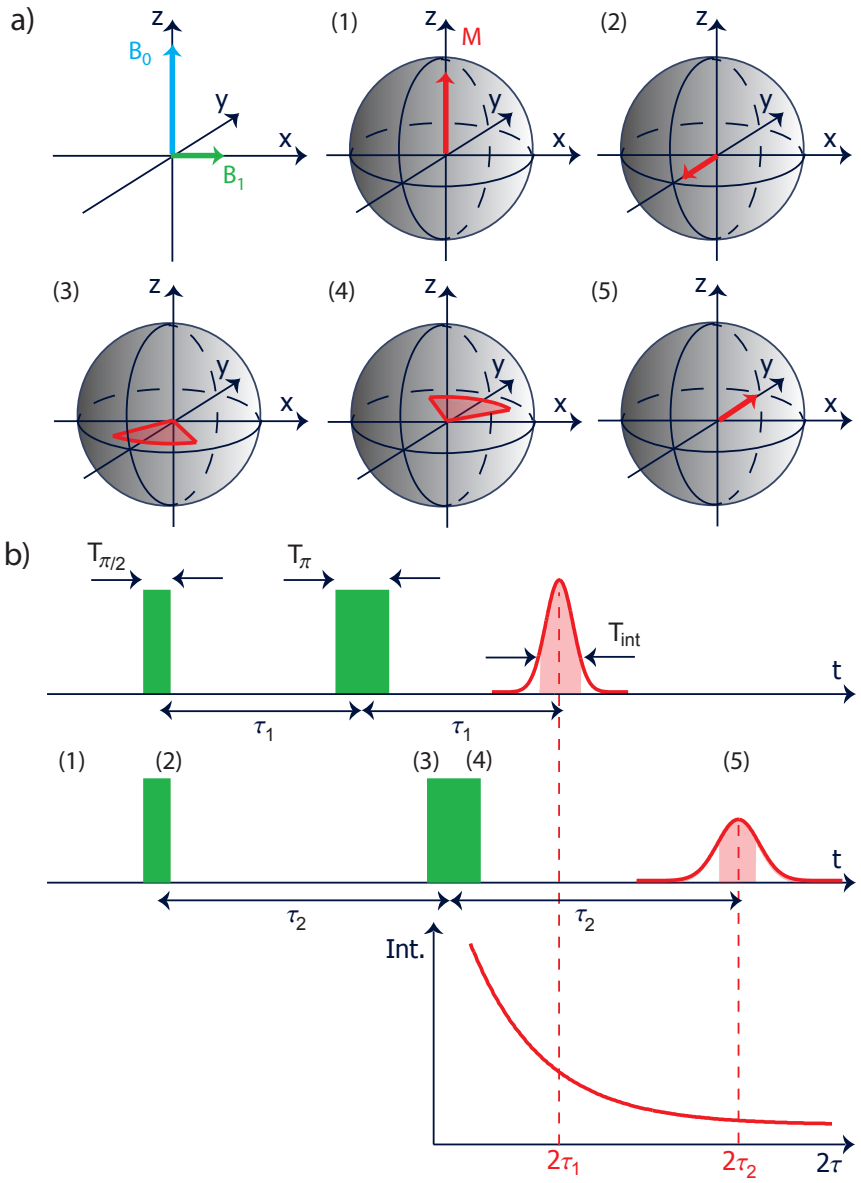

FIGURE 2.5: A T_2 pulse sequence. (a) shows field orientations and evolution of our spins on the Bloch sphere. (b) shows the pulses applied and spectrum obtained.

remaining component of $\boldsymbol{M}$ in the z-direction, we track the recovery of the equilibrium value. The resulting curve usually takes the form $a(1 - b\exp(-T/T_1))$, where a and b are constants, although, as was the case with the T_2 curve, certain relaxation processes can distort this.

2.2.4 Phase Cycling

Often, when we integrate the echo, we include not only the signal we want to observe, but also unwanted contributions such as, for example, some component of ringing which

has not yet fully decayed or coherence resulting from a pathway alternative to that which we intended. In order to minimise such effects we employ 'phase cycling'. This involves application of pulses in different channels and subsequent addition or subtraction of the resulting integrated intensity.

In this thesis, we will employ two phase cycle routines, the first is a two-step phase cycle, as applied to a Hahn echo sequence, summarised by table 2.1. The phase of the first pulse is inverted, which inverts the phase of the resulting echo. The integrated intensity from step 2 is then subtracted from that from step 1 to give the final value.

TABLE 2.1: Phase routine for a two-step phase cycle.

Pulse	$\pi/2$	π	echo
Step 1	$+x$	$+x$	$+y$
Step 2	$-x$	$+x$	$-y$

Table 2.2 shows an example four-step scheme, used in a nutation experiment, which will be introduced in chapter 6. In this case the final intensity is calculated from (step 1 + step 2) − (step 3 + step 4).

TABLE 2.2: Phase routine for a four-step phase cycle.

Pulse	ξ	$\pi/2$	π	echo
Step 1	$+x$	$+x$	$+x$	$+y$
Step 2	$-x$	$+x$	$+x$	$+y$
Step 3	$+x$	$-x$	$+x$	$-y$
Step 4	$-x$	$-x$	$+x$	$-y$

2.2.5 Experimental Setup and Cavity

The experimental setup used for a pulsed ESR experiment is very similar to that used for a CW experiment. All pulsed experiments in this thesis were performed at X-band such that an electromagnet was sufficient to provide the required B_0. The microwave system is the same as in the CW case, with the addition of a high power amplifier and quadrature detection channel, as was discussed in section 2.2.1. In contrast to the CW case, however, we 'over' rather than critically couple the cavity. What this means is that the total Q-factor of the system is lower (typically ~ 250) and more energy is reflected (equation 2.15). Immediately following a pulse, the power in the cavity is so high that it

would damage the detector diode if a measurement were made. This results in a certain amount of 'dead time'. A reduced Q-factor means the applied power is dissipated more rapidly such that measurement dead time is minimised. An alternative way to express the Q-factor is

$$Q = \frac{\nu}{\Delta\nu}. \tag{2.15}$$

Here ν is the central frequency of the resonant mode and $\Delta\nu$ the mode bandwidth. Figure 2.6 illustrates this. A lower Q-factor leads to a greater available bandwidth, which we will see in chapters 5 and 6 is very useful for multifrequency experiments.

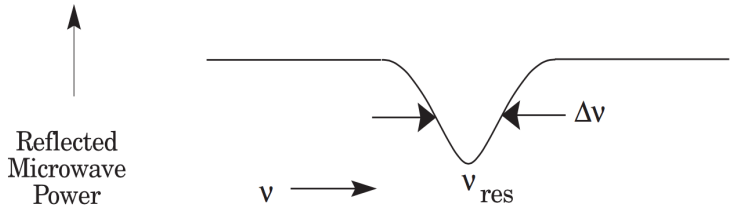

FIGURE 2.6: Reflected microwave power from a resonant cavity with central resonant frequency, ν_{res}. Taken from [90].

All pulsed experiments in this thesis were performed using a commercial Bruker ELEX680 spectrometer, with either a rectangular TE_{102} (figure 2.3) or split ring resonator. Temperatures down to $T = 2.5$ K were achieved by use of a flow cryostat. Field modulation is not used in pulsed ESR, however, signal to noise is improved by repeating each application of a pulse sequence multiple times. The time between the start of each 'shot' is known as the 'shot repetition time' and care must be taken to choose a time long enough that the system returns to thermal equilibrium before the next 'shot' is begun. This an issue encountered in chapter 4.

2.2.6 Pulse Lengths

When we apply a B_1 pulse of rectangular profile in time, oscillating at frequency ν, it introduces a finite bandwidth of frequencies in the cavity. This is illustrated by figure 2.7, which shows the Fourier transform for a pulse applied at frequency ν_0 for time T_{p}. We

see the width of the resulting frequency spectrum is proportional to $1/T_\mathrm{p}$ such that a longer pulse gives a narrower distribution of frequencies. If we want only to excite transitions within a particular range of frequencies, we therefore have to choose very carefully the pulse length. This will be particularly important when choosing molecules of a given orientation in chapter 5.

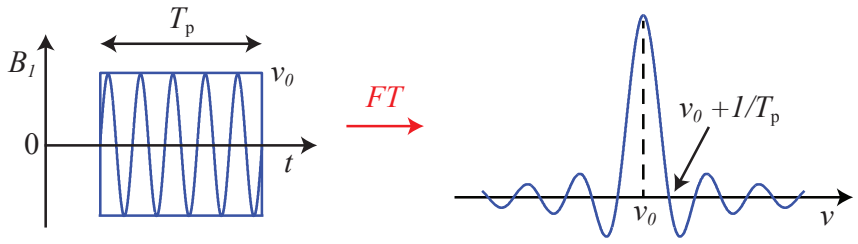

FIGURE 2.7: Ideal profile of a pulse applied with frequency ν_0 for duration T_p and its Fourier transform.

2.2.7 ESEEM

Electron spin echo envelope modulation is an effect that occurs as a result of the electron spin coupling to nearby nuclei. In order to account for this we include an additional contribution to equation 1.6,

$$H_\mathrm{nuc} = \mu_\mathrm{N} g_\mathrm{N} \boldsymbol{B}_0 \cdot \boldsymbol{I} + \boldsymbol{S} \cdot \boldsymbol{A} \cdot \boldsymbol{I}, \tag{2.16}$$

where μ_N is the nuclear magneton, g_N the isotropic nuclear g-factor, I the nuclear spin and A the hyperfine coupling tensor, with components directly analogous to those discussed regarding the exchange coupling tensor, $\boldsymbol{J}_{ij}$, in section 1.2.2. The result is that the precessional frequency of the electron is dependent upon the nuclear state.

When we apply a pulse of finite bandwidth, in some cases, it will contain not only the resonant frequency required to flip an electron but also that required to flip both an electron and a nucleus, and in some cases the nucleus will be flipped. The effect of this is that electrons coupled to nuclei which have been flipped, will precess at a slightly different rate to those which are not. In a T_2 experiment, as we increment τ,

this results in the oscillation of our decaying signal, as the component now slightly off resonance, comes in and out of phase with those electrons whose surrounding nuclei remained unchanged.

The effect can be used as a tool to gain quantitative insight into nuclear couplings [92]. In this case, a complete description of the effect is required, which predicts oscillating components at multiple frequencies. However, this is beyond the scope of this thesis, in which the effect will appear only as an annoyance, which we will aim to remove. In cases where the energy required for a nuclear transition is large (for example for hydrogen nuclei), this can be done by increasing the pulse lengths, to reduce the bandwidth such that the transition involving a nuclear flip now falls outside of it. In the case of deuterium this was found to be ineffective due to its low magnetic moment. In previous work on related compounds, the ESEEM was found to include at most two frequency components, governed by the strength of nuclear Zeeman interaction [93]. We therefore accounted for deuterium ESEEM by including such oscillatory terms in the T_2 fit (chapter 3).

2.2.8 Frequency Bands

In this thesis measurements are carried out in the most common frequency region, 'X-band' only, however, one can carry out both CW and pulsed ESR experiments over a much wider range of frequencies. The bands in typical use are listed in table 2.3. As one moves to higher frequency, resolution is enhanced due to a given separation in g-factor corresponding to a greater field separation. In addition, the corresponding increase in B_0 enhances sensitivity by increasing energy level separation and therefore the excess population in the lower energy state. However, the increase in applied field strength for W and D band experiments requires a superconducting magnet, cooled with helium, rather than the resistive magnet that is sufficient at X-band.

2.2.9 Sample Preparation

The majority of samples measured in this thesis are molecules dissolved in organic solvent. The solution is made up in a glass vial and transferred to a cylindrical quartz ESR

TABLE 2.3: Bands of ESR experiment with typical operating frequencies and corresponding B_0 values for $g = 2.0$.

Band	Frequency (GHz)	B_0 (T)
S	3	0.11
X	10	0.36
Q	35	1.25
W	95	3.40
D	130	4.65

tube of diameter 3-4 mm. All stages of this process are carried out under argon to minimise the addition of any moisture from the air, which can affect sample stability. Once in the glass tube, the sample is usually subjected to three or four 'freeze-pump-thaw' cycles. The purpose of these is to remove dissolved oxygen, which is paramagnetic and can reduce relaxation times [94]. The sample is connected to a vacuum line and, in one cycle, is frozen, pumped to remove air in the tube, sealed off again and thawed to release dissolved gasses. When the process is complete, the top of the tube is flame sealed, such that it is air tight.

The concentration in most samples is chosen to avoid 'instantaneous diffusion', which occurs when it is too high. In a frozen solution of spins with the same nominal resonant frequency, say A spins, they interact with each other via a magnetic dipole interaction. When a pulse is applied and A spins are tipped, this causes a change in the resonant frequency of other A spins, due to the dipolar interaction between them. If the concentration is too high (the strength of the magnetic dipole interaction scales as the inverse cube of their separation), this change in resonant frequency interferes with the refocussing process. In a T_{m} experiment, this provides an additional dephasing component and causes an apparent reduction in T_{m} [95].

2.2.10 Density Matrices

While a classical vector picture of ESR is perhaps the most intuitive in the case that we have one spin and two energy levels, in some situations, for example when the electron is coupled to a nuclear spin, we require a more sophisticated formalism. This is provided

by the density matrix description, which, unlike either the classical or state vector descriptions, allows us to describe both pure and mixed states [96].

Considering firstly the pure state

$$|\psi(t)\rangle = \sum_n c_n(t)|u_n\rangle, \tag{2.17}$$

where u_n is an orthonormal set of basis states and $\sum_n |c_n(t)|^2 = 1$, we can calculate

$$\langle u_p|\psi(t)\rangle\langle\psi(t)|u_n\rangle = c_n^*(t)c_p(t), \tag{2.18}$$

where $|c_n(t)|^2$ represents the probability of occupation of basis state $|u_n\rangle$ and $c_n^*(t)c_p(t)$ for $n \neq p$ represents the coherence between states $|u_n\rangle$ and $|u_p\rangle$. These form the elements of our 'density matrix'. For example, if we have an electron and a nuclear spin described by the basis

$$|\psi(t)\rangle = c_{00}(t)|00\rangle + c_{10}(t)|10\rangle + c_{01}(t)|01\rangle + c_{11}(t)|11\rangle, \tag{2.19}$$

where 0 corresponds to spin down, 1 to spin up and the first and second numbers to the electron and nucleus respectively, the resulting density matrix is given by

$$\rho(t) = \begin{pmatrix} |c_{00}(t)|^2 & c_{00}^*(t)c_{01}(t) & c_{00}^*(t)c_{10}(t) & c_{00}^*(t)c_{11}(t) \\ c_{10}^*(t)c_{00}(t) & |c_{10}(t)|^2 & c_{10}^*(t)c_{01}(t) & c_{10}^*(t)c_{11}(t) \\ c_{01}^*(t)c_{00}(t) & c_{01}^*(t)c_{10}(t) & |c_{01}(t)|^2 & c_{01}^*(t)c_{11}(t) \\ c_{11}^*(t)c_{00}(t) & c_{11}^*(t)c_{10}(t) & c_{11}^*(t)c_{01}(t) & |c_{11}(t)|^2 \end{pmatrix}. \tag{2.20}$$

Its time evolution is described by the *Liouville-von Neumann* equation,

$$\frac{\mathrm{d}\rho}{\mathrm{d}t} = -i[H(t), \rho(t)], \tag{2.21}$$

where $H(t)$ is the time dependent Hamiltonian.

In the case that we have a mixture of pure states, i represented by individual density matrices, ρ_i, we may define the density matrix as the normalised sum over ρ_i:

$$\rho(t) = \sum_i p_i \rho_i(t), \tag{2.22}$$

where p_i is the probability of occupation of pure state i. For a pure state the trace, $\mathrm{Tr}\rho^2(t) = 1$ and for a mixed state $\mathrm{Tr}\rho^2(t) < 1$ [92]. In both cases the expectation value of an observable A, is given by

$$\langle A \rangle = \mathrm{Tr}\{A\rho\}. \tag{2.23}$$

Chapter 3

Halogenation of Cr_7Ni Rings

3.1 Introduction

An essential property of a qubit is a coherence time significantly longer than that required to perform single qubit manipulations and two qubit gates (section 1.1.1). In 2007, it was shown that the ground state spins of certain Cr_7M based rings did in fact, at low enough temperature, satisfy this requirement, showing coherence times up to 3.8 μs at 1.8 K, which is several orders of magnitude longer than the approximate time of 10 ns required to manipulate a single qubit using pulsed ESR [88]. In addition to verifying the feasibility of MNMs as qubits, the study compared T_1 and T_2 times for structurally similar Cr_7Ni ($S = 1/2$) and Cr_7Mn ($S = 1$) rings, across a range of temperatures, in order to identify sources of relaxation and decoherence. It was found that T_1 was dependent upon the zero-field splitting parameters, which, for $S > 1/2$, can be modulated as a result of coupling to excited modes of mechanical deformation. In contrast, T_2 appeared to be dominated by coupling to the surrounding network of ^{1}H nuclear magnetic moments. It was by replacing these instead with ^{2}H (D) nuclei, which have an approximately six times smaller gyromagnetic ratio (table 3.1), that the coherence time of 3.8 μs at 1.8 K for a Cr_7Ni based ring, was reached, more than six times longer than that for its hydrogenated analogue.

TABLE 3.1: Nuclear spin, relative magnetic moment and relative gyromagnetic ratio for relevant nuclei.

Element	Nuclear Spin	Magnetic Moment Relative to ^{1}H	Gyromagnetic Ratio, γ Relative to ^{1}H
^{1}H	1/2	1	1
^{2}H (D)	1	0.307	0.154
^{19}F	1/2	0.941	0.941
^{35}Cl	3/2	0.294	0.098
^{37}Cl	3/2	0.245	0.082

Motivated by the enhancement in coherence time that this chemical modification delivered, a further, more substantial study was carried out, attempting to identify more precisely the mechanisms of decoherence in a Cr_7Ni based MNM [89]. By systematically modifying the carboxylate bridging ligand and the central templating cation (red and blue respectively, in figure 3.1 (a)), and recording T_2 over a range of temperatures, the study provided significant new insight. It was found that decoherence was affected by both the magnetic and inertial properties of surrounding nuclei, including those in the carboxylate bringing ligand, those in the central templating cation and those in the solvent. Methyl groups were proven to be particularly effective at driving decoherence due to their potential to show significant librational motion and quantum tunnelling rotations (section 3.2), even at liquid helium temperatures [97, 98]. An optimal coherence time of 15.3 μs at 1.5 K was achieved for a Cr_7Ni ring with a perdeuterated pivalate carboxylate ($(CH_3)_3CCO_2H$) bridging ligand, templated around a single Cs^+ ion, in deuterated solvent.

The work presented in this chapter follows on from this, aiming to determine the effects on phase memory time of substituting H atoms not only for D but also for halogen atoms. This is motivated by the chemically similar, but physically distinct, properties of these atoms (table 3.1). Fluorine has magnetic properties very similar to H but its mass is 19 times greater, allowing us to examine motional effects. In addition, the chlorine atom has a much smaller magnetic moment than hydrogen and is relatively bulky so could, for example, replace an entire methyl group, allowing construction of bulky ligands containing fewer magnetic nuclei [99].

The chapter begins with an overview of possible decoherence mechanisms, moving on

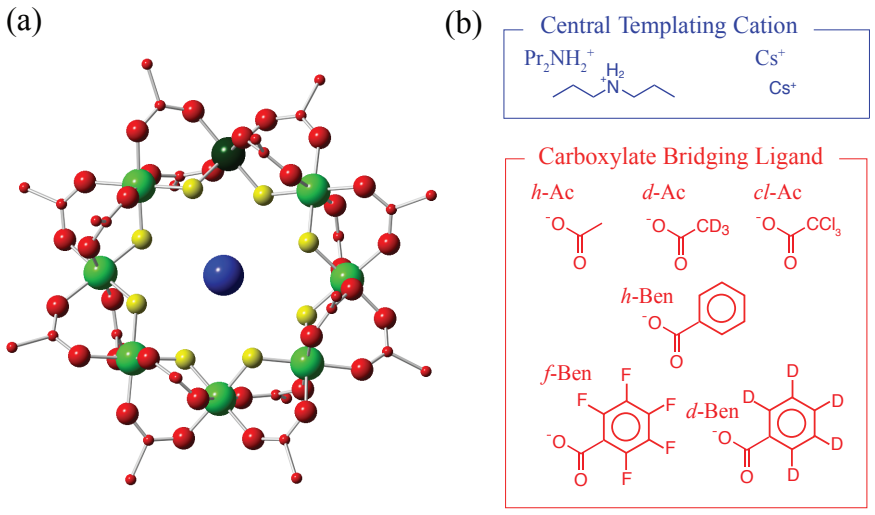

FIGURE 3.1: Structures of the Cr_7Ni molecules. (a) Crystal structure of $Cs[Cr_7NiF_8Ac_{16}]$. The colored balls represent either different atom types: Cr (light green), Ni (dark green), F (yellow), or different interchangeable substituents: central templating cation (blue), carboxylate bridging ligand (red). Hydrogen atoms have been omitted for clarity. (b) Appropriately color coded chemical structures of some possible variants with abbreviated names.

to present the compounds synthesised. The magnetic susceptibility as a function of temperature, as measured by a superconducting quantum interference device (SQUID), is presented for select compounds. This is followed by pulsed ESR data, including T_2 as a function of temperature, with accompanying analysis and interpretation. All samples were synthesised by Dr Grigore Timco at the University of Manchester. Sample preparation was carried out by myself. SQUID measurements were carried out by myself with help from Dr Junjie Liu. ESR data were collected by myself and Dr Amy Webber. All data analysis is my own. The chapter is based on work already published, where full synthetic details and crystallographic information for the compounds can be found [100].

3.2 Decoherence Mechanisms

Phase decoherence that is not refocussed in a spin echo experiment is caused by magnetic field fluctuations at the site of the excited electron spin. In the rigid limit, we expect these to be dominated by nuclear spin flip-flop processes. Although conserving net magnetisation, such flip-flops cause local magnetic field fluctuations at the site of the electron spin, transmitted via a magnetic dipole interaction. The flip-flop rate of any

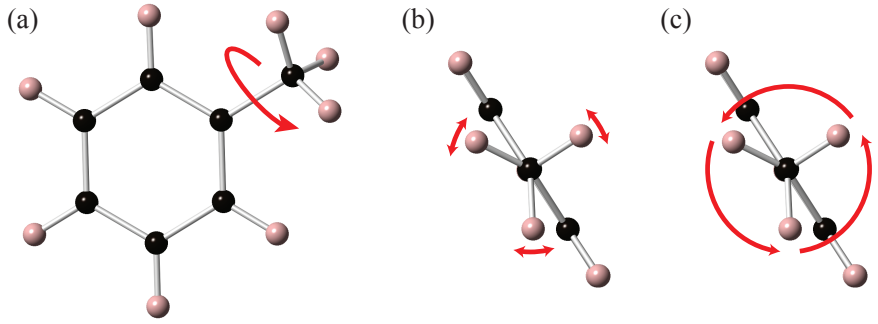

FIGURE 3.2: (a) Toluene (C_7H_8) molecule, with the red arrow marking the axis about which methyl rotation may occur. (b) View down the rotation axis, with the red arrows illustrating librational motion (back and forth rotations of very small amplitude) of the methyl group. (c) View down the rotation axis, with the red arrows marking a quantum tunnelling rotation of the methyl group. The coloured balls represent C (black) or H (pink).

individual nucleus is low (typically $\sim$ 10kHz), but the efficiency of the decoherence process can be enhanced by a large bath of available spins, for example, in the solvent [99]. We refer to this as *nuclear spin diffusion*.

Moving away from the rigid limit, we must also consider motional effects, both as a direct cause of magnetic field fluctuations and something which affects the rate of nuclear spin flip-flops. At the temperatures investigated, we expect bond vibration to be frozen out. However, rotations and librations are still possible, particularly of light atoms, as illustrated by figure 3.2 for a methyl (CH_3) group. At such temperatures, the quantisation of motion becomes relevant, making it difficult to predict the dephasing effect that any given group will have [101]. For example, in the case that we have approximately harmonic librational modes, we find that, in the limit of small displacement, the eigenfrequency of oscillation, $\nu \sim \sqrt{V/I}$, and the mean square displacement, $\overline{\Delta\theta^2} \sim 1/\sqrt{VI}$, where I is the moment of inertia and V the height of the potential [102]. As mass is increased, quantum tunnelling rotations are suppressed, however, I increases, giving rise to more accessible librational modes [89]. Decoherence resulting from motion will be termed *spectral diffusion*.

The processes discussed affect not only the decoherence time, T_2, but also the shape of the echo decay curve. We fit our curves to the 'stretched exponential' form:

$$Y(2\tau) = Y(0)\exp\left(-(2\tau/T_{\mathrm{m}})^x\right) + c, \tag{3.1}$$

where τ is the time delay between pulses, $Y(0)$ is the extrapolated echo intensity at $\tau = 0$ and c accounts for a small linear baseline offset of instrumental origin. T_m and x are phenomenological parameters known as the phase memory time and stretch parameter, respectively. Their values depend on both the dominant mechanism of decoherence and its rate. We find that nuclear spin diffusion processes increase the stretch parameter, giving rise theoretically to a value of $2 \leq x \leq 3$, depending on the exact model [99, 103, 104]. In contrast, spectral diffusion processes are found to lower the stretch parameter, which can reach 0.5 if the motional correlation time is on the order of the pulse delay [99].

3.3 Synthesis of Compounds

All compounds investigated were based on the heterometallic Cr_7Ni rings, of ground state spin $S = 1/2$, discussed in section 1.2.3. The effects of several classes of modification were explored: substituting the pivalate in the bridging ligand with a group in which we replace H with D, F or Cl; templating around different cations; and solvent deuteration. Figure 3.1 shows the structures that we were motivated to study by the possibility of modifying the phase memory time and stretch parameter of the Cr_7Ni spin.

Cr_7Ni rings assemble readily around a wide range of cations [89]. In the present investigation, we chose to study rings templated around either a caesium cation (Cs^+), which was earlier found to support long phase coherence times, or around a large di-propyl ammonium ($Pr_2NH_2^+$) cation, as an alternative synthetic target. These cations are shown in blue in figure 3.1(b). We identified acetates (Ac), and benzoates (Ben), shown in red in figure 3.1(b), as carboxylate ligands in which hydrogens may readily be exchanged for halogens.

It was found that not all combinations of cations and ligands in figure 3.1 formed stable compounds. It was possible to synthesise fully Cl-substituted Ac rings around the $Pr_2NH_2^+$ template, but this was not stable in solution, so we were unable to study pulsed ESR in this structure. The analogous Cs^+ structure is expected to be even less stable and no attempt was made to synthesise it. Hydrogenated-, deuterated-, and fluorinated-Ben (*h*-Ben, *d*-Ben, *f*-Ben respectively) ligand structures formed successfully around the

$Pr_2NH_2^+$ cation. While it was possible to synthesise the chlorinated-Ben (*cl*-Ben), it was not soluble in the solvents used for pulsed ESR measurements. It was possible to synthesise *h*-Ben and *d*-Ben rings around Cs^+, but the synthesis of *f*-Ben generated many by-products, and a sample of the pure fully-substituted ring was not obtained.

3.4 SQUID Measurements

Given that fluorine is much more electronegative than hydrogen (3.98 on the Pauling scale, compared with 2.20 for hydrogen), we considered the possibility that fluorine substitution might distort the structure sufficiently to modify the exchange couplings within the Cr_7Ni ring. In order to check this, we measured the d.c. magnetic susceptibility of the sample, χ_m, defined by

$$M = \chi_m H \tag{3.2}$$

where H is the applied static magnetic field intensity and M the resulting equilibrium magnetisation of the sample, as a function of temperature, T. At a given T and H, M is determined by the equilibrium occupation of the MNM's spin levels. Therefore, as T decreases, $\chi_m(T)$ reflects the rate at which spins move from upper to lower spin multiplets. In the strong exchange limit, for a given set of magnetic ring constituents, this is largely controlled by $J_{i,j}$, the strength of the isotropic exchange couplings between them and features in $\chi_m(T)$ can be identified with magnetic excitations in the ring. By fitting to a Hamiltonian accounting for all dominant spin multiplets, this permits extraction of the magnitudes of $J_{i,j}$ [83, 105].

$\chi_m(T)$ data were obtained using a standard Quantum Design MPMS 7 T SQUID. This utilises a superconducting loop with two parallel Josephson junctions, measuring the phase difference between the currents passing through each one [106]. With the measured phase difference dependent upon the magnetic flux in the ring, we are able to make very accurate readings of the change in magnetic flux resulting from the magnetisation of the sample. Measurements were taken on powder samples of the *h*-Ben, *d*-Ben and *f*-Ben

compounds templated around the $Pr_2NH_2^+$ cation, across the temperature range 1.8 to 300 K, with an applied magnetic field of strength 0.1 T.

Figure 3.3 shows the $\chi_m(T)$ data obtained, which are in agreement with previously reported values for Cr_7Ni [107]. We see that the magnetic susceptibilities of all three compounds are almost identical, with turning points, indicative of exchange coupling strength, occurring at the same temperatures. From this, we conclude that there is little variation in the strength of the isotropic exchange interactions within the metal ring for the compounds studied here, and that the F atoms in the ligand do not affect this.

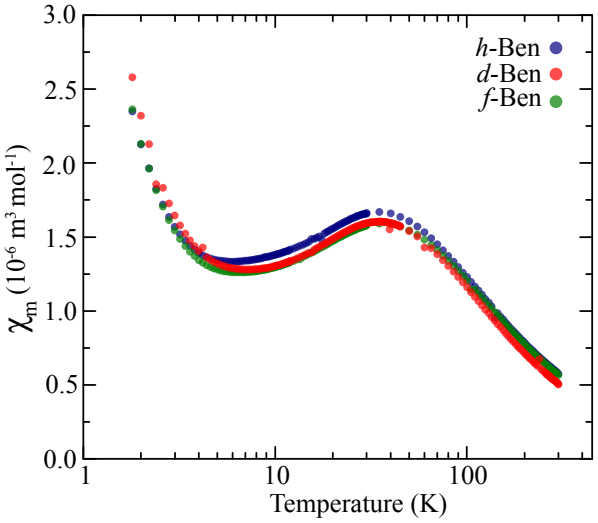

FIGURE 3.3: Magnetic susceptibility, χ_m as a function of temperature, T for compounds templated around a $Pr_2NH_2^+$ cation, measured with an applied magnetic field of 0.1 T.

3.5 ESR Measurements

Phase memory times of all fully substituted, stable compounds were measured using X-band ($\sim$ 9.5 GHz) pulsed ESR spectroscopy over the temperature range 3 to 5 K, applying the standard Hahn echo sequence, '$\pi/2 - \tau - \pi - \tau -$ echo', with a two-step phase cycle, as discussed in section 2.2.3.

The compounds were dissolved in dry hydrogenated or deuterated toluene (*h*-tol, *d*-tol respectively), the structure of which is shown in figure 3.2, and diluted such that intermolecular dipolar interactions could be neglected ($\lesssim 10^{-4}$M). This was verified by

measuring T_2 as a function of pulse length, as discussed in section 2.2.9, in order to check that there was no instantaneous diffusion. Dissolved oxygen was removed via the 'freeze-pump-thaw' method described in section 2.2.9 and all samples were subsequently flame sealed in quartz tubes of diameter 3-4 mm. Samples were flash-frozen before being inserted into the spectrometer in order to ensure that the solvent formed a glass, and therefore that our MNMs were evenly distributed.

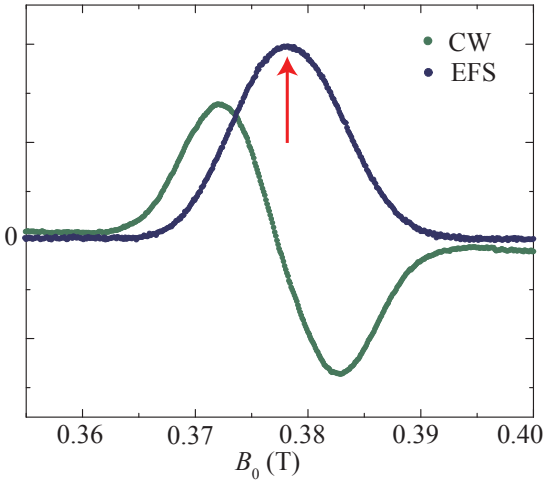

FIGURE 3.4: CW and EFS spectra for the Cr_7Ni ring with an *h*-Ben ligand, templated around an ammonium cation, in *d*-tol. (Green) CW signal intensity in arbitrary units against applied magnetic field, B_0 (T), for an applied microwave frequency, $\nu = 9.449$ GHz. (Blue) EFS integrated echo intensity in arbitrary units against B_0 (T), for an applied frequency of $\nu = 9.454$ GHz and π-pulse length of 128 ns. The red arrow marks the field position selected from the EFS for use in subsequent T_2 measurements.

For each sample, both CW and echo detected field sweep (EFS) spectra were recorded at $T = 5$ K. These were, in the first instance, used to ensure that the sample had not decomposed. Cr_7Ni rings show a characteristic single resonance at $g \approx 1.8$ (figure 3.4), which was checked for in both spectra. The peak of the EFS was also used in order to choose the field position for subsequent measurements. In all cases, this was chosen to be at the peak of the resonance, as marked in the figure.

Example T_2 spectra and fits are shown in figure 3.5. In figure 3.5(a), we note the strong ESEEM at the deuterium nuclear Larmor frequency. The magnetic moments of hydrogen and fluorine nuclei are sufficiently large that the bandwidth of a 128ns π-pulse is not wide enough to excite their ESEEM. However, in the case of deuterium, which has a lower magnetic moment ($\gamma_H/\gamma_D \approx 6.5$), this is not the case. Using lengthened pulses, thereby

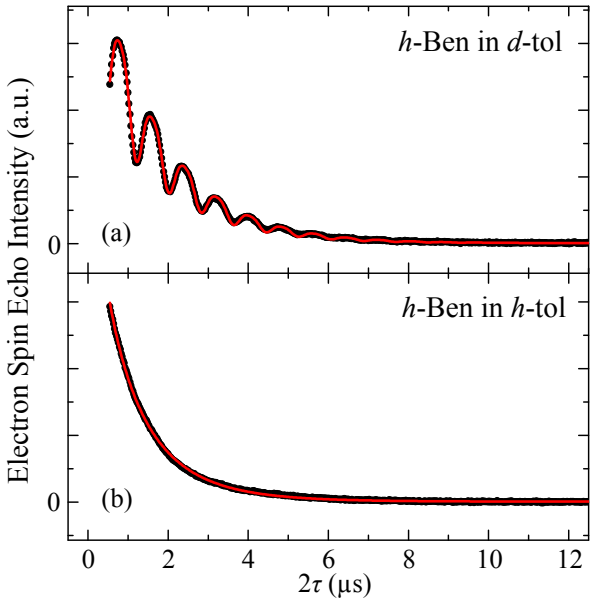

FIGURE 3.5: Echo decay curves (black points) with the relevant fits (red line), for the *h*-Ben compound templated around a $Pr_2NH_2^+$ cation, at temperature $T = 4$ K.

reducing the excitation bandwidth, we were able to reduce the modulation depth of the deuterium ESEEM, however, we were unable to remove it completely, as is illustrated by the figure. For each sample, spectra were recorded using π-pulse lengths of 32 ns, 128 ns, and, in cases where the ESEEM was particularly strong, 400 ns. However, all data presented in this chapter have been recorded with a π-pulse length of at least 128 ns.

Spectra not exhibiting ESEEM fitted well to the stretched exponential function (equation 3.1) discussed in section 3.2. In the cases in which ESEEM was present, the first term of equation 3.1 was multiplied by a modulation function accounting for both its fundamental frequency (ω) and first harmonic (2ω):

$$Y(2\tau) = Y(0)\exp(-(2\tau/T_m)^x)(1 + k_1\sin(2\omega\tau + \phi_1) + k_2\sin(4\omega\tau + \phi_2)) + c, \qquad (3.3)$$

with $Y(0)$, T_m, x, k_1, k_2, ϕ_1, ϕ_2, ω and c being freely varying fitting parameters. The additional parameters k_1 and k_2 characterise the modulation depth of the two ESEEM components and ϕ_1 and ϕ_2 give their respective phases. To reduce the number of variable

parameters the modulations were not permitted to decay independently of the overall decay of the echo signal, although in reality the decay of modulations may be faster [92]. Phase memory times were determined by least squares fitting of the echo decay with the relevant expression using a MATLAB solver based on the Trust-Region algorithm.

3.6 Results and Interpretation

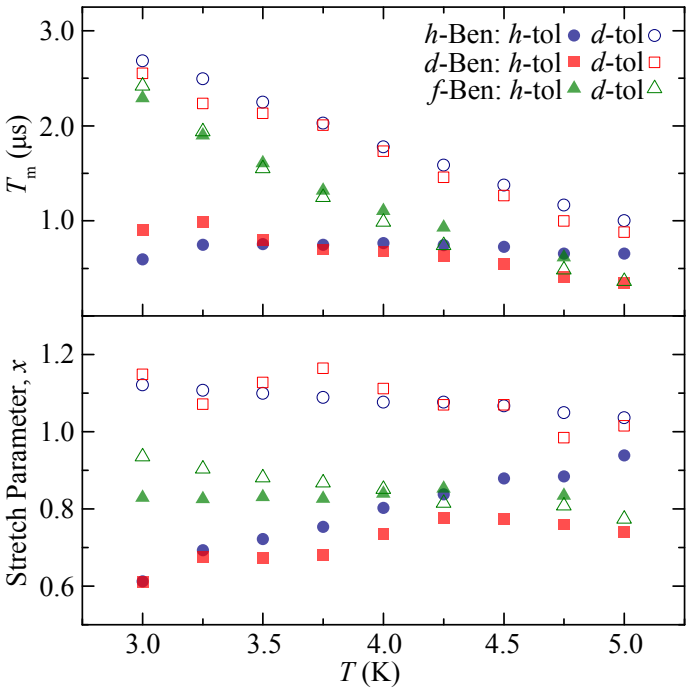

FIGURE 3.6: Phase memory time, T_m and stretch parameter, x for compounds templated around a $Pr_2NH_2^+$ cation. Error bars from the fit are omitted as these were on the order of the marker size.

Figure 3.6 shows the T_m and x values for compounds templated around the ammonium cation. In *h*-tol, there is a marked increase in T_m at low temperatures for the fluorinated compound. As fluorine and hydrogen are magnetically similar, and we confirmed through measurement of $\chi_m(T)$ that the intra-molecular exchange interactions are similar, we conclude that this difference arises from structural effects. As with other 2,6-substituted benzoic acids, in the pentafluorobenzoate the aromatic ring of the benzoate ligands is rotated out of the plane of the carboxyl group [108]. This significantly alters the local environment of the central templating cation, hindering both penetration of solvent molecules and rotation and libration of the central methyl groups. The

temperature dependence of the phase memory time indicates that such rotations and librations are frozen out at lower temperatures in the fluorinated compound but continue to dominate phase decoherence through spectral diffusion in the protonated and deuterated compounds. Despite variation in the efficiency of dephasing by spectral diffusion between compounds, in all cases the stretch parameter remains low ($x < 1.2$) across the given temperature range. This indicates that spectral diffusion rather than nuclear spin-diffusion is the limiting phase decoherence pathway in the regime investigated.

We also note that the phase memory times for the *h*-Ben and *d*-Ben ligands are very similar and in *h*-tol remain roughly constant with temperature. This is in contrast to previously investigated ligands such as pivalate, for which deuteration has a significant effect [89]. The insensitivity to ligand deuteration (which is not expected to affect structure) shows that in these compounds the protons of the ligand are not involved in the limiting phase decoherence pathway. The likely reason for this is that the relatively unhindered rotation of the methyl groups of the ammonium cation is much more effective at driving phase decoherence, aided by the possibility of quantum tunnelling transitions.

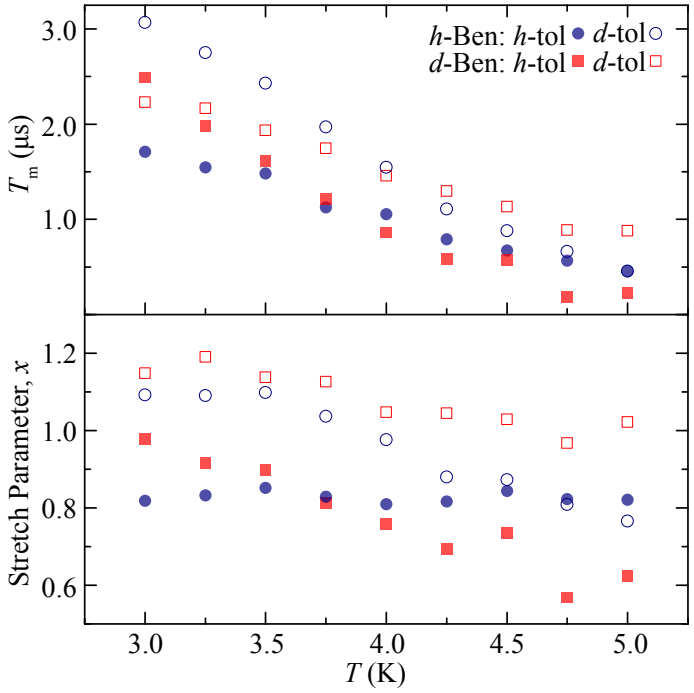

FIGURE 3.7: Phase memory time, T_m and stretch parameter, x for compounds templated around a Cs^+ cation. Error bars from the fit are omitted as these were on the order of the marker size.

The T_m and x values for h-Ben and d-Ben compounds templated around the Cs^+ cation are presented in figure 3.7. Although caesium substitution of the fluorinated compound was not possible we note that the phase memory time now increases with decreasing temperature for protonated and deuterated benzoate ligands, exceeding those in the respective ammonium templated compounds in h-tol. This supports the hypothesis that, when coupled to a large proton spin-bath, the protons of the ammonium cation limit phase coherence. The low stretch parameter ($x < 1.2$) again indicates spectral diffusion to be the dominant decoherence mechanism in these caesium templated compounds.

In all of the cases studied except the fluorinated compound it is found that solvent deuteration increases phase memory times. This is not unexpected, given that the solvent nuclei provide a large spin network that can be very effective in dephasing the electron spin directly, as well as acting as a spin-bath for nuclear spin flip-flops with other nuclei in the system, including those of the carboxylate ligand and central templating cation. The lack of increase in T_m upon solvent deuteration in the case of the f-Ben ligand is likely related to hindered access of the solvent molecules to the region of the central cation.

3.7 Conclusions

In conclusion, in order to further elucidate the decoherence mechanisms at work in Cr_7Ni based MNMs, the synthesis of a group of compounds in which hydrogen is replaced by deuterium, fluorine or chlorine, was explored. Synthesis was found to be challenging, with many resulting compounds showing only partial substitution of H for the replacement atoms, or instability in ESR solvents. Phase memory times of the resulting stable compounds, all with hydrogen-, deuterium- or fluorine-substituted benzoate carboxylate ligands, were measured via pulsed ESR over the temperature range 3-5K. It was found that structural changes associated with the inclusion of fluorine atoms provided the dominant effect, modifying phase decoherence pathways and in particular, hindering decoherence driven by the central cation. However, the enhancement in phase memory time achieved by the inclusion of fluorine was no greater than that provided by solvent

deuteration or substitution of the central cation. Therefore, halogenation does not seem to provide a productive strategy for the improvement of phase memory time in Cr_7Ni based MNMs.

Chapter 4

Cr_7Ni-$N@C_{60}$: a Coherent Probe of Spin Dynamics

4.1 Introduction

The first requirement for physical implementation of quantum algorithms discussed in section 1.1.1 was scalability, and in the context of molecular spins, the simplest example of this is scaling up to a two qubit dimer. In this chapter and the next, we will explore two examples of such systems, beginning firstly with the asymmetric dimer: $N@C_{60}$(py)-Cr_7Ni, introduced below.

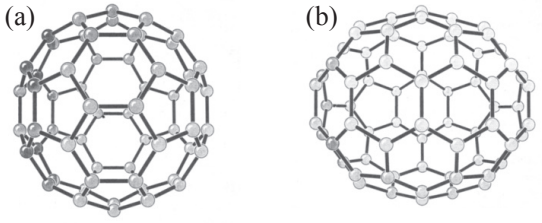

FIGURE 4.1: Structures of (a) C_{60} and (b) C_{70}. All balls represent carbon atoms. Adapted from [109].

Fullerene molecules form a family of carbon cages, which consist of various numbers of carbon atoms. Figure 4.1 shows the example structures of C_{60}, the first member of the group to be synthesised in 1985, and C_{70} [110]. It was subsequently shown that

implantation of an atom or small molecule within the fullerene cage, was possible. For example, lanthanum (La) was successfully implanted in C_{82}, sitting off centre in the cage and transferring to it three electrons, to form $La^{3+}C_{82}^{3-}$ [111–114]. An example of particular note is that of the nitrogen atom implanted in a C_{60} cage, known as N@C_{60}. In contrast to the case of La, N sits centrally and transfers only 2% of its electron density to the cage, a remarkable figure given its high reactivity [115, 116]. By virtue of its encapsulation in the C_{60} cage, the N spin ($s = 3/2$) exhibits extraordinarily long, environment-sensitive, decoherence times (up to $T_m = 0.23$ μs at $T < 20$ K in a CS_2/S_2Cl_2 mixture) [117]. This, coupled with the fact that N@C_{60} can be functionalised to form N@C_{60}-N@C_{60} dimers, has led to much exploration of its use as a molecular qubit [116, 118–122].

In the present chapter we examine a dimer, in which a N@C_{60} molecule is linked chemically to a Cr_7Ni ring (figure 4.2 (a)). The motivation for this is twofold: firstly, the dimer represents a two qubit system in which each spin is individually addressable due to its distinct g-factor (for N, $g \approx 2$ and for Cr_7Ni, $g \approx 1.8$). Perhaps even more interesting, however, is that the highly coherent nitrogen spin can be used to probe spin dynamics on the Cr_7Ni ring, with its phase memory time a direct reflection of the ring's dynamics. This idea is inspired by the principles underlying experimental techniques such as NMR, in which the T_1 time of a nucleus can be used to probe the frequency spectrum of electron spin fluctuations and muon spin rotation, in which the relaxation time of the muon reflects the spin dynamics of the surrounding electrons [123–126]. Such dynamics are at present highly relevant, also being studied, for example, in the contexts of superconductivity and quantum phase transitions [127–132]. The work in this chapter will examine the phase memory time of the N spin in our N@C_{60}(py)-Cr_7Ni dimer, as a function of temperature, comparing the results to those obtained for both a mixture of undimerised N@C_{60} and Cr_7Ni molecules and functionalised N@C_{60} alone, all with the aim of identifying different regimes of spin dynamics on the ring.

The chapter will begin by discussing all three samples in more detail. It will move on to present both CW and EFS data, with fits to characterise the spins. We will then examine the results of the variable temperature measurements of T_m for all three samples, along

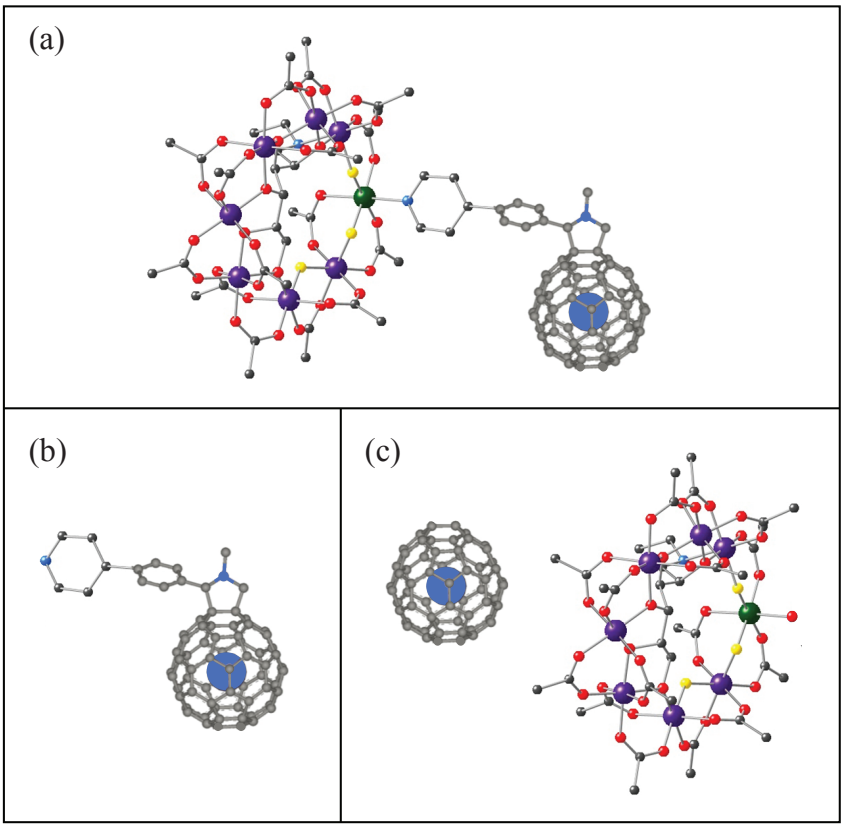

FIGURE 4.2: Structures of (a) the N@C_{60}(py)-Cr_7Ni dimer, (b) the N@C_{60}(py) monomer and (c) components of the N@C_{60}/Cr_7Ni mixture. The coloured balls represent C (grey), N (light blue), Cr (purple), Ni (green), F (yellow), O (red). Methyl groups of pivalates and ethyl groups of ether are omitted for clarity.

with a potential way to interpret them. The N@C_{60}(py)-Cr_7Ni dimer was synthesised by Benjamin Farrington (BF), of the Oxford Department of Materials and Grigore Timco (GT) of the University of Manchester. The functionalised N@C_{60}(py) monomers were prepared by BF. N@C_{60} molecules in the mixture were synthesised by Shen Zhou of the Oxford Department of Materials and the Cr_7Ni rings by GT. The sample was prepared by myself. ESR measurements on the dimer and functionalised monomer were taken in collaboration with BF. All measurements on the mixture are entirely my own. All analysis presented is my own.

4.2 Compounds and Samples

The caged N@C_{60} molecules were synthesised via ion implantation, in which a beam of nitrogen atoms is fired at a gas of C_{60} and subsequently condensed to give a N@C_{60} purity of approximately 6 x 10^{-3} % by mole. This was then purified to give a final purity of 8×10^{-2} % by mole [133]. A pyridine bridge was added to the C_{60} cages via an addition reaction to then give the N@C_{60}(py) monomer shown in figure 4.2(b).

The N@C_{60}(py)-Cr_7Ni dimer was formed by mixing C_{60}(py) (8×10^{-2} % of which contained an implanted N spin) and Cr_7Ni in the ratio 1:1.05 to promote dimerisation. Reaction pathways were tested firstly with 100% C_{60} and the chemically and structurally similar molecular magnet Cr_7Co, whose significantly weaker paramagnetism allowed characterisation of the product using ^{1}H NMR [133]. The specific Cr_7Ni ring used has a structure somewhat different to those described in section 3; ions in the Cr_7Ni ring are, as before, octahedrally coordinated, however, the bridging ligands vary around the ring (figure 4.2(c)) [84]. Instead of eight, there are now only three bridging fluorides, with the remaining five replaced by a polyalkoxide ($C_8H_{14}N_5H_5$). Seven out of eight edges are bridged by two pivalate ligands, with one Cr-Ni edge bridged by one only. Octahedral coordination is maintained by a link from the N of the polyalkoxide to the Cr and bonding of a water molecule (H_2O) to the Ni. The ring is overall charge neutral therefore, we do not require a central templating cation. In the dimerisation reaction, the water molecule is displaced and a bond formed between the Ni ion of the Cr_7Ni ring and the N of the pyridine in N@C_{60}(py) (figure 4.2(a)).

Three samples were prepared for ESR measurement. In all cases, the relevant molecules were dissolved in dry deuterated toluene, transferred under argon to a quartz ESR tube, degassed via the 'freeze-pump-thaw' method described in section 2.2.9, and flame sealed. They were then flash frozen before insertion for ESR measurement. The first sample contained the N@C_{60}(py)-Cr_7Ni dimer, with a N spin concentration of 4.8×10^{-7} M. Given that the C_{60} (including those both with and without an enclosed N spin) and Cr_7Ni were combined in the ratio 1:1.05, this resulted in a Cr_7Ni spin concentration of 6.3×10^{-4} M. This was chosen to strike a balance between reduction of instantaneous

diffusion due to the Cr_7Ni rings and enhancement of the N signal. The first of the two control samples was N@C_{60}(py), with a N@C_{60} spin concentration of 4.8×10^{-7} M. The second was a mixture of 'simple' N@C_{60} (without functionalisation to prevent dimerisation with Cr_7Ni rings), with a N spin concentration of 4.8×10^{-7} M, and Cr_7Ni rings at a concentration of 6.3×10^{-4} M. It should be noted that due to the light sensitivity of N@C_{60}, estimates of the N spin concentration are upper bounds [134–136].

The $s = 3/2$ electron spin of N is coupled isotropically to its nuclear spin. For the $> 99\%$ naturally abundant ^{14}N, this is $I = 1$. The resulting spin Hamiltonian, when the cage is functionalised, is

$$H = DS_z^2 + E(S_x^2 - S_y^2) + \mu_B g \boldsymbol{B}_0 \cdot \boldsymbol{s} + \mu_N g_N \boldsymbol{B}_0 \cdot \boldsymbol{I} + A\boldsymbol{S} \cdot \boldsymbol{I}. \tag{4.1}$$

Here, the fourth term represents the nuclear Zeeman energy, with μ_N the nuclear magneton and g_N the isotropic nuclear g-factor. The final term accounts for an isotropic hyperfine coupling between the N electron and nuclear spins, introducing an energetic preference for them to be antiparallel to one another, of strength characterised by A, the isotropic hyperfine coupling constant. In the absence of cage functionalisation, full symmetry is restored and both $D = 0$ and $E = 0$. The Cr_7Ni ring is, as for those we encountered in chapter 3, described by equation 1.6. The resulting spectrum of the N spin, in both cases, is hyperfine split into three characteristic narrow lines [137, 138].

In the case that N@C_{60}(py) successfully forms a dimer with Cr_7Ni, we expect an additional dipolar coupling between the two spins, given by

$$H_{dip} = \boldsymbol{s} \cdot \boldsymbol{J}_{dip} \cdot \boldsymbol{S}, \tag{4.2}$$

where s and S are the spins of the N atom and Cr_7Ni ground state, respectively, and $\boldsymbol{J}_{dip}$ is the dipolar coupling tensor. In the point-dipole approximation, $\boldsymbol{J}_{dip}$ is given by

$$\boldsymbol{J}_{\text{dip}} = J_{\text{dip}} \begin{pmatrix} -1 & & \\ & -1 & \\ & & 2 \end{pmatrix}; \quad J_{\text{dip}} = \frac{\mu_0 \mu_{\text{B}}^2 g_s g_S}{4\pi\hbar r_{1,2}^3}, \tag{4.3}$$

where g_s and g_S are the isotropic g-factors of the N and Cr_7Ni spins respectively [92].

4.3 ESR Measurements

Figure 4.3(a) shows a CW ESR spectrum of the N@C_{60}(py)-Cr_7Ni dimer, recorded at $T = 10$ K. We note the separation in field of the N@C_{60} and Cr_7Ni resonances (at $B_0 \approx 0.335$ T and $B_0 \approx 0.368$ T, respectively), reflecting their distinct g-factor values. We also note that the linewidth of the ring's resonance is significantly greater than that of the N spin. In order to characterise the Cr_7Ni ring, the spectrum was fitted with a uniaxial g-factor and H-strain, to account for unresolved hyperfine interactions with surrounding nuclei. The parameters obtained were $g = [1.833\ 1.833\ 1.768]$ and $H_{\text{strain}} = 250$ MHz. Due to the extremely long relaxation time of N@C_{60} at low temperature, as evidenced by its narrow linewidth, CW measurements of the N@C_{60} part of the spectrum were additionally carried out at the increased temperature of 90 K (figure 4.3(b)) in order to prevent signal saturation. We note here the three lines characteristic of both 'pure' and functionalised N@C_{60}, with two further peaks outside this region. These appear only for the functionalised form, whose symmetry is broken by the attached chemical linker, and are characterised by the zero field splitting terms D and E, both of which must be included in order to find a good fit to the data. The optimal fit to equation 4.1, returned the values: $g = 2.0023$, $D = 14.62$ MHz, $E = 0.21$ MHz and $A = 15.73$ MHz, with a Gaussian linewidth, $\Delta B_0 = 0.056$ mT. These are typical for functionalised N@C_{60}(py), showing that any dipolar interaction with the Cr_7Ni ring does not influence the N spin's spectrum at this temperature.

Given that 99.92% of Cr_7Ni rings in the dimer sample were connected to an empty C_{60} cage their investigation would not have revealed any information on the ring's interaction with the N spin. Therefore, all subsequent measurements were performed solely on the

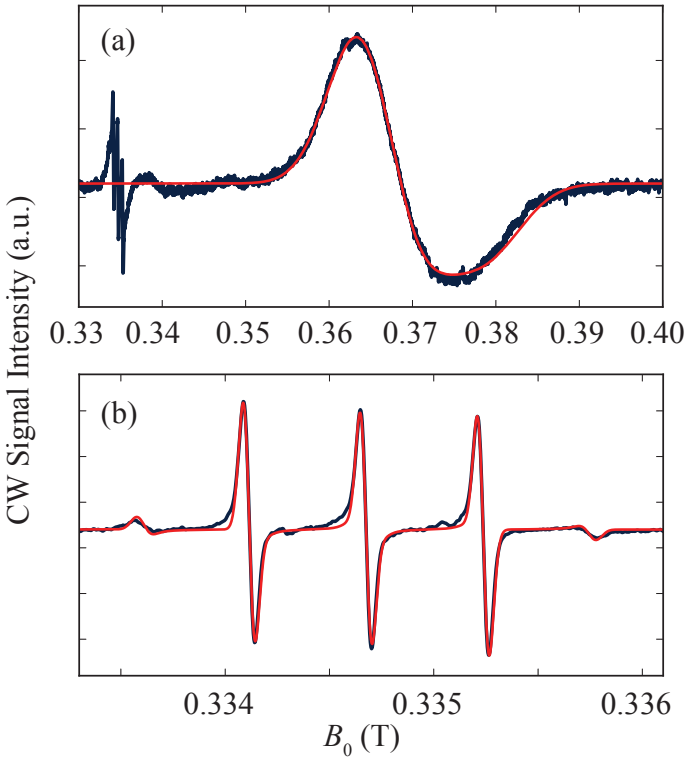

FIGURE 4.3: CW ESR spectra of N@C_{60}(py)-Cr_7Ni. (a) Spectrum recorded at T = 10 K with ν = 9.380 GHz (dark blue line) and modulation amplitude, $\Delta B_0 = 3.0 \times 10^{-5}$ G; fit to the ring's signal at $B_0 \approx 0.368$ T (red line), with a uniaxial g-tensor [1.833 1.833 1.768] and an isotropic Gaussian H-strain accounting for unresolved hyperfine interactions, H_{strain} = 250 MHz. (b) Spectrum recorded at T = 90 K with ν = 9.379 GHz and modulation amplitude, $\Delta B_0 = 3.0 \times 10^{-5}$ G, focused on the region of the N@C_{60} signal (dark blue line); fit (red line), with an isotropic g-factor, $g = 2.0023$, Gaussian linewidth, $\Delta B_0 = 0.056$ mT, zero field splittings, D = 14.62 MHz and E = 0.21 MHz and isotropic hyperfine coupling to the $s = 1$ ^{14}N nucleus, A = 15.73 MHz.

N@C_{60} component. The greater concentration of Cr_7Ni spins is reflected by figure 4.3, from which we see that the integrated signal amplitude is much greater for the Cr_7Ni signal than for that of the N@C_{60}.

For all three samples, echo detected field sweeps were performed at various temperatures using a Hahn echo sequence with a 160 ns π-pulse, delay time, τ = 2000 ns and two-step phase cycle. For these measurements, and all further pulsed ESR presented in this chapter, at each temperature, the shot repetition time was adjusted to give a reasonable compromise between the time taken to perform a measurement and signal saturation due to the long T_1 time of N@C_{60}. From figure 4.4(b) and (c), we see that for both the monomer and mixture, we obtain the characteristic three line spectrum expected for N@C_{60}, and that this retains the same shape, down to temperature T = 2.5 K. For the

dimer, however, figure 4.4(a) shows that this is not the case. At $T = 8$ K, the spectrum resembles those of the dimer and mixture, however, as we cool to lower temperatures, it develops a new feature, most notably additional peaks between the original three. We attribute this to dipolar interaction with the Cr_7Ni ring.

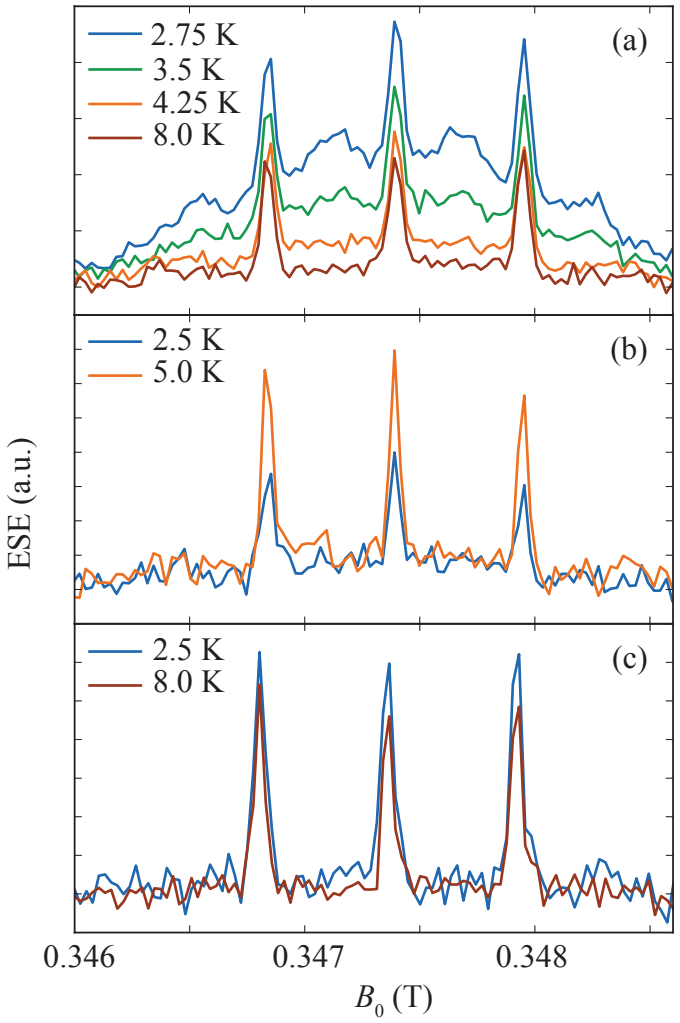

FIGURE 4.4: EFS at variable temperature for (a) N@C_{60}(py)-Cr_7Ni dimer, (b) N@C_{60}(py) monomer and (c) N@C_{60}/Cr_7Ni mixture. (a) recorded at $\nu = 9.737$ GHz, (b) recorded at $\nu = 9.737$ GHz and (c) recorded at $\nu = 9.748$ GHz. (b) and (c) are scaled to $\nu = 9.737$ GHz for ease of comparison.

Figure 4.5 explores EFS data for the dimer in more detail. In panel (a), the $T = 8$ K trace is presented along with a fit to equation 4.1. To obtain this, values for the parameters g, D, E and A were taken from the CW fit in figure 4.3(b), and the Gaussian linewidth was varied. This strategy was chosen as the extremely narrow linewidths of N@C_{60} make them highly susceptible to experimental distortion, for example, in CW data, due to the modulation amplitude or in EFS data, due to the finite bandwidth of a π-pulse.

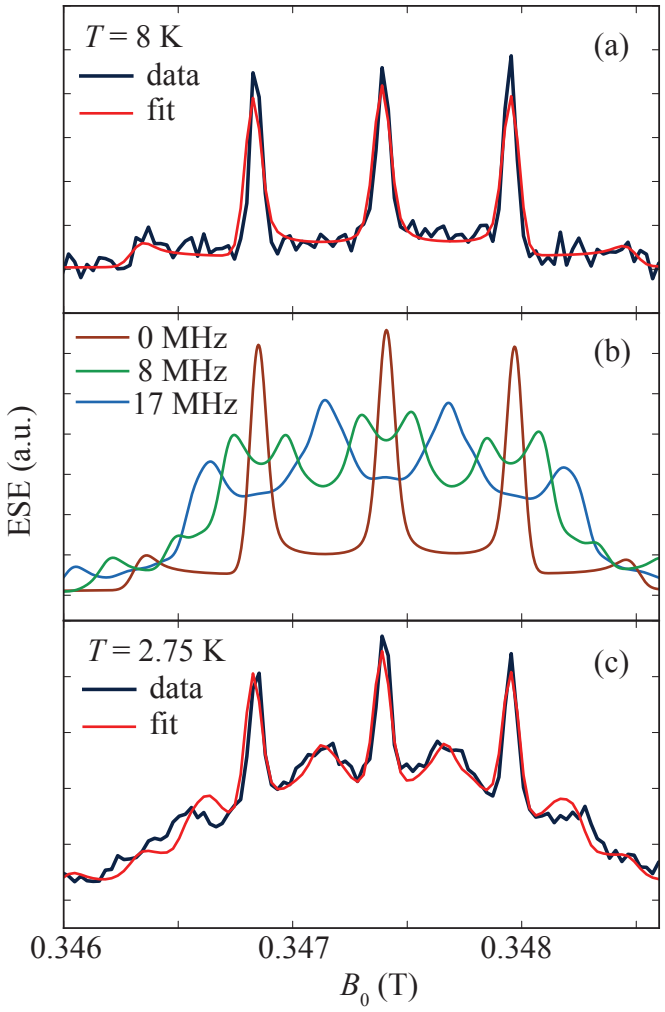

FIGURE 4.5: EFS data and simulation for N@C_{60} region of N@C_{60}(py)-Cr_7Ni spectrum, with $\nu = 9.737$ GHz. (a) Data at $T = 8$ K (dark blue line) and fit (red line). For fit, isotropic g-factor, $g = 2.0023$, zero field splittings, $D = 14.62$ MHz and $E = 0.21$ MHz and isotropic hyperfine coupling to the $s = 1$ ^{14}N nucleus, $A = 15.73$ MHz were taken from the CW fit of figure 4.3. Gaussian line width varied and an optimum value, $\Delta B_0 = 0.0703$ mT, was returned. (b) Simulated spectra, with parameters taken from (a), in the absence of dipolar coupling to the Cr_7Ni spin (brown line) and with dipolar couplings of $J_{dip} = 8$ MHz (green line) and $J_{dip} = 17$ MHz (light blue line). (c) Data at $T = 2.75$ K (dark blue line) and fit (red line). Fit assumes parameters taken from (a) and that we have a mixture of N spins, some with $J_{dip} = 0$ MHz and some $J_{dip} = 17$ MHz. Relative population size optimised to give the percentage of nitrogen spins experiencing a $J_{dip} = 17$ MHz dipolar coupling as 64.3%.

This could cause a difference in the measured linewidth between CW and EFS data. The linewidth obtained was $\Delta B_0 = 0.0703$ mT and the fit represented the data well, confirming that dipolar interaction with the Cr_7Ni ring does not influence the N spin's spectrum at this temperature.

In order to explain the additional features in the $T = 2.75$ K spectrum, we turn firstly

to figure 4.5(b), which shows simulated spectra for N@C_{60}, with fit parameters taken from (a), without dipolar coupling to the Cr_7Ni ring, and with dipolar couplings $J_{\text{dip}} =$ 8 MHz, and $J_{\text{dip}} = 17$ MHz. These were chosen as they correspond to the two expected conformations of the dimer: the first with N at a distance 1.8 nm from the centre of the ring, known as the 'anti' conformation and the second with N at a distance 1.4 nm from the ring's centre, known as the 'eclipsed' conformation [133]. The J_{dip} values were calculated via equation 4.3 using the g-vales obtained from our CW data. In the case of the ring, an isotropic g-value of $g = 1.811$ was used, the weighted average for a spherical distribution of spins. One can see immediately that features of the $J_{\text{dip}} = 17$ MHz spectrum closely resemble those in our $T = 2.75$ K data (panel (c)). From this we assume our dimers are in an 'eclipsed' conformation. Given the appearance in the $T = 2.75$ K spectrum of spectral features for N@C_{60}(py) both with and without a $J_{\text{dip}} = 17$ MHz dipolar coupling, and the expectation that only some of our N@C_{60}(py) dimerised successfully, we postulate that what we are seeing is the signal from a mixture of dimers and monomers. Panel (c) shows the $T = 2.75$ K data fitted, assuming such a mixture and and varying the percentage of each component. The optimal fit was found for a mixture in which 64.3% of the N@C_{60}(py) molecules had successfully formed dimers. We must remember, however, that this is only an estimate as any difference in T_{m} time between the two types of molecule would distort this value, leading to an artificially higher percentage of the species with a larger T_{m}, such that its echo was stronger at the point of measurement. Exploration of these times forms the next part of our investigation.

Phase memory times of all three samples were measured as a function of temperature using X-band pulsed ESR, applying the standard Hahn echo sequence, '$\pi/2 - \tau - \pi - \tau -$ echo', with a 160 ns π-pulse and two-step phase cycle, as discussed in section 2.2.3. Measurements were performed on the lowest field line of the N spin's trio of resonances. At lower temperatures, this may have resulted in a favouring of signal due to undimerised molecules, given their relative signal strength compared with dimerised molecules at this field position. However, it was unavoidable if we were to achieve consistent measurement across all temperatures as in the high temperature region, there is little signal away from the three principal resonances. The resulting decay curves were found to best fit the

stretched exponential function given by equation 3.1, without an instrumental offset, such that the extracted parameters were T_m and x. We can alternatively consider the former as a decoherence *rate* (T_m^{-1}), the sum of the individual decoherence rates resulting from each contributing mechanism. All results are presented in the next section.

4.4 Results and Interpretation

Figure 4.6 compares the T_m, T_m^{-1} and x data obtained for the dimer and monomer. At temperatures below about 50 K, we see the phase memory time of the N@C_{60}(py) sample decrease with decreasing temperature. Typically, endohedral fullerenes in deuterated toluene show a minimum in T_m around 14 K, attributed to the slow rotation of solvent methyl groups [139]. That we do not see this suggests that at low temperature, the dominant source of decoherence in the uncomplexed case is rather, slow motional modes within the attached bridge. This is supported by a stretch parameter x, which decreases with decreasing temperature, as a slowing of the dominant motional mode increases its decoherence effect [99]. The T_m values of the N@C_{60}(py)-Cr_7Ni complex show a similar gentle decrease with decreasing temperature, down to approximately 15 K. However, between the temperatures of 10 K and 3 K, we see the emergence of a dramatic new feature, most visible in the plot of decoherence rate (panel (b)). This, we attribute to the magnetisation dynamics of the Cr_7Ni ring. At this stage, we also note that at $T = 2.5$ K the T_m times for the dimer and monomer are fairly similar, indicating that the estimate made of the successfully dimerised population in figure 4.5, was not biased by a difference in phase memory time.

Due to the dipolar interaction between them, spin transitions on the Cr_7Ni ring cause magnetic field fluctuations at the N spin sites. These, in turn, give rise to fluctuating terms in the N spin Hamiltonian:

$$H_\mathrm{fluct} = \sum_{i=x,y,z} C_i(t)\sigma_i, \tag{4.4}$$

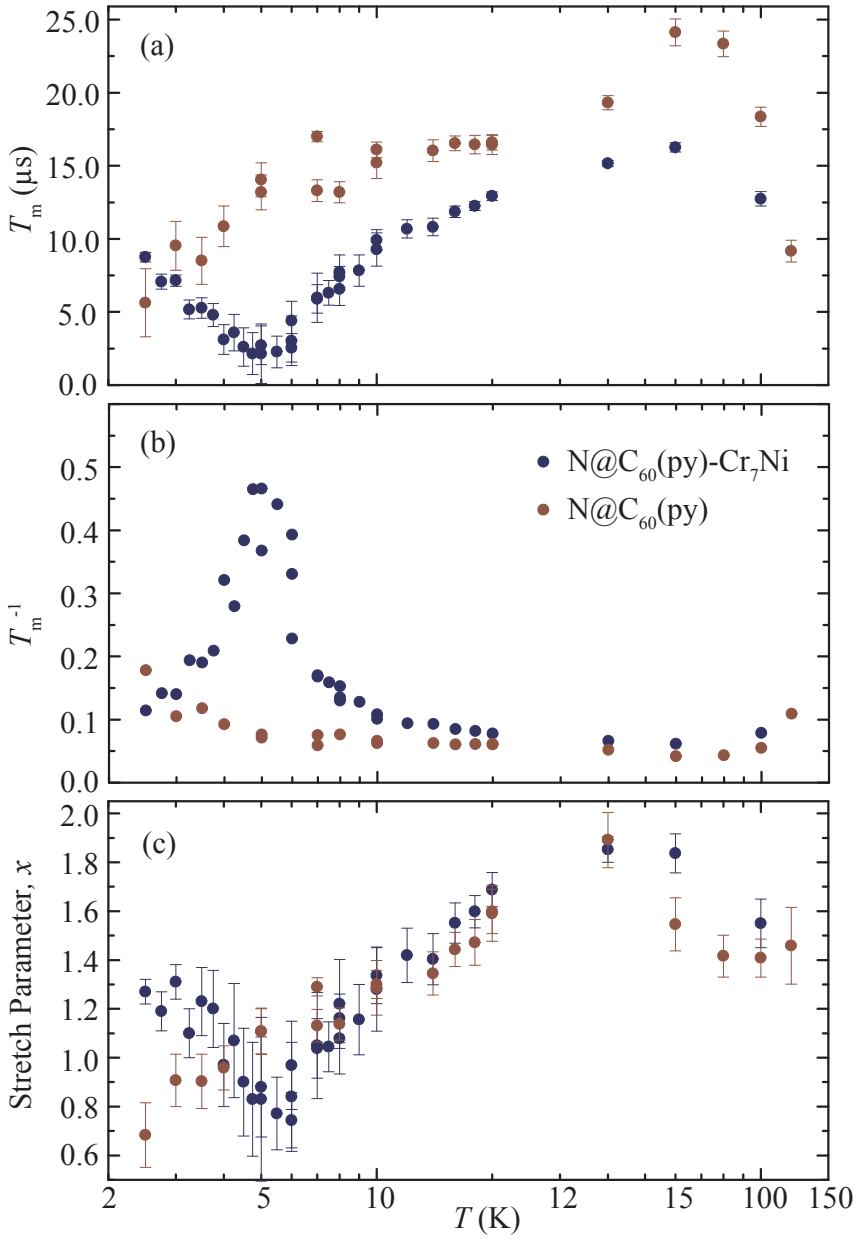

FIGURE 4.6: Phase memory time, T_m (a), decoherence rate, T_m^{-1} (b) and stretch parameter, x (c) for the N@C_{60}(py)-Cr_7Ni dimer (dark blue circles) and N@C_{60}(py) monomer (dark red circles). All were recorded using the standard Hahn echo sequence and a π-pulse length of 180 ns. B_0 was tuned to the lower field line of the N@C_{60} spectrum at high temperature, and was then kept constant throughout.

where $C_i(t)$ characterises the size of the fluctuating term and absorbs the magnetic field fluctuation, $B_i(t)$, at the site of the N spin. σ_i is the relevant sigma matrix. The x and y components drive longitudinal relaxation and, assuming the longitudinal relaxation time $T_1 > T_m$, do not affect T_m. The z component, however, provides an additional contribution to phase relaxation. It is characterised by its autocorrelation function,

$$G(\tau) = \langle C_z(t)C_z(t+\tau)\rangle = \left\langle C_z^2 \right\rangle \exp\left(\frac{-|\tau|}{\tau_c}\right). \tag{4.5}$$

The first form provides the definition and the second is the functional form characteristic of the thermal excitation of a mode with relaxation time, τ_c. Here, angular brackets denote a time average. In the case that we have fluctuations on multiple timescales, we have a sum of such functions. We expect that the magnitude of C_z is governed by two factors: the absolute size of the magnetic field fluctuations at the Cr_7Ni sites, and the distribution of dipolar coupling strengths between the ring and the N spin. The coupling strength between any given two spins is inversely proportional to the cube of their separation (equation 4.3). We expect τ_c to reflect both the intrinsic energy level structure of the ring and its surrounding environmental phonon bath, which provides energy, thereby inducing transitions between these.

Alternatively, one can consider the frequency spectrum:

$$I(\omega) = FT\left[G(\tau)\right] = \left\langle C_z^2 \right\rangle \frac{2(1/\tau_c)}{(1/\tau_c)^2 + \omega^2}, \tag{4.6}$$

given by the Fourier Transform of $G(\tau)$. For a spectrum of fluctuations characterised by a single τ_c, we get a frequency distribution that is Lorentzian, with halfwidth, $\omega_c = \tau_c^{-1}$. Alternatively, in the case that there are fluctuations occurring on multiple timescales, we expect the frequency distribution to be Gaussian. It has been shown, by NMR and subsequent theoretical calculation, that fluctuations on the ring, do in fact decay over a single timescale [123, 140]. Therefore, we will assume that our frequency distribution is Lorentzian, with a temperature dependent halfwidth. This is expected to increase with increasing temperature, as the higher energy phonon bath induces more rapid fluctuations. At low temperature ($T \lesssim 8$ K), we expect that $\left\langle C_z^2 \right\rangle$ starts to decrease, eventually tending to zero as the coherent ground state is formed and fluctuations are frozen out. This corresponds to the temperature at which the ground state of the ring is sufficiently coherent that it permits the observation of a spin echo in experiments conducted directly on the Cr_7Ni $S = 1/2$ Zeeman transition [89].

Having examined fluctuations on the Cr_7Ni ring, we must now consider the effect that these will have on the phase memory time of our N spins. For a given amplitude of fluctuation, we expect that its efficacy in driving decoherence in a Hahn echo experiment, will be determined by its characteristic timescale, τ_c, with respect to the timescale of the interaction. This is governed by the strength of the dipolar interaction: $\tau_{dip} \sim \omega_{dip}^{-1}$. When there is a fluctuation on the ring, the N spin experiences a corresponding change in B_z, which must be either strong or long enough to cause a change in the phase of the precessing N spin. For the 1.4 nm separation within the 'eclipsed' molecule, the dipolar interaction strength corresponds to a timescale ~ 0.058 μs. Interaction with a single Cr_7Ni ring on a neighbouring molecule at an average distance of 14 nm, corresponds to a timescale, $\tau_{dip} \sim 58$ μs. Fluctuations rapid with respect to the relevant timescale will average to zero, as they will relax before any significant phase difference has been acquired by the N spin. However, as they slow towards the interaction timescale, they will become highly effective in driving decoherence. This will continue to be true until the fluctuation timescale slows down so much that it reaches that of the Hahn echo experiment, on the order of T_2. In this regime, the phase differences acquired will be partially refocused. We note that refocusing of slow fluctuations will be less effective at initial time points with a shorter wait time between pulses, such that as we move to subsequent time points, the signal decay is enhanced. This leads to a 'super exponential' form reflected by a reduced stretch parameter.

Turning back to figure 4.6, we can begin to understand the data. At high temperature, fluctuations are rapid, and have little effect on decoherence. At the peak in T_m, around $T = 5$ K, there is a high intensity of fluctuations within the effective window of timescales and therefore rapid decoherence is driven. At low temperature, fluctuations are frozen out, such that the decoherence rate decreases and the coherent ground state is formed. This is illustrated by figure 4.7, in which Lorentzian distributions of different halfwidths with respect to the dipolar interaction frequency, are plotted. Neutron scattering reveals the Cr_7Ni ring's first excited state, of spin $S = 3/2$, to occur approximately 14 K above the ground state. The next group of excited states is closely spaced and begins at 32 K above the ground state [81]. Therefore, in the region of interest, we expect fluctuations to be due primarily to the ground to first excited state transition, with the same amplitude

regardless of temperature. Before fluctuations between these states begin to be frozen out, we assume $\langle C_z^2 \rangle$ is roughly temperature independent for a given dipolar distribution. Below $T \lesssim 8$ K, as discussed, we expect a reduction in $\langle C_z^2 \rangle$ due to the fluctuations being frozen out. We see that the greatest integrated intensity of transitions at frequencies $\omega < \omega_{\text{dip}}$ occurs for an intermediate τ_c, such that, as observed, as we cool, there is a peak in the decoherence rate, which then falls back down as $\langle C_z^2 \rangle$ decreases. We also note that in the region of rapid decoherence, the stretch parameter is reduced. This indicates that fluctuations may be slowing to the timescale of the T_2 experiment.

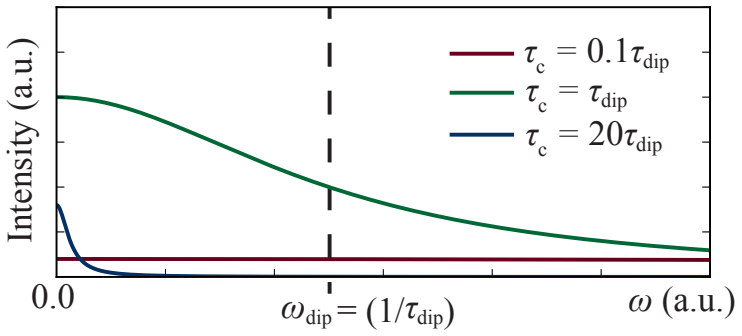

FIGURE 4.7: Lorentzian frequency spectra, as described by equation 4.6, for three different correlation timescales: $\tau_c = 0.1\tau_{dip}$ and $\tau_c = \tau_{dip}$ when $\langle C_z^2 \rangle = 1$; $\tau_c = 20\tau_{dip}$ when $\langle C_z^2 \rangle = 0.02$. We see that the integrated intensity below ω_{dip}, is greatest for the $\tau_c = \tau_{dip}$ curve.

In order to separate the decoherence effects of fluctuations within the N@C_{60}(py)-Cr_7Ni dimer and with the surrounding distribution of rings, we turn to figure 4.8, which compares data for the dimer and mixture. We see that results for the mixture follow a similar trend to the dimer. At high temperature, decoherence rate is low, then, as we cool, we reach a peak at around $T = 5$ K, and finally the decoherence rate decreases again. However, it appears that in the case of the mixture, the peak in decoherence rate, is narrower. This is likely due to the broader distribution of dipolar interaction energies present in the case of the dimer. At high temperature, when fluctuations are rapid, decoherence in the dimer is driven by fluctuations slower than the timescale of the intra-dimer interaction. However, in the case of the mixture, these are still too rapid to be effective. At lower temperatures, fluctuations due to the distribution of surrounding molecules become effective, and their effect is amplified by there being a large number of spins surrounding the N, on the same order of separation.

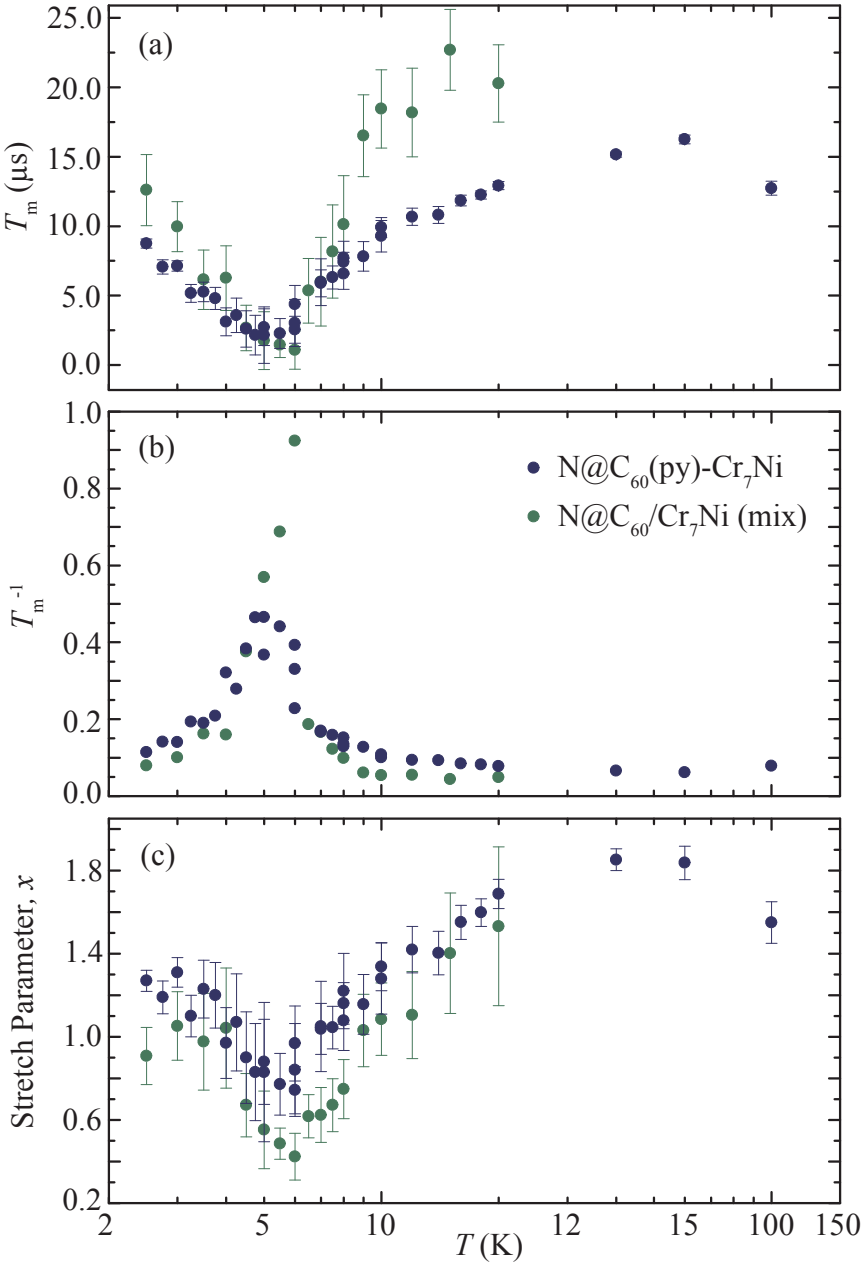

FIGURE 4.8: Phase memory time, T_m (a), decoherence rate, T_m^{-1} (b) and stretch parameter, x (c) for the N@C_{60}(py)-Cr_7Ni dimer (dark blue circles) and N@C_{60}/Cr_7Ni mixture (dark green circles). All were recorded using the standard Hahn echo sequence and a π-pulse length of 180 ns. B_0 was tuned to the lower field line of the N@C_{60} spectrum at high temperature, and was then kept constant throughout.

4.5 Conclusions

In conclusion, motivated by its potential use both as a two qubit dimer and a way to probe spin dynamics on the Cr_7Ni ring, we have used ESR to explore a N@C_{60}(py)-Cr_7Ni dimer. The dimer was characterised using both CW and EFS data, and, using features

in the N spin's low temperature EFS data, attributed to the dipolar interaction with the Cr_7Ni ring, it was estimated that approximately 63.4% of N@C_{60}(py) molecules had successfully dimerised. Measurements of the phase memory time and decoherence rate of the N spin were presented over a range of temperatures ($T = 2.5$ K to $T = 130$ K) for the N@C_{60}(py)-Cr_7Ni dimer and compared to those obtained for both N@C_{60}(py) monomers alone, and a N@C_{60}/Cr_7Ni mixture. The measurements successfully provided insight into the magnetisation dynamics of the Cr_7Ni ring. We have identified three distinct regimes: the first at high temperature, where fluctuations on the ring are so rapid that the N@C_{60} appears magnetically disconnected. As these magnetic fluctuations begin to slow towards the timescale of the dipolar interaction between Cr_7Ni and the N spin, we see a sharp rise in the decoherence rate of the N spin, peaking at $T \approx 5$ K. At the lowest temperatures, a recovery of the relaxation rate reflects the onset of the ring's coherent ground state. It was found that the peak in decoherence rate as a function of temperature was broader in the case of the dimer, reflecting the broader distributions of dipolar interaction energies experienced by the N spins.

Chapter 5

Cr_7Ni-Cr_7Ni Dimers: towards Entanglement

5.1 Introduction

In chapter 4 we presented the asymmetric dimer, $N@C_{60}(py)$-Cr_7Ni, whose two components have distinct g-factor values (for N, $g \approx 2$ and for Cr_7Ni, $g \approx 1.8$), thereby allowing us to address each one individually. However, what this dimer does not allow is control of its two spins simultaneously. This is because, for a given B_0, their resonant frequencies have a separation greater than the bandwidth of our ESR cavity. In the present chapter we will explore instead a group of symmetric dimers, formed from two identical Cr_7Ni rings. While one might assume that use of identical spin components would result in loss of the ability to address each one individually, this is not the case. The spins show significant g factor anisotropy (≈ 3 %) and our molecules are flexible, therefore we expect that, in a given molecule, there will be some difference in the rings' orientations with respect to B_0, leading to a difference in g-factor. This allows us to address them individually and is small enough that we can do so simultaneously.

In order to move further towards the implementation of quantum algorithms in a dimer, we must investigate not only properties of the individual qubits, but also the coherent couplings between them, essential for the controlled formation of entangled states. This

should be done bearing in mind three key timescales, relative to one another: T_m, the phase memory time of an individual qubit, must be the longest; h/J (with J the inter-qubit interaction energy) is characteristic of the duration of a two qubit gate and should be intermediate; and the single qubit manipulation time should be the shortest. Phase memory times of the Cr_7Ni ground state are typically within the range 1-10 μs at low temperature and in a pulsed ESR experiment we can manipulate them on the 10 ns timescale [88, 89]. Therefore, an interaction offering h/J in the 100 ns range would be the most readily exploitable. It is this that we want to measure in our group of Cr_7Ni-Cr_7Ni dimers using the technique known as double electron-electron resonance (DEER). Our aim will be to identify which systems, if any, obey the relevant hierarchy of timescales.

DEER is a technique that utilises the fact that, if there is a magnetic interaction between two spins, the coherent precession rate of one is modified by an inversion of the spin state of the other, with a stronger interaction inducing a greater change. Although originally applied to inorganic systems, it has been used extensively in the investigation of biological systems, for example proteins [92, 141–144]. These are labelled by ESR active molecules, for example nitryl nitroxides, at specific sites. The measured dipolar coupling between the spin labels is used to reveal their separation, providing insight into the structure of the system [145].

The chapter will begin by presenting the group of Cr_7Ni-Cr_7Ni dimers investigated. It will move on to present CW data and fits used to characterise the individual rings. The phase memory times for each compound at $T = 2.5$ K, as measured by the standard Hahn echo sequence, are presented. We then examine in more detail the pulse sequence of the DEER experiment. The resulting data for each compound are presented, accompanied by a discussion of both the data and feasibility of the compounds for use in implementing two qubit quantum gates. We end by presenting an outlook for use of these dimers in more advanced two qubit experiments in the near future. Samples were synthesised by Grigore Timco and Antonio Fernandez of the University of Manchester. ESR experiments were carried out in collaboration with Dr Alice Bowen of Oxford Department of Physics. DEER traces for samples **1D** and **2B** were 'stitched' by Dr Alice

Bowen. All other analysis and simulation presented here is entirely my own.

5.2 Compounds

Figure 5.1 shows the structures of the dimers investigated in this chapter. All of these consist of two coupled Cr_7Ni rings of ground state spin $S = 1/2$, as discussed in chapter 1. However, the ligands on the rings and linking strategy divide them into two main groups.

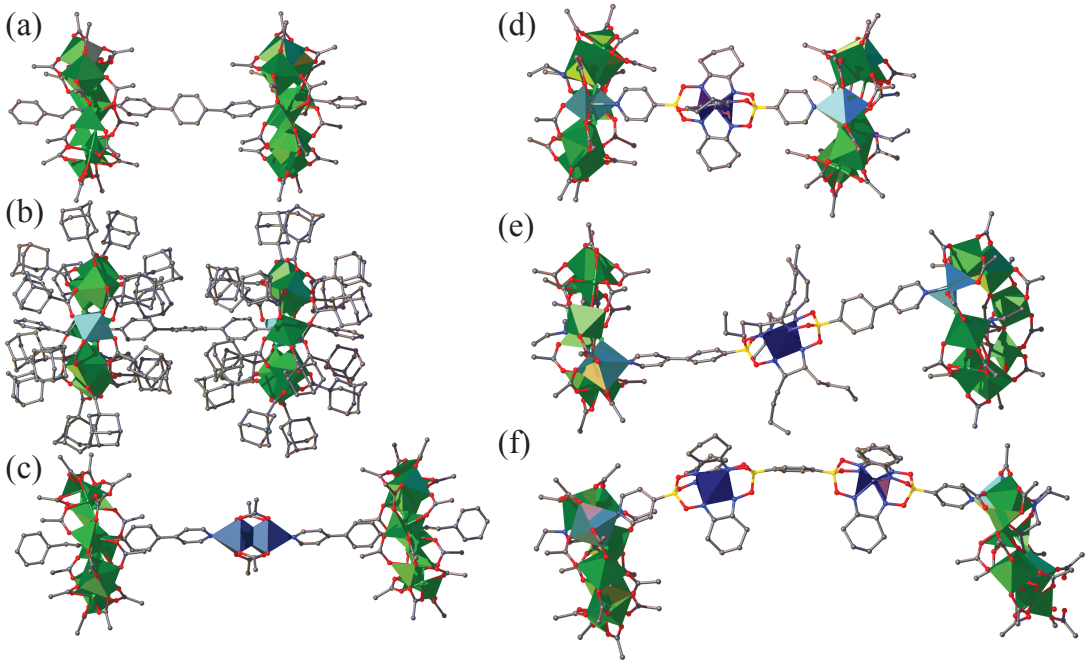

FIGURE 5.1: Structures of the two Cr_7Ni ring dimers investigated in this chapter. The atoms present are Cr (green octahedra), Ni (light blue octahedra), other metals (dark blue octahedra), O (red balls), C (grey balls), N (blue balls), B (yellow balls). (a) $\{[H_2\mathbf{T1}][Cr_7NiF_8(O_2C^tBu)_{16}]_2\}$ **1A** (**1B** is very similar, differing only by the stopper on the thread); (b) $\{[H_2\mathbf{T1}][Cr_7NiF_8(O_2CAd)_{16}]_2\}$ **1C**; (c) $\{[H\mathbf{T3}][Cr_7NiF_8(O_2C^tBu)_{16}]\}_2[Rh_2(O_2CMe)_4]$ **1D**; (d) $\{[Cr_7NiF_3(Etglu)(O_2C^tBu)_{15}]_2L1\}$ **2A**; (e) $\{[Cr_7NiF_3(Etglu)(O_2C^tBu)_{15}]_2L2\}$ **2B**; (f) $\{[Cr_7NiF_3(Etglu)(O_2C^tBu)_{15}]_2L3\}$ **2C**. Methyl groups of pivalates and ethyl groups of ether are omitted for clarity.

The first group of compounds is the 'rotaxanes', which consist of two Cr_7Ni rings threaded on a rigid axle. The type of ring used to form this group is the same as those presented in chapters 1 and 3, with the difference that instead of a central templating cation, the axle passes through the centre of the ring. In these compounds, there is no covalent bonding between the two rings therefore we expect the magnetic

interaction between them to be entirely dipolar, dependent upon the separation of the rings and the orientation of the axle with respect to B_0.

For compounds **1A**, **1Bd** and **1C**, the rigid axles are very similar and have the chemical formula [R-CH_2CH_2-NH-CH_2-$(C_6H_4)_3$-CH_2-NH-CH_2CH_2-R] (**T1**: R = Ph; **T2**: R = CH_2CHMe_2). The carboxylate bridging ligands of **1A** and **1Bd** are pivalate ($O_2CCH(CH_3)_3$), with the H exchanged for D in **1Bd**, motivated by a possible enhancement of T_m. In compound **1C**, the carboxylate ligand is, in contrast, formed from rigid adamantane groups, shown in figure 5.1(b), motivated again by a possible increase in T_m, this time by reducing the mobility of attached H nuclei. These were all synthesised by threading the axle through two rings and then attaching a chemical 'stopper' on the end.

By contrast, **1D** was synthesised by threading the linker [Ph-CH_2NH_2-CH_2-C_6H_4-Py] (**T3**: Py = C_5H_4N) through one ring and then attaching the ends of two of these to the metal complex $[Rh_2(O_2CMe)_4]$. This strategy allowed the formation of an axle of length longer than would have been possible directly due to the insolubility of the relevant 'double' organic axle. The carboxylate bridging ligand in this case was pivalate. Table 5.1 gives the separation of the Cr_7Ni ring centroids for each rotaxane dimer.

The second group of compounds is based on the variety of Cr_7Ni ring described in section 4.2. Just as the water molecule was displaced by the functional group of the $N@C_{60}$(py) molecule to form $N@C_{60}$(py)-Cr_7Ni, each end of the relevant chemical linker displaces an H_2O and forms a bond with a ring. Each of the dimers has a different linker, from shortest to longest: **2A** (L1), **2B** (L2) and **2C** (L3). The structures of these linkers are shown in appendix A. They are more flexible than the rotaxane axles. The shortest metal-metal distances in the compounds are the Ni-Ni distances: 1.89 nm, 2.71 nm and 3.07 nm, for **2A**, **2B**, **2C** respectively. The largest Cr-Cr distances are 2.24 nm, 3.24 nm and 3.55 nm, respectively.

Full synthetic details are beyond the scope of this thesis and can be found in the supplementary information of the relevant paper [146].

5.3 CW ESR and T_m Measurements

Samples were dissolved in either dry hydrogenated (samples **1A**, **1Bd**, **1C**, **2B**) or dry deuterated (**1D**, **2A**, **2C**) toluene, such that the concentration was either 100 μM (samples **1A**, **1Bd**, **1C**) or 200 μM (samples **1D**, **2A**, **2B**, **2C**). Solvent was chosen as a compromise between extension of T_m by deuteration and introduction of deuterium ESEEM, which is difficult to remove in DEER experiments. Concentration was chosen as a compromise between enhancement of signal strength and reduction of T_m due to instantaneous diffusion. Samples were transferred to a 3 mm quartz ESR tube and flash frozen before insertion for ESR measurement.

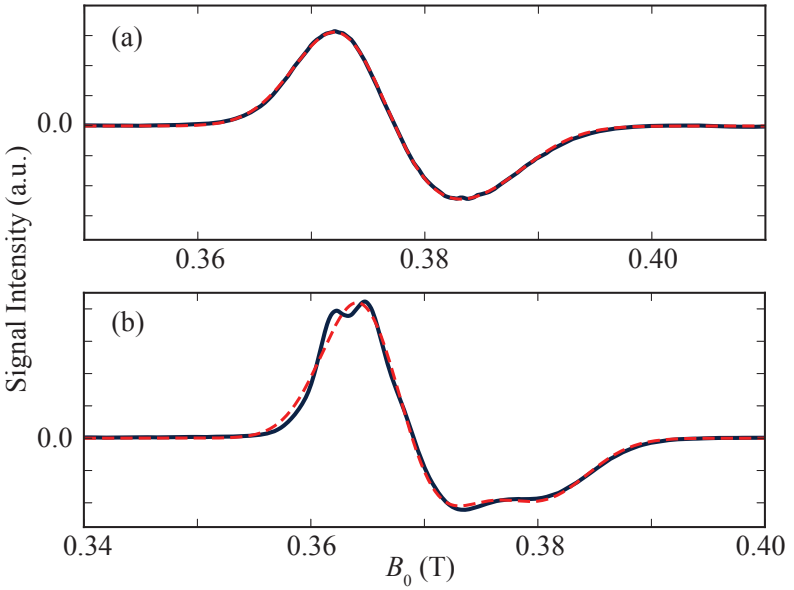

FIGURE 5.2: Example CW ESR spectra. (a) X-band CW ESR spectrum of compound **1A** at 9.3878 GHz (dark blue line) and EasySpin simulation (red dashed line). Simulation assumed a uniaxial g-tensor and included an isotropic Gaussian FWHM energy broadening (H-strain), which accounts for unresolved hyperfine splittings. Optimised parameters were g = [1.791 1.791 1.739], with an H-strain = 253 MHz. (b) X-band CW ESR spectrum of compound **2A** at 9.3878 GHz (dark blue line) and EasySpin simulation (red dashed line). Data was simulated as for (a), giving g = [1.832 1.832 1.761] and an H-strain = 223 MHz.

Figure 5.2 shows X-band CW spectra for compounds **1A** and **2A**, recorded at T = 2.5 K, along with the corresponding simulations, which allowed a uniaxial g-factor and isotropic Gaussian broadening due to unresolved hyperfine splittings. It was found that an anisotropic broadening or g-factor with three distinct principal components did not improve the fit in either case. The spectrum of **2A** shows more structure than that of

1A. This is due to it being more anisotropic as a result of the reduced symmetry of the Cr_7Ni rings from which it was synthesised. Both spectra are essentially indistinguishable from the spectra of the corresponding monomers, therefore we conclude that the ring-ring interaction energy is small, compared to the ESR linewidth. This is in contrast to previously synthesised Cr_7Ni-Cr_7Ni dimers, which had an inter-ring interaction strength so high (between $h \times 0.3$ GHz and $h \times 10$ GHz) that there was a clear splitting observable in the CW ESR spectra that was not present in those of the monomers [147]. CW spectra for all other dimers in groups **1** and **2**, were almost identical to those of compounds **1A** and **2A**, respectively. The fit parameters for all compounds are presented in table 5.1.

TABLE 5.1: Parameters for each compound, obtained by simulation of X-band CW data, using EasySpin. Simulation assumed a uniaxial g-tensor and allowed an isotropic Gaussian FWHM energy broadening (H-strain), which accounts for unresolved hyperfine splittings. Bracketed distances give the separation of the Cr_7Ni ring centroids for **1A**, **1Bd**, **1C** and **1D** and the Ni-Ni distances for compounds **2A**, **2B** and **2C**.

Compound	g-tensor	H-strain (MHz)
1A (1.64 nm)	[1.791 1.791 1.739]	253
1Bd (1.64 nm)	[1.796 1.796 1.742]	255
1C (1.64 nm)	[1.794 1.794 1.741]	285
1D (2.50 nm)	[1.790 1.790 1.740]	260
2A (1.89 nm)	[1.832 1.832 1.761]	223
2B (2.71 nm)	[1.835 1.835 1.771]	220
2C (3.07 nm)	[1.833 1.833 1.764]	223

Phase memory times of all compounds were measured at $T = 2.5$ K using the standard Hahn echo sequence (section 2.2.3), with a π-pulse of length 280 ns to eliminate hydrogen ESEEM. In all cases, the field position was chosen from the peak of a preliminary EFS, as in chapter 3. The resulting curves were fitted to a stretched exponential (equation 3.1), without any instrumental offset. Table 5.2 contains the resulting parameters for each compound, along with the corresponding errors. We note that phase memory times are in the same region as those presented in chapter 3, indicating that dimerisation has not had a detrimental effect on the preservation of coherence at this temperature. The longest phase memory times: 3.2 μs and 2.4 μs, were achieved for compounds **1Bd** and **1C** respectively. This is to be expected given that the carboxylate bridging ligand of compound **1Bd** has been deuterated, limiting the decoherence effect of the highly magnetic protons and that of compound **1C** has been replaced with the more rigid

adamantane group, which reduces decoherence due to the mobility of hydrogen nuclei. In all cases the stretch parameter was greater than 1, suggesting that coherence times may be limited by nuclear spin diffusion mechanisms.

TABLE 5.2: Phase memory time, T_m and stretch parameter, x for each compound, recorded at $T = 2.5$ K, using a standard Hahn echo sequence and π-pulse length of 280 ns, in order to suppress ESEEM. Bracketed distances give the separation of the Cr_7Ni ring centroids for **1A**, **1Bd**, **1C** and **1D** and the Ni-Ni distances for compounds **2A**, **2B** and **2C**.

Compound	T_m (μs)	σ_{T_m} (μs)	x	σ_x
1A (1.64 nm)	0.801	0.003	1.615	0.007
1Bd (1.64 nm)	3.24	0.02	1.294	0.008
1C (1.64 nm)	2.442	0.011	1.209	0.007
1D (2.50 nm)	0.543	0.008	1.295	0.014
2A (1.89 nm)	0.608	0.012	1.27	0.02
2B (2.71 nm)	0.683	0.004	1.45	0.01
2C (3.07 nm)	0.54	0.02	1.18	0.03

5.4 The DEER Sequence

While the CW spectra allow us to place an upper bound on the strength of the interaction between our two Cr_7Ni rings, it does not allow us to estimate it accurately. For this, we require a more sophisticated method and we turn now to the technique mentioned in section 5.1: double electron-electron resonance, or DEER. As was discussed, this utilises the fact that, if there is a magnetic interaction between two spins, the inversion of one will induce a change in the rate of precession of the other, which the DEER technique allows us to measure.

Figure 5.3 illustrates the two types of ESR pulse sequence that can be used for DEER experiments. In panel (a), we meet the 'three-pulse' variant, in which the 'probe' sequence is shown in red. This sets up a simple Hahn echo at the resonant frequency of one spin on the molecule, say spin A, and we measure its integrated intensity. Both pulses are of the same length but are applied with attenuation adjusted to produce a $\pi/2$- and π-pulse. This approach is taken such that the bandwidth excited by each of the pulses is the same. In green is shown the 'pump' sequence. This consists of a single

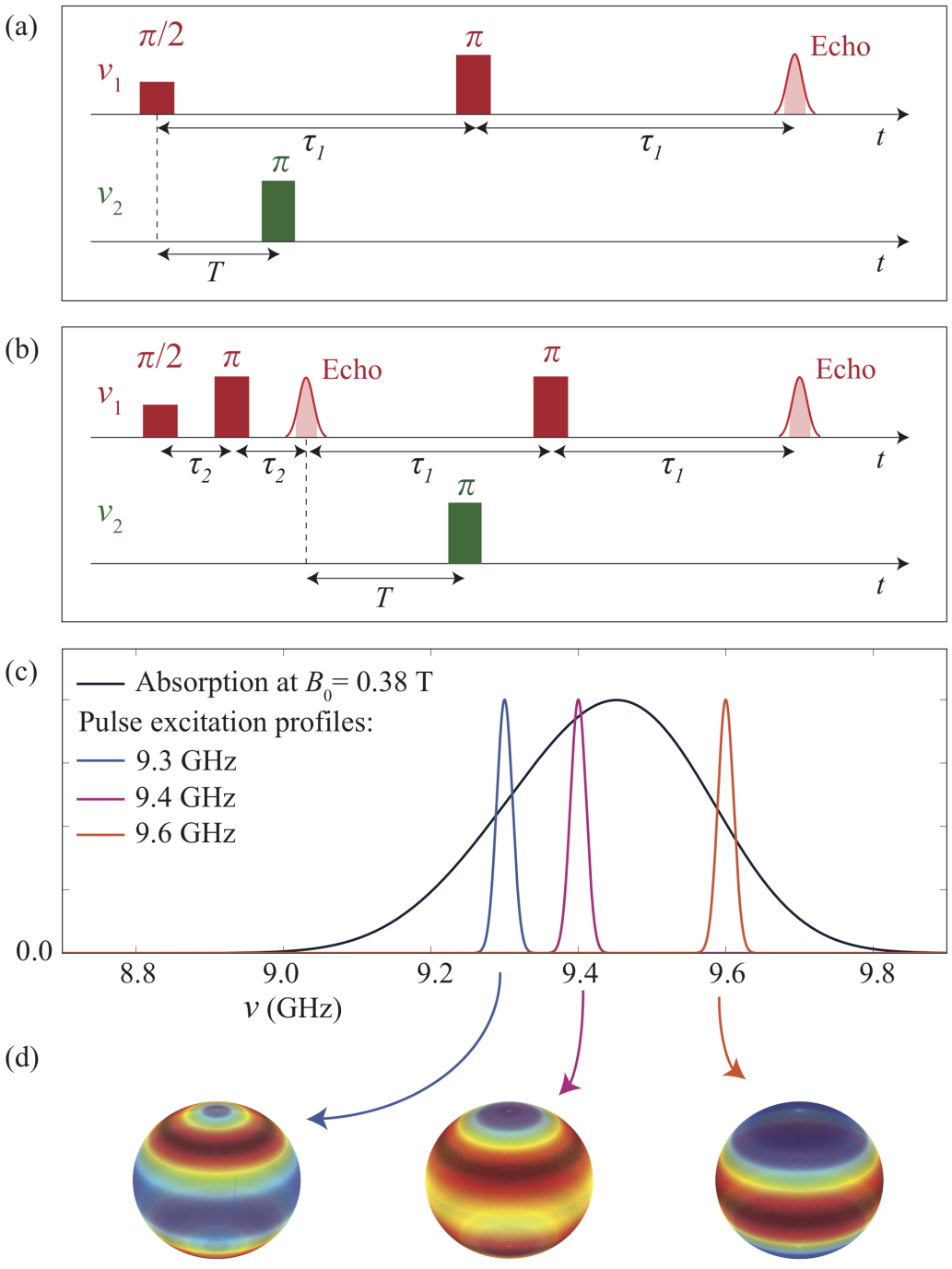

FIGURE 5.3: (a) and (b) illustrate a three and four pulse DEER sequence respectively. In both, the pump pulse (green, at ν_2) is stepped along the time axis, increasing T. The effect of this is seen as an oscillation in the height of the echo, observed with the probe pulse sequence (red, at ν_1). (c) shows the ESR absorption spectrum as a function of frequency, for a system with axial g-tensor ([1.79, 1.79, 1.74]) and 250 MHz isotropic H-strain. Example excitation pulse profiles are shown in blue, pink and orange. (d) provides a visual representation of the ring orientations, relative to a vertical B_0, which, due to g-anisotropy, H-strain and population differences, are excited by each example pulse. The north pole corresponds to rings whose anisotropy axes are aligned with B_0. Red indicates high excitation and blue, low.

π-pulse tuned to the resonant frequency of the other spin in our molecule, say spin B, which is inverted, thereby altering the precession frequency of spin A. The effect of this is to adjust the phase of the echo by an amount dependent upon the time, T, at which the pump pulse was applied. In a DEER experiment, T is incremented, resulting in an oscillation in the integrated echo intensity. A higher frequency of oscillation indicates a greater change in precessional frequency caused by a stronger magnetic interaction between the two spins.

If, when we excite A spins with the probe sequence, the pump pulse excites all B spins in the corresponding molecules, and all magnetic interactions are intramolecular, our observed signal will be as described above. However, this is unfortunately not the case. Firstly, only a fraction of B spins corresponding to the excited A spins, F_{B}, will fall within the bandwidth of the pump pulse. This introduces an unmodulated component. Furthermore, the A spins interact not only with B spins in the same molecules but also with those in neighbouring molecules. This results in a decay of the signal, as at greater T, there is a greater mismatch in background interactions before and after the probe channel π-pulse, thus refocussing is less effective. For a 3D homogenous background distribution of B spins in the point dipole approximation, this is found to be a simple exponential decay:

$$\mathrm{Signal}(T) \propto \exp\left(-k g_{\mathrm{A}} g_{\mathrm{B}} C F_{\mathrm{B}} T\right), \tag{5.1}$$

where k is a constant, g_{A} and g_{B} are the isotropic g factors of spins A and B respectively, and C is the volume concentration of spins [92]. The effect of this is that the strongest signal is seen at the earliest times. However, when the pump pulse overlaps with the $\pi/2$-pulse of the probe sequence, the signal is distorted due to nonlinearities in the high power amplifier. This means that in the 3-pulse sequence we experience a certain amount of 'deadtime', in the most crucial region of the data, when the pulses overlap.

A solution to this problem is provided by the deadtime free '4-pulse' variant of the DEER experiment, shown in panel (b). Now, in the probe channel, the $\pi/2$ pulse is replaced by a Hahn echo sequence, which sets up an echo at time $2\tau_2$ after the initial $\pi/2$-pulse.

At the time the echo is formed, coherence is refocused and, instead of the $\pi/2$-pulse, we can use this as our $T = 0$ point. This allows us to measure the $T = 0$ region without any distortion of the signal. The disadvantage of the sequence is that it is longer, such that the final echo is weaker, which is a problem for samples with short phase memory times.

Now, we have so far based our discussion on the assumption that spins A and B have well-defined frequencies, to which we tune ν_1 and ν_2. However, as was discussed in section 5.1, this is not the case for our Cr_7Ni-Cr_7Ni dimers. Instead, what we have is a distribution of randomly oriented dimers comprising two rings with uniaxial g-tensors. Panel (c) shows the corresponding distribution of resonant frequencies for **1A**, whose g-tensor has principal components [1.791 1.791 1.739] and H-strain = 253 MHz. At a given B_0, a higher g-value corresponds to a higher resonant frequency, therefore higher frequency pulses excite rings oriented such that the largest component of B_0 lies in the plane of the ring (we will refer to these as equatorial rings). Conversely, lower frequency pulses excite rings oriented such that the largest component of B_0 lies parallel to the ring's anisotropy axis (we will call these axial rings). Panel (d) illustrates the orientations selected by the three example pulses shown in panel (c).

In a dimer, we assume that, while not identical due to flexibility of the linker, the orientations of the two rings are reasonably well correlated. Therefore, we choose our frequencies ν_1 and ν_2 to be closely spaced ($\nu_1 - \nu_2 = 80$ MHz) with respect to the total width of the spectrum, aiming to increase the probability of 'pumping' spin B once the probe spin, A, has been chosen. In order to probe different orientational regions, we tuned ν_1 and ν_2 and adjusted B_0 for each experiment. This is because the microwave resonator is non-linear over the frequency range of the absorption spectrum for a given B_0. Three B_0 positions were investigated for each compound. Probe and pump pulse lengths of 40 ns and 20 ns respectively were used in all experiments. Compounds **1A**, **1Bd**, **1C** and **2A** were measured using 4-pulse DEER. Compound **2C** was measured using 3-pulse DEER only. In both cases, a two-step phase cycle was employed, varying the phase of the initial $\pi/2$-pulse. Due to the shorter T_m times of compounds **1D** and **2B**, they were measured using both 3-pulse and 4-pulse DEER. In these cases, the 4-pulse

DEER trace was recorded with a very short acquisition window in order to reconstruct the $T = 0$ region, without reducing the echo height too much. The two traces were then 'stitched' together by the method proposed by Lovett et al. [148].

All data were analysed using the DeerAnalysis package, designed by Jeschke et al. [149]. Using this package, the data were smoothed, corrected for the homogeneous background dipolar interactions and filtered to remove proton ESEEM. Figure 5.4 shows the raw DEER trace for compound **1A** in the lowest field position, with the background fit. From this we see that the background correction is small, as was the case for all compounds. This is a result of the dilution of the the sample. The more rapid decay in the oscillation is due to inhomogeneity in the interaction strength between the two excited spins. All subsequent data are presented post-smoothing and post-background correction. Data are, for comparison, presented both with and without filtering of the H-ESEEM.

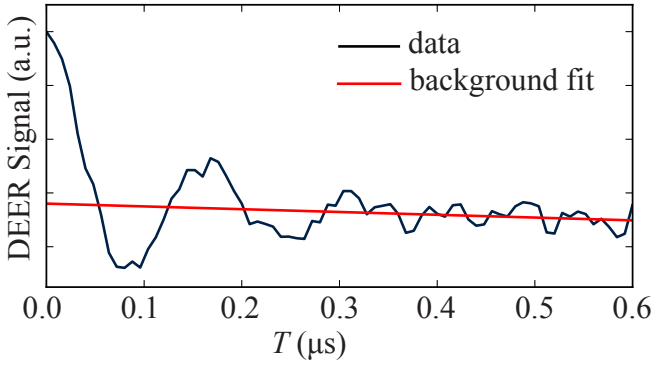

FIGURE 5.4: Smoothed DEER data (dark blue line) for the compound **1A**, recorded with $B_0 = 377.8$ mT, a probe frequency, $\nu_1 = 9.5632$ GHz and a pump frequency, $\nu_2 = 9.4832$ GHz. The ν_1 pulse was of length 40 ns (with power tuned to give either a $\pi/2$- or π- pulse) and the pump pulse was of length 24 ns. The red line shows the background fit which accounts for an exponential decay as a result of a homogeneous background distribution of dipolar couplings.

5.5 DEER Results and Interpretation

Figure 5.5 shows the resulting data for compound **1A**. The left hand panel plots the integrated intensity of the final echo as a function of the time T, at which the pump pulse is applied. Data are plotted both before (open circles) and after (line) a frequency filter is applied to remove proton ESEEM. The right hand panel plots the Fourier transform of

these data. In the upper two traces, the peak corresponding to proton ESEEM is clearly visible at $\nu \approx 17$ MHz in the unfiltered, Fourier transformed data. The central spherical intensity maps indicate the range of orientations excited by a pulse of frequency ν_1, at each B_0.

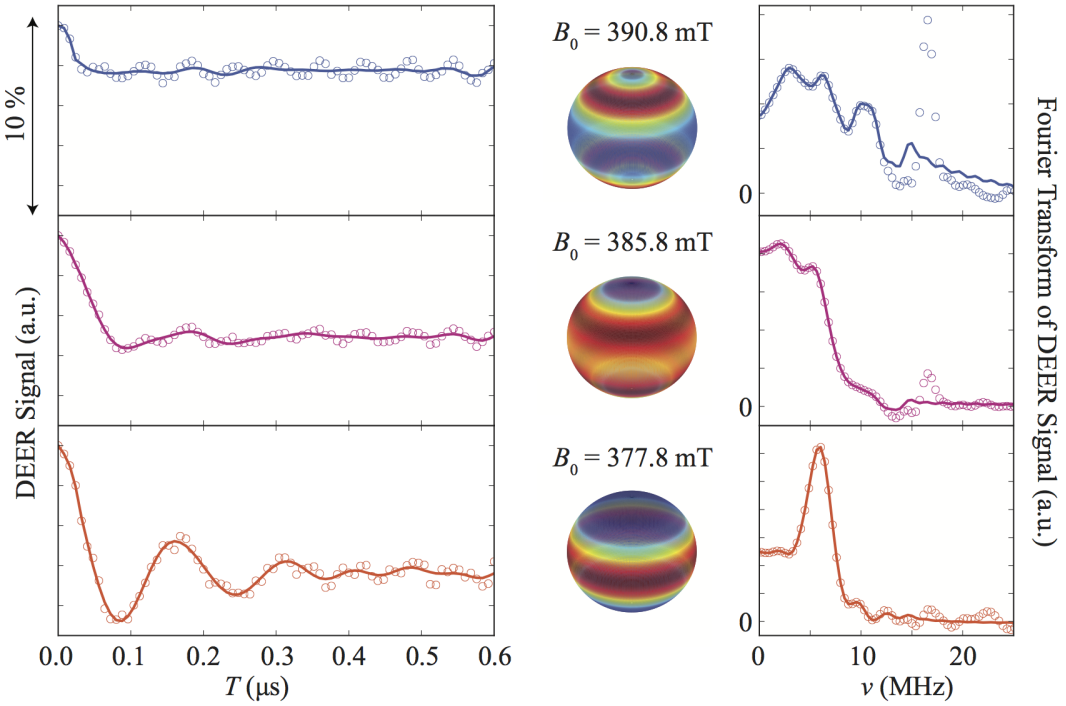

FIGURE 5.5: DEER data for the compound **1A**, in all cases recorded with a probe frequency, $\nu_1 = 9.5632$ GHz and pump frequency, $\nu_2 = 9.4832$ GHz, such that the separation of the two was 0.08 GHz. All ν_1 pulses were of length 40 ns (with power tuned to give either a $\pi/2$- or π- pulse) and the pump pulse was of length 24 ns. Data was recorded in three field positions: $B_0 = 390.8$ mT (blue), $B_0 = 385.8$ mT (pink) and $B_0 = 377.8$ mT (orange), to examine different orientational populations, illustrated by the intensity map spheres, which show intensity excited by a pulse of frequency ν_1. Circles show data after smoothing and correcting for a homogenous background interaction, inducing an exponential decay in the signal. Lines show data after the additional application of a filter to remove the unwanted contribution of proton ESEEM at $\nu = 17$ MHz. Time traces are shown on the left hand side with the Fourier transformed data on the right.

We see that there is a clear dependence of the DEER signal on applied B_0, or rather the selected orientation subpopulation. This is due to a number of factors. Firstly, the strength of the coupling between spins A and B in a given molecule is dependent upon the orientation, θ of the axis joining them with respect to B_0. This varies as $(3\cos^2\theta - 1)$, therefore we expect the frequency of signal oscillation in the DEER trace to be dependent upon B_0, with no oscillation at all close to the 'magic angle': $\theta \approx 54°$ [92]. Secondly, the

number of A spins excited by the probe sequence is proportional to the concentration of spins in that orientational region. The population of rings with anisotropy axis at angle θ to B_0 varies as $\sin\theta$, therefore we expect a stronger signal and lower signal to noise when we probe at a lower B_0, such that we excite more equatorial rings. A further contribution results from variation in the fraction of B spins, F_{B}, excited for a chosen subpopulation of A spins. The higher this fraction, the greater the modulation depth of the oscillation in our DEER trace.

At $B_0 = 377.8$ mT, we see a clearly observable oscillation of approximate period 1.6 μs in the time domain signal, corresponding to a well-defined peak in the Fourier transform, at $\nu \approx 6.2$ MHz. At this field, as shown by the intensity map, we excite mainly equatorial rings, such that we have maximal signal to noise. We also maximise the modulation depth. This is because we choose equatorial A spins, such that any deviation from the equatorial orientation reduces the resonant frequency of the corresponding B spin. Therefore, by pumping with a lower frequency, we capture B spins with orientational deviation from that of the A spin in any direction. This helps to optimise F_{B}, thereby enhancing the modulation depth. We note that the first minimum in the oscillation occurs at a time $T \approx 0.08$ μs. This is the time required for the phase of the A spin to be adjusted by π under the influence of the inverted spin B. It corresponds to the time required for implementation of a two qubit gate and lies perfectly between the compound's $T_{\mathrm{m}} = 0.8$ μs and the single qubit manipulation time of 10 ns.

At $B_0 = 385.8$ mT, we excite a broad distribution of rings joined by an axis at an intermediate angle between directions parallel and perpendicular to the applied B_0. Therefore, the corresponding distribution of interaction strengths is broad and a large proportion of the dimers excited are oriented close to the magic angle, such that they do not show oscillation in the time trace. This results in the absence of a well defined peak in the Fourier transformed data.

The data recorded at $B_0 = 390.8$ mT do not show well defined oscillation. This is for reasons converse to those that gave us such a strong oscillation at $B_0 = 377.8$ mT. At $B_0 = 390.8$ mT, we excite rings that are close to axial, such that firstly, the absolute population excited is small and signal to noise is poor. Secondly, in order for the pump

pulse, at lower frequency than the probe, to excite the B spins corresponding to the chosen A spins, we require them to have a lower g-value, or rather to be 'more axial' than the A spins. This is unlikely, given that the probe is already approaching the edge of the spectrum, therefore F_B is very low, and we do not observe an oscillation.

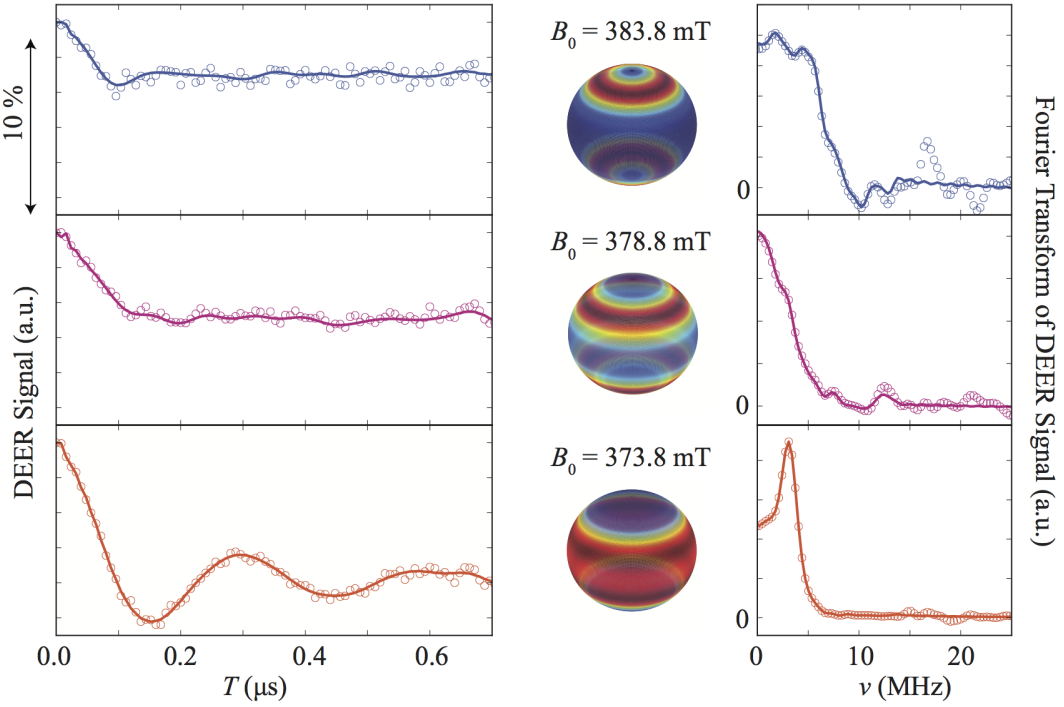

FIGURE 5.6: DEER data for the compound **2A**, in all cases recorded with a probe frequency, ν_1 = 9.5260 GHz and pump frequency, ν_2 = 9.4460 GHz, such that the separation of the two was again 0.08 GHz. All experimental details are as given for figure 5.5 and all plots are analogous.

Figure 5.6 shows the corresponding data for compound **2A**. We see that the same trends as for compound **1A** are followed as we move from the data recorded at the lowest B_0 to that recorded at the highest B_0. The trace at B_0 = 373.8 mT, probing the most equatorial rings, shows a well defined oscillation of approximate time period 0.31 μs corresponding to a sharp peak in the Fourier transform at $\nu \approx 3.2$ MHz. We note that this frequency is approximately half that observed for compound **1A**, indicating an approximately two times weaker magnetic interaction strength. This can be attributed largely to the greater ring-ring separation in compound **2A**; **2A** has a Ni-Ni separation of 1.89 nm compared to the ring centroid separation of 1.64 nm in compound **1A** and in the point dipole approximation, the dipolar interaction strength varies as the inverse

cube of spin separation (equation 4.2). As was the case for compound **1A**, the two qubit gate time, 0.16 μs, lies between the compound's $T_m = 0.61$ μs and that taken to perform a single qubit manipulation. However, in this case, T_m is approximately 4 times the two qubit gate time, rather than 10, as was the case for **1A**, such that the coherence time would be more limiting in the implementation of quantum algorithms.

The same trends were observed in the data for all other compounds, and the two qubit gate times, as taken from the lower field traces, are presented in table 5.3, along with the measured T_m times and the ratio of T_m to the two qubit gate time, for comparison. We see that compounds in group **1** in general offer longer T_m times and shorter two qubit gate times. In particular, compounds **1Bd** and **1C** offer excellent ratios of 39 and 31 respectively, making them eminently suitable for the implementation of two qubit gates.

TABLE 5.3: Comparison of phase memory time, T_m, as presented in table 5.2 and two-qubit gate time, as determined from the first minimum in the lowest field DEER trace, at $T = 2.5$ K. Bracketed distances give the separation of the Cr_7Ni ring centroids for **1A**, **1Bd**, **1C** and **1D** and the Ni-Ni distances for compounds **2A**, **2B** and **2C**.

Compound	T_m (μs)	Two qubit gate (μs)	T_m/Two qubit gate
1A (1.64 nm)	0.801	0.080	10.0
1Bd (1.64 nm)	3.24	0.084	38.6
1C (1.64 nm)	2.442	0.080	30.5
1D (2.50 nm)	0.543	0.232	2.3
2A (1.89 nm)	0.608	0.157	3.8
2B (2.71 nm)	0.683	0.400	1.7
2C (3.07 nm)	0.54	0.550	1.0

5.6 Outlook

Now that we have identified compounds which obey the hierarchy of timescales required for the implementation of two qubit gates, we ask how one could proceed towards the implementation itself, specifically the entanglement of the two spins' states. Firstly, a significant advantage could be gained by moving to work at Q- rather than X-band. If we were to move from working at $T = 2.5$ K at X-band to $T = 2.5$ K at Q-band, we would enhance the initial population excess in the lower energy state for a given spin from ~ 8.5 % to ~ 29.4 %. This would enhance both the signal strength and the purity of any

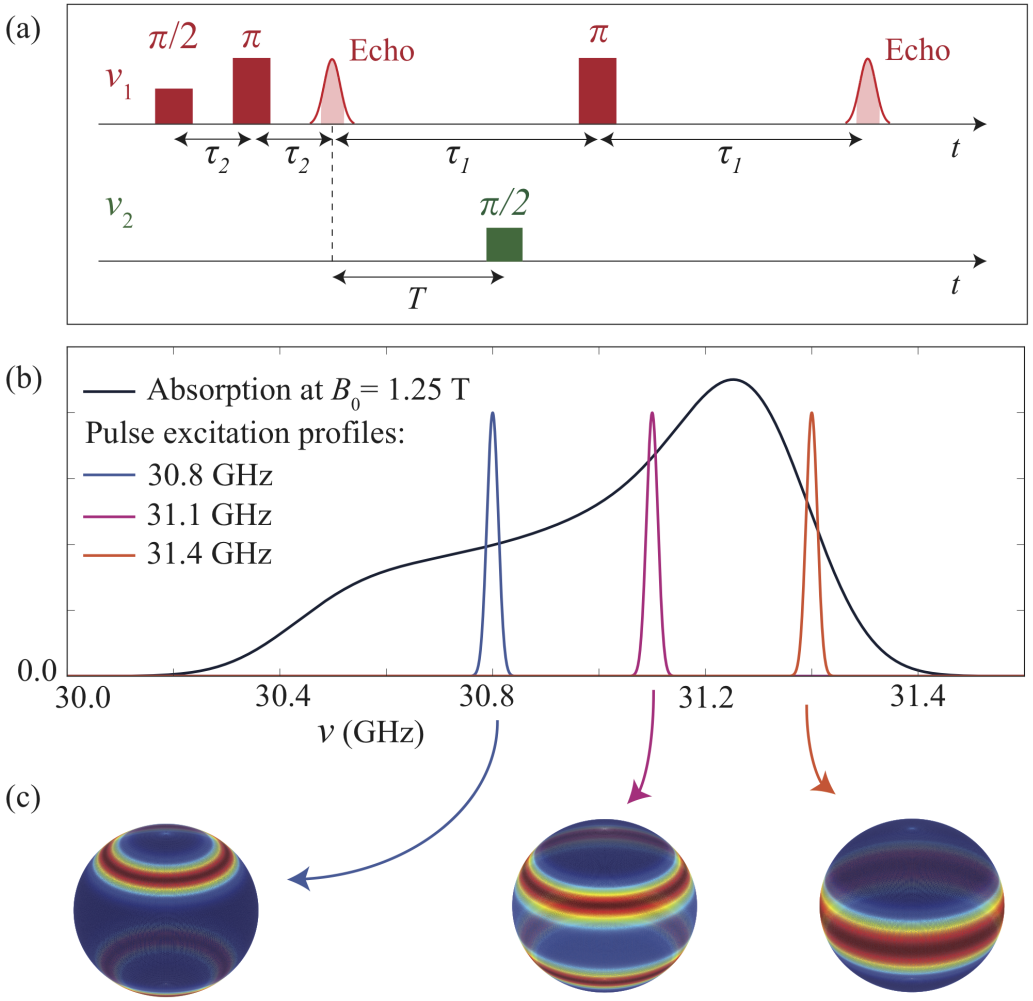

FIGURE 5.7: (a) illustrates the adapted four pulse DEER sequence proposed for use in the formation of an entangled state. The ν_2 pulse (green) is stepped along the time axis, increasing T, to modify the phase difference of the spin A states coupled to the up and down components of spin B. (b) shows the Q-band ESR absorption spectrum as a function of frequency, for a system with axial g-tensor ([1.79, 1.79, 1.74]) and 250 MHz isotropic. Example excitation pulse profiles are shown in blue, pink and orange. (d) provides a visual representation of the ring orientations, relative to a vertical B_0, which, due to g-anisotropy, H-strain and population differences, are excited by each example pulse. The north pole corresponds to rings whose anisotropy axes are aligned with B_0. Red indicates high excitation and blue, low.

resulting state formed [36, 38]. Working at Q-band would also provide a greater degree of orientational selectivity. Figure 5.7(b) shows the distribution of resonant frequencies for **1A**, whose g-tensor has principal components [1.791 1.791 1.739] and H-strain = 253 MHz. We see a greater degree of structure compared with the X-band spectrum shown in figure 5.3 and the corresponding spherical intensity maps for the pulses marked (panel (c)) illustrate the narrower range of orientations excited by a given pulse at Q-band. This would result in a narrower range of interaction strengths between the selected spins, slowing the decay of the observed oscillations.

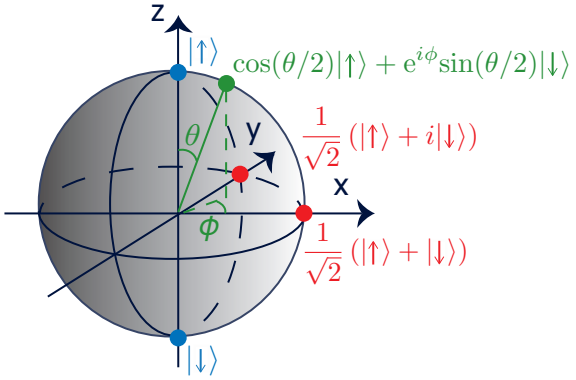

FIGURE 5.8: Visualisation of a two level system of states $|\uparrow\rangle$ and $|\downarrow\rangle$ on the Bloch sphere.

We turn now to consider the pulse sequence itself, shown by figure 5.7(a). This is very similar to the 4-pulse DEER sequence in figure 5.3, with the only difference that the 'pump' pulse, previously a π-pulse, is now replaced by a $\pi/2$-pulse. The effect of this can be considered as follows, if we assume an initial state in which both spin A (red channel, resonant frequency ν_1) and spin B (green channel, resonant frequency ν_2) are in the lower energy spin 'up' state, so aligned with B_0, then

$$|\psi\rangle = |\uparrow\rangle_A|\uparrow\rangle_B. \tag{5.2}$$

Application of a $\pi/2$-pulse in the y-direction (as defined by figure 5.8) then 'tips' spin A into a superposition state:

$$|\psi\rangle = \frac{1}{\sqrt{2}}(|\uparrow\rangle + |\downarrow\rangle)_A|\uparrow\rangle_B. \tag{5.3}$$

After the application of one π-pulse in the y-direction, which acts to invert the phase, we have

$$|\psi\rangle = \frac{1}{\sqrt{2}}(|\uparrow\rangle - |\downarrow\rangle)_A|\uparrow\rangle_B, \tag{5.4}$$

and after the second π-pulse, we return to the state described by equation 5.3. However, if we apply the additional $\pi/2$-pulse at ν_2, this is no longer the case. This acts to place spin B in a superposition state such that, at the time of application, we have:

$$|\psi\rangle = \frac{1}{2}(|\uparrow\rangle - |\downarrow\rangle)_A(|\uparrow\rangle + |\downarrow\rangle)_B. \tag{5.5}$$

This can alternatively be written as

$$|\psi\rangle = \frac{1}{2}(|\uparrow\rangle - |\downarrow\rangle)_A|\uparrow\rangle_B + \frac{1}{2}(|\uparrow\rangle - |\downarrow\rangle)_A|\downarrow\rangle_B. \tag{5.6}$$

Now, as was discussed in the context of the DEER experiment, the state of spin B controls the rate of precession of spin A. Therefore the A states in equation 5.6 will accumulate a phase difference, dependent upon the time for which their corresponding B spins are in different states. This will correspond to the phase accumulated over time T, given that this is the time for which precession rates are asymmetric about the time at which the ν_1 π-pulse refocussing pulse is applied. If T is chosen such that the phase difference accumulated in this time is π, the resulting final state is

$$|\psi\rangle = \frac{1}{2}(|\uparrow\rangle + |\downarrow\rangle)_A|\uparrow\rangle_B + \frac{1}{2}(|\uparrow\rangle - |\downarrow\rangle)_A|\downarrow\rangle_B. \tag{5.7}$$

Now, we have adjusted the state of qubit A dependent upon the state of qubit B, such that the final state given by equation 5.7 is inseparable. We have formed an entangled state. Application of a further ν_1 $\pi/2$-pulse in the y-direction would then convert this into one of the famous Bell states,

$$|\psi\rangle = \frac{1}{\sqrt{2}}(|\downarrow\rangle_A|\uparrow\rangle_B + |\uparrow\rangle_A|\downarrow\rangle_B). \tag{5.8}$$

such that we had conditionally inverted the state of spin A dependent upon the state of spin B. This is known as a CNOT gate [1].

5.7 Conclusions

In conclusion, we have explored two groups of Cr_7Ni-Cr_7Ni ring dimers: those threaded on rigid axles ('rotaxanes') and those linked chemically. To be useful in the implementation of a two qubit gate, we require a dimer to have a long phase memory time, a short single qubit manipulation time and an intermediate two qubit gate time, governed by the strength of the magnetic interaction between the two spins. The phase memory times of all dimers were measured in a Hahn echo experiment and the two qubit gate times were estimated using the two frequency ESR technique, double electron-electron resonance. It was found that, at $T = 2.5$ K, the rotaxanes in particular showed times which obeyed this hierarchy of timescales, with phase memory times up to ~ 39 times longer than the two qubit gate time and two qubit gate times ~ 8 times the single qubit manipulation time. It was found that the effects of the magnetic interaction between the spins were most clearly observable when probing rings in an equatorial orientation.

The last part of this chapter discussed how the work might be advanced. Suggestions have been made: firstly, to work at higher field and frequency, in order to enhance both state purity and the degree of orientational selectivity that we have; secondly, an 'adapted DEER' pulse sequence, which would enable entanglement of the two spins in a dimer and the implementation of a CNOT gate, was proposed.

Chapter 6

The Issue of Alignment: $Cr_7Zn@Ga_7Zn$ and Mn:ZnO

6.1 Introduction

When, in 2001, Loss et al. presented a scheme utilising the ESR of MNMs to perform Grover's algorithm with an efficiency greater than that permitted classically, the field of MNMs for QIP was born [47]. The proposal utilises the high spin and large negative anisotropy of MNMs, with a unit of memory consisting of a single MNM rather than multiple two level systems. A high static magnetic field is applied and subsequently reduced, in order to initialise a majority population in the lowest energy levels. This is followed by application of a microwave pulse of discrete frequency spectrum, tuned to the allowed transitions of the MNM, which forms simultaneous coherences between the lowest and each upper energy level thereby allowing simultaneous queries. Further to this, although not specifically referencing MNMs, there has been a number of studies, both experimental and theoretical, which exploit computational units of greater than two energy levels [150–156]. These have presented situations in which use of a higher dimensional Hilbert space can both enhance security and reduce the required number of quantum gates. The aim of this chapter is to explore the use of MNMs of ground state spin, $S > 1/2$ as units for QIP, within the experimental constraints of our pulsed ESR system.

Work in previous chapters has focused entirely on Cr_7M rings of spin $S = 1/2$, for which, regardless of orientation, there is only one transition excitable using ESR: $m_S = -1/2 : m_S = 1/2$. It has therefore been possible to measure these in frozen solution, with rings of every orientation, diluted such that ring-to-ring dipolar interactions are negligible. As we move to spins $S > 1/2$, this is no longer possible, with anisotropic terms in the Hamiltonian introducing a dependence of accessible transitions upon the ring's orientation with respect to B_0. In order to exploit these compounds, we must, with a given pulse, be able to excite the same transition on every ring. We therefore require an oriented ensemble. The obvious way to obtain this is to measure the rings as a single crystal, however, we would then lose the advantage of dilution and the decoherence induced by inter-ring dipolar interactions would be crippling. Previous attempts to overcome this issue have applied a strong static magnetic field in order to quench electron spin flip-flop relaxation [157, 158]. The work in the first half of this chapter takes an alternative approach, with measurements performed on a single crystal in which the $S = 3/2$ rings Cr_7Zn dope the isostructural, diamagnetic host Ga_7Zn. These comprise the first ever coherent manipulations of such a dilute oriented ensemble of MNMs.

Once we have our dilute oriented ensemble of rings, we want to manipulate our spins within the resulting ladder of states. In order to explore this in the first instance, we take a test system, the Mn defect in ZnO, which forms a fully oriented dilute ensemble, with the large electron spin, $S = 5/2$ coupled to a large nuclear spin, $I = 5/2$. The spin shows a negative anisotropy, lifting transition degeneracies, and a rich landscape of transitions excitable with ESR. Furthermore, Mn:ZnO shows long electron coherence times, reaching $T_2 \sim 50$ μs at $T = 50$ K, making it an ideal candidate for pulse sequence development [42]. The work presented in the second half of this chapter aims to identify a suitable three level system within the level structure of Mn:ZnO, manipulating spins across all three levels. It is hoped that this will in future, be transferrable to MNM based systems.

The chapter begins by introducing details of the $Cr_7Zn@Ga_7Zn$ crystal, moving on to present nutation data. This is based on work already published [159]. We then turn to

the Mn:ZnO system, discussing first the structure of its energy levels and the identification of its transitions. Finally, a new pulse sequence and resulting data are presented for a subset of three levels, with manipulations performed across all three. We explore a way to initialise the system, alternative to that presented in the original paper of Loss et al., via formation of a pseudopure state. $Cr_7Zn@Ga_7Zn$ was synthesised by Dr Grigore Timco at the University of Manchester. Alignment and initial CW and relaxation measurements were performed by Dr Fabrizio Moro at the University of Manchester. Sample simulation, nutation experiments and subsequent analysis are my own. All simulation, measurement and analysis presented on Mn:ZnO are entirely my own. The sample was purchased from MTI Corporation and cut to the appropriate size by Bob Watkins.

6.2 Cr_7Zn doped Ga_7Zn

6.2.1 Sample

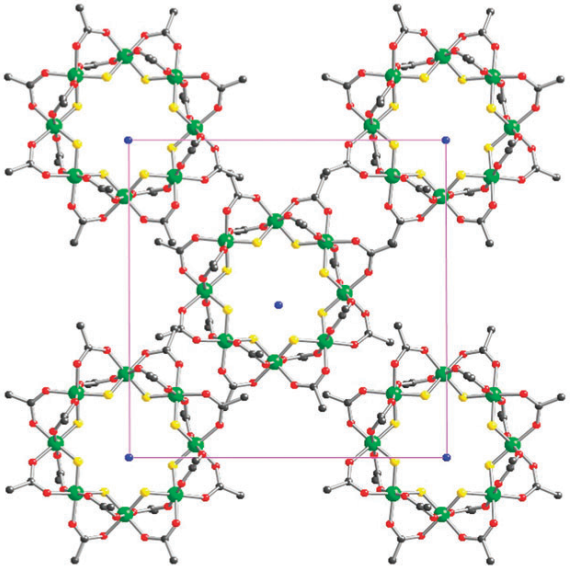

FIGURE 6.1: Unit cell of $Cr_7Zn@Ga_7Zn$ viewed down the crystal c axis. The coloured balls represent Ga/Cr/Zn (green), F (yellow), O (red), N (blue), C (black). Methyl groups are omitted for clarity.

$Cr_7Zn@Ga_7Zn$ crystallises in the tetragonal I4 space group, with the molecules lying on the C4 axis such that all rings lie in the crystal ab plane. Figure 6.1 shows the unit cell, viewed down the crystal c axis. The metal ions in each ring form a planar octagon

and, as in previous chapters, each is bridged to its neighbour by a fluoride and two pivalate ligands. The resulting negative charge on the ring is neutralised by templating around a $Me_2NH_2^+$ cation. The crystal comprises 0.3% Cr_7Zn by mass, doped into the isostructural and diamagnetic host, Ga_7Zn. CW measurements confirmed that there was no scrambling of Cr^{3+} and Ga^{3+}. Antiferromagnetic exchange between magnetic ions in the ring and the zero spin of the Zn^{2+} ion, give Cr_7Zn a ground state spin of $S = 3/2$. This is, in the GSA, described by the Hamiltonian

$$H = DS_z^2 + E(S_x^2 - S_y^2) + \mu_B \boldsymbol{B}_0 \cdot \boldsymbol{g} \cdot \boldsymbol{S}, \tag{6.1}$$

where $D = -12.6$ GHz, $E = 1.46$ GHz, $g = 1.96$. The principal direction of the ZFS tensor is normal to the Cr_7Zn plane.

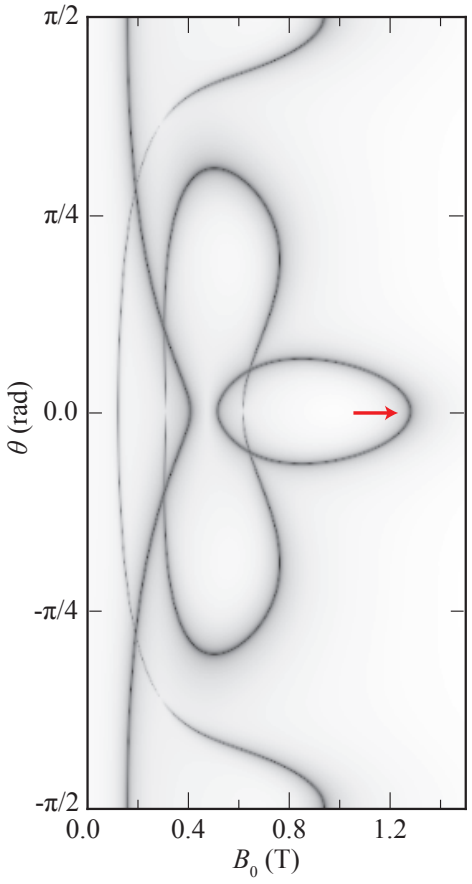

FIGURE 6.2: ESR transition intensity for Cr_7Zn (as described by equation 6.1) as a function of B_0 and its angle, θ to the anisotropy axis of the crystal. Calculated for microwave frequency $\nu = 9.5$ GHz. Darker shades indicate a greater intensity. The red arrow points to the position in which nutation experiments were performed.

Crystals were mounted to allow ESR measurement in the crystal bc plane. The b and c axes (defined here as $\theta = 90°$ and $\theta = 0°$, respectively) can then be identified from turning points in the allowed ESR resonances, mapped as a function of θ and B_0 (figure 6.2). The coplanarity of the rings in the unit cell means there is only one magnetically distinct molecule when B_0 is parallel to c (also the molecular z direction). However, because the Zn ion is disordered over all sites of the Cr_7Zn octagon, when B_0 is applied at finite angle, θ to c, this is no longer the case. By symmetry, if ψ is the projection of B_0 onto the molecular xy plane, there are distinct magnetic orientations corresponding to ψ, $\psi + 45°$, $\psi + 90°$ and $\psi + 135°$. Therefore, at finite θ, we should observe four sets of resonances from distinct molecules in the bc plane, which collapse onto a single set at $\theta = 0°$. The effect of these distinct orientations is illustrated by figure 6.3, which shows the simulated energy level structure for $\theta = 8°$ and $\theta = 90°$, with $\psi = 16°$.

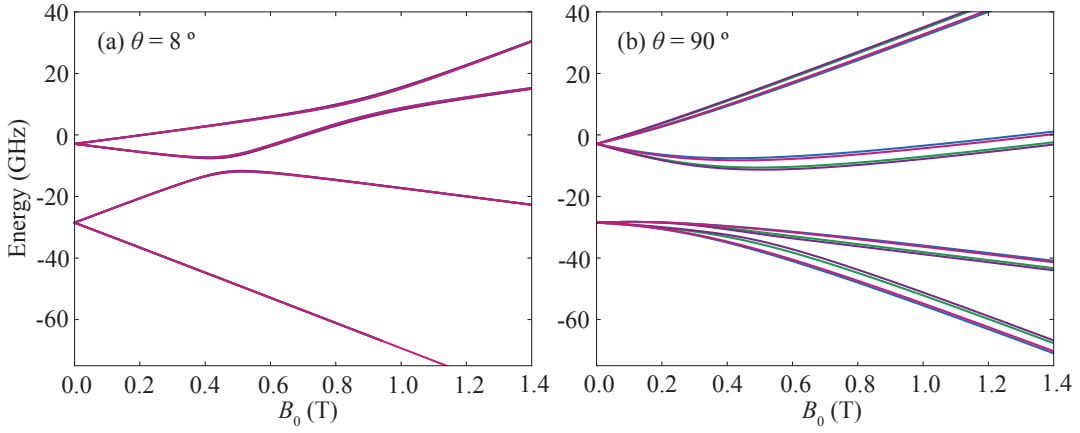

FIGURE 6.3: Simulated energy level structures for the $S = 3/2$ ground state of Cr_7Zn, as a function of applied magnetic field, B_0, applied at angles (a) 8° and (b) 90° to the anisotropy axis. Calculated for microwave frequency, $\nu = 9.5$ GHz. Different colours represent the four distinct molecular orientations.

6.2.2 ESR Measurements and Results

Preliminary measurements showed that the crystal was sufficiently dilute that spin echoes were observable below $T \sim 8$ K via the standard Hahn echo sequence (chapter 1), showing phase memory times of up to 1.5 μs at $T = 2.5$ K. Further to this, nutation experiments were carried out on the $Cr_7Zn@Ga_7Zn$ single crystal, in order to prove that coherent spin manipulations are possible. In this experiment, a nutation

pulse of duration t_p tips the magnetisation through an angle $g\mu_B B_1 t_\mathrm{p}/\hbar$, followed by a two-pulse detection sequence (figure 6.4 with a four-step phase cycle). The echo intensity, quantifying the z-component of the magnetisation after the nutation pulse, is measured as a function of t_p. This experiment sets up a coherent oscillation between the two states, corresponding to the generation of arbitrary superpositions, observed as oscillation of the echo intensity as a function of t_p. These are sometimes described as Rabi oscillations, although this is only strictly correct when the pulse bandwidth substantially exceeds the ESR linewidth, such that all spin packets rotate together.

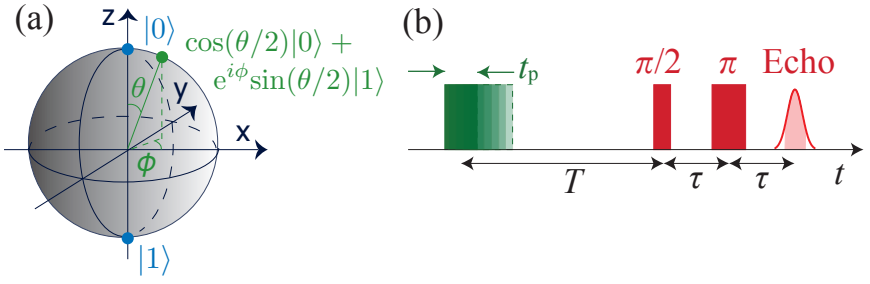

FIGURE 6.4: Pulse sequence used to perform nutation experiments. The first pulse ((b) green) tips the magnetisation by angle θ ((a) green), dependent upon the length of the pulse. The $\pi/2 - \tau - \pi - \tau -$ echo ((b) red) measures the z component of the magnetisation after the nutation pulse.

We selected the highest-field and most isolated transition for $c \parallel B_0$, with $B_0 = 1160$ mT, corresponding to the nominally $m_S = +1/2$ to $+3/2$ transition with frequency 9.77 GHz. We find oscillations in the echo amplitude as a function of t_p (figure 6.5; $T = 256$ ns and the $\pi/2$- and π-pulses are optimised for the power). The oscillation frequency is proportional to the square root of the applied microwave power (i.e. to the amplitude of the microwave field B_1; figure 6.6), demonstrating that we are observing coherent electron spin oscillations rather than other phenomena such as ESEEM. The excitation bandwidth in this experiment is narrow compared to the inhomogeneous broadening of the line, leading to a nutation envelope that depends on oscillation number rather than time.

It has been noted in previous nutation experiments on MNMs in frozen solution that the distribution in molecular orientations being excited (each with a different nutation frequency) contributes to premature damping of the oscillations before the limits placed by T_2 [160–162]. This factor is removed in the present single crystal experiments and

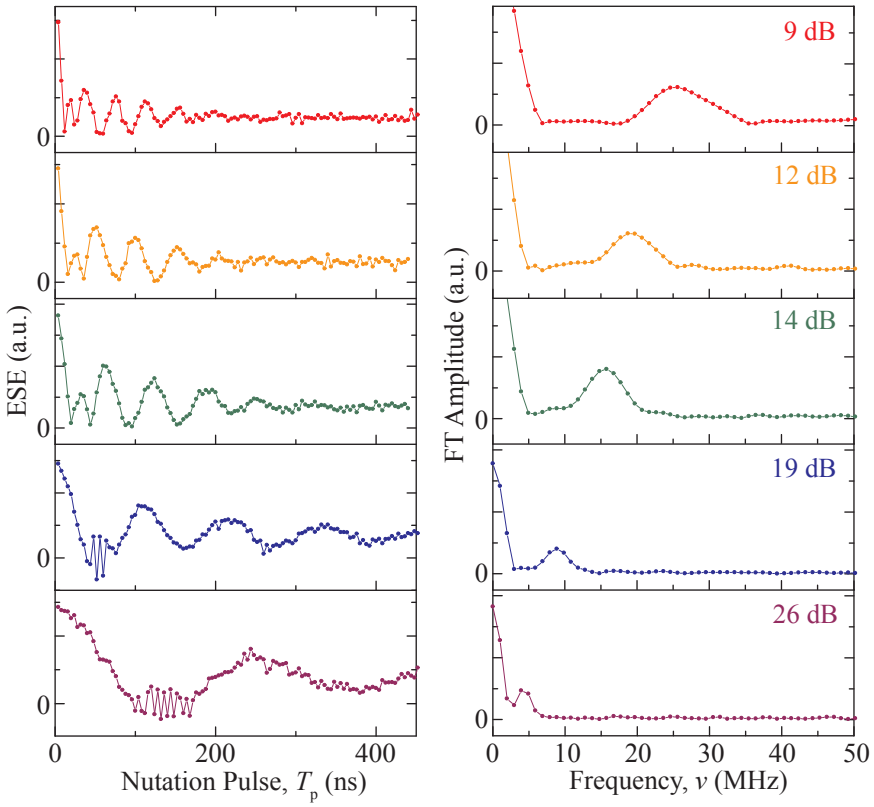

FIGURE 6.5: Left: nutation experiment at $T = 4.5$ K measured at $B_0 = 1160$ mT with $c \parallel B_0$, for a range of attenuation settings (marked). Right: Fourier transforms of the nutations.

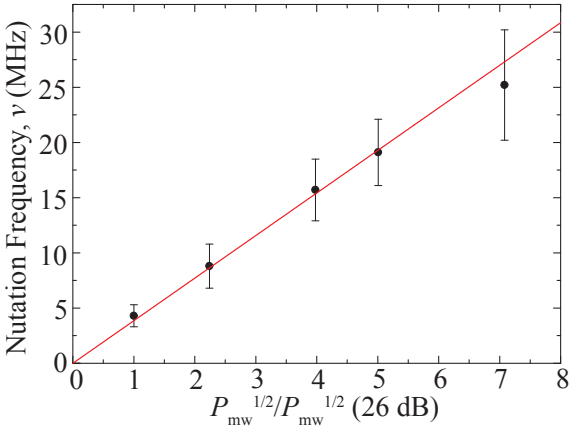

FIGURE 6.6: Nutation frequency as a function of the square root of applied microwave power relative to that when a high power attenuation of 26 dB is applied (black circles; measured at $B_0 = 1160$ mT and $c \parallel B_0$ at $T = 4.5$ K). Error bars are derived from the full width at half maximum of the corresponding peaks in the Fourier transformed data (figure 6.5). The linear least squares fit (red line) was constrained to go through the origin.

limiting factors may instead include D-strain and/or crystal mosaicity, with analogous effects.

6.3 ZnO

6.3.1 Sample

Zn(II)O (referred to as ZnO) is a semiconductor, which can have either a cubic or hexagonal crystal structure [163]. The sample used presently is of the latter type, known as 'wurtzite', with each cation surrounded by four anions at the corners of a tetrahedron. It contains Mn as a naturally occurring impurity, with Mn^{2+} ions replacing non magnetic Zn^{2+} ions at cation sites. Such sites are identical, therefore our Mn^{2+} ions are perfectly aligned, with the molecular z axis coinciding with the crystal c axis. They have an electron spin $S = 5/2$ coupled to a nuclear spin $I = 5/2$ and are described by the spin Hamiltonian

$$H = D\hat{S}_z^2 + \mu_{\mathrm{B}}\boldsymbol{B}_0 \cdot \boldsymbol{g} \cdot \boldsymbol{S} + \mu_{\mathrm{N}}\boldsymbol{B}_0 \cdot \boldsymbol{g}_{\mathrm{N}} \cdot \boldsymbol{I} + \boldsymbol{S} \cdot \boldsymbol{A} \cdot \boldsymbol{I}, \tag{6.2}$$

where $D = -705$ MHz. The principal components of the three tensors are $g_{\|} = 1.998$, $g_{\perp} = 2.000$, $A_{\|} = 222$ MHz, $A_{\perp} = 220$ MHz and $g_{N,\|} = g_{N,\perp} = 7.54\text{x}10^{-4}$, where $\|$ and $\perp$ refer to directions parallel and perpendicular to the molecular z axis, respectively [164]. The third term represents the nuclear Zeeman energy and the final term, the hyperfine coupling. In contrast to the case of the N spin in chapter 4, the hyperfine coupling shows slight anisotropy such that there is a slight energetic preference for the electron and nuclear spins to be antiparallel along the crystal anisotropy axis. Higher order terms, such as nuclear quadrupole and fourth order electron spin anisotropy, have previously been detected however they are small and irrelevant for the work discussed in this chapter therefore are omitted. All data presented here were taken on a sample of dimensions 5.0 x 2.5 x 0.22 mm. The crystal c-axis coincides with the smallest of these. The sample was mounted, using a small quantity of vacuum grease, on the flat surface of a quartz

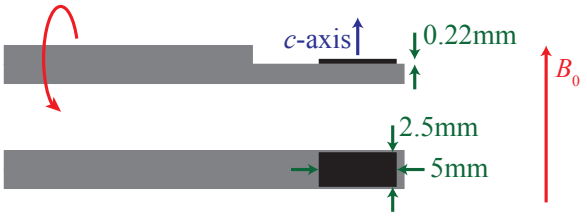

FIGURE 6.7: Schematic showing the ZnO sample (black) mounted onto the flat surface of a quartz rod (grey). Upper: orientation with $B_0 \parallel c$. Lower: B_0 in ac-plane. The curved red arrow marks the direction of rotation of the sample.

rod such that it could be conveniently rotated in the crystal ac plane (figure 6.7). Both of its faces were polished.

The rich landscape of ESR transitions that ZnO provides is illustrated by figure 6.8. Turning points in this structure are used to align the sample within the ac-plane. We note how, as we move away from the principal axes, the transitions move closer to each other in field.

6.3.2 Identifying a Three Level System

In order to explore manipulation over three energy levels, we must first identify a suitable subsystem within the ZnO landscape. As shown by figure 6.9, we require two transitions of frequencies ν_1, ν_2, with one energy level in common. In addition, we must be able to excite both these transitions using ESR. This relies upon both transitions having a non-zero matrix element and both frequencies falling within the bandwidth of our resonator. When overdamped ($Q \sim 150$), the resonator used in this study has a bandwidth $\Delta\nu \sim$ 65 MHz, which, for a $g = 2$ spin, corresponds to $\Delta B_0 \sim 2.3$ mT.

Figure 6.10(a) shows the energy level structure at $\theta = 0°$. We see six main groups of energy levels, corresponding to the different m_s states. These are further split into different m_I states. Allowed ESR transitions, for all of which $\Delta m_I = 0$ at this angle, are marked. In the corresponding EFS (figure 6.10(b)), these are all clearly observable. This means identification of two transitions with one level in common, is simple: we choose any three electron spin states, with m_S changing by one from one to the next, for example, $m_S = 1/2,\ 3/2,\ 5/2$, for a given m_I. The problem is, however, that the resulting ν_1 and ν_2 are too far apart to fit within the bandwidth of the cavity. For

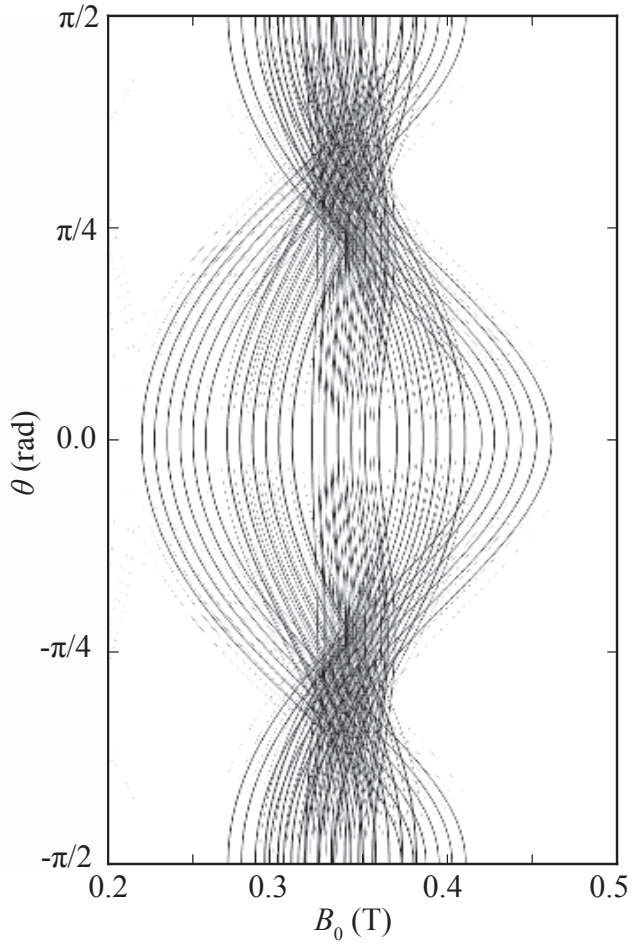

FIGURE 6.8: ESR transition intensity for Mn:ZnO (as described by equation 6.2) as a function of B_0 and its angle, θ to the anisotropy axis of the crystal. Calculated for microwave frequency, $\nu = 9.5$ GHz. Darker shades indicate a greater intensity.

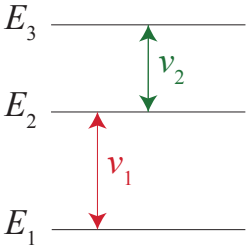

FIGURE 6.9: Three level system, with two transitions of frequencies ν_1, ν_2.

example, if we take $m_I = -5/2$ and $m_S = -5/2, -3/2, -1/2$, for $\nu_1 = 9.722$ GHz, we require $\nu_2 = 11.949$ GHz, such that the required bandwidth, $\Delta\nu_{\text{req}} = 2.227$ GHz is orders of magnitude greater than that we have.

As a potential solution to this problem, we rotate the sample away from $B_0 \parallel c$ in order

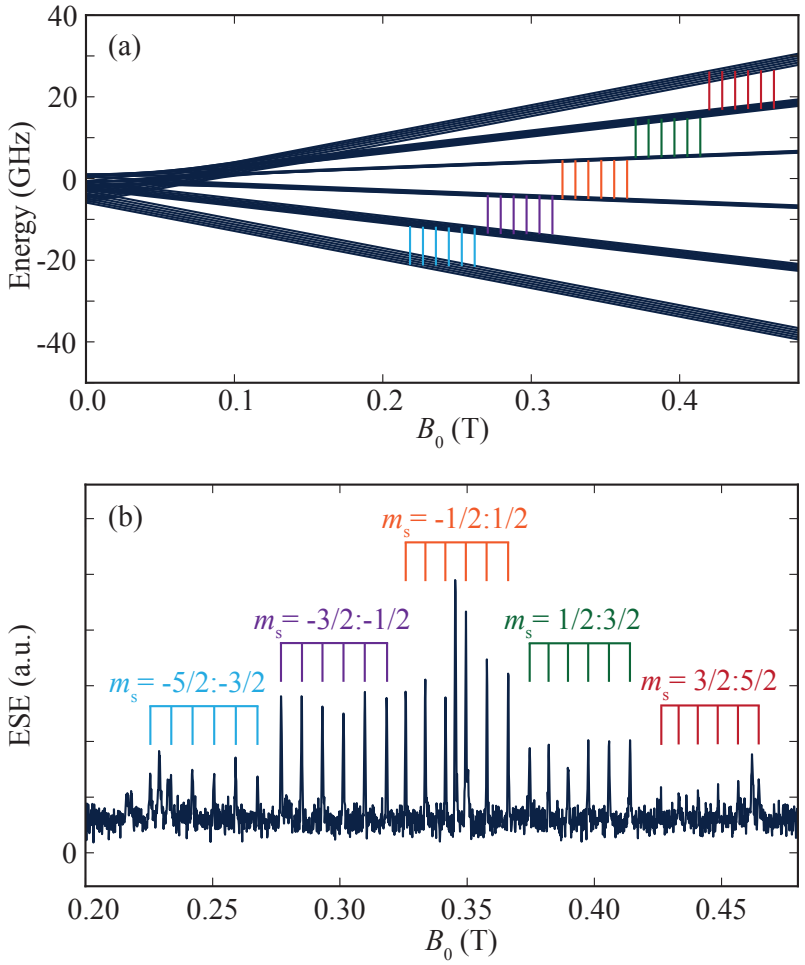

FIGURE 6.10: (a) Simulated energy level structure and (b) EFS, as a function of B_0, parallel to the anisotropy axis, for the $S = 5/2$ electron spin coupled to the $I = 5/2$ nuclear spin of Mn:ZnO. EFS recorded at $T = 50$ K, with $\nu = 9.722$ GHz, and a π-pulse of length 32 ns. Coloured lines mark allowed magnetic dipole transitions.

to exploit the greater proximity of transitions. Figure 6.11 shows the EFS at $\theta = 45°$, recorded using the same experimental parameters as figure 6.10(a). We see that there is a high density of transitions, such that it is impossible, by eye, to pick out for any given one, the changes in m_S and m_I. At this angle, we now see the effects of state mixing, such that m_S is no longer a good quantum number and observe 'forbidden' transitions, for example $\Delta m_S = \pm 2$, $\Delta m_I = \pm 1$. The dense structure means that we are more likely to find three levels which satisfy our constraints, however, finding them is difficult.

The method devised to overcome this problem, we refer to as the 'echo kill' experiment, and it is illustrated by figure 6.12. Rather than attempting to identify and choose two appropriate transitions from the EFS, we choose just one strong transition. We then

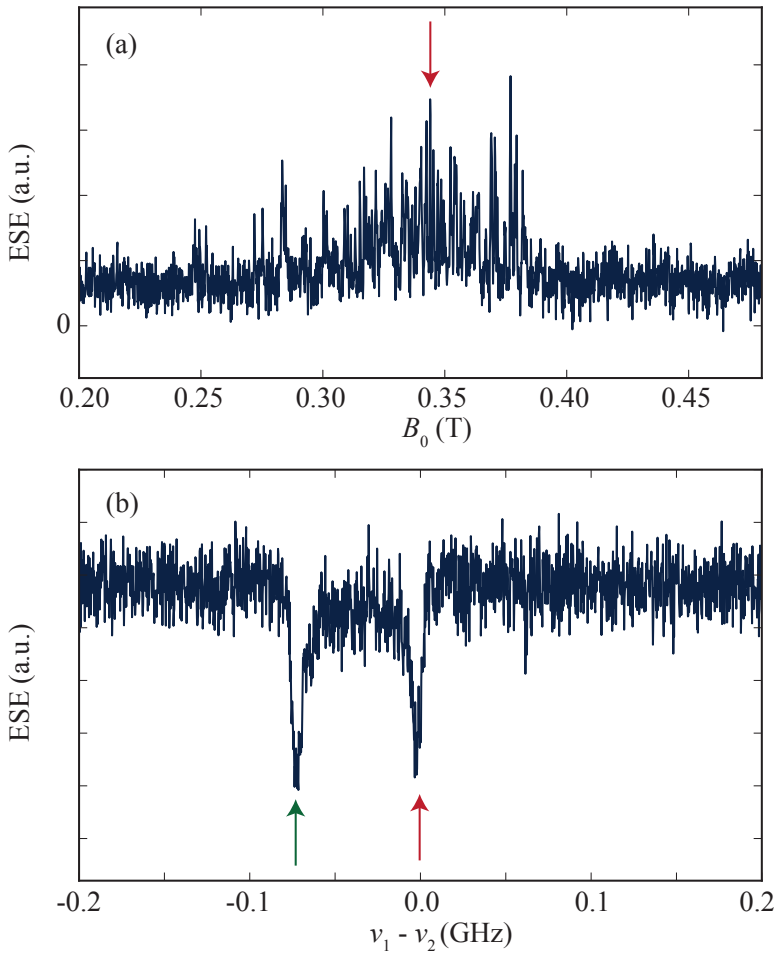

FIGURE 6.11: (a) EFS, as a function of applied magnetic field, B_0, with ν_1 = 9.722 GHz, and a π-pulse length of 32 ns, and (b) Echo Kill experiment (as detailed in figure 6.12, with t_p = 200 ns, and ν_2 varied) as a function of frequency separation ($\nu_1 - \nu_2$), for the $S = 5/2$ electron spin coupled to the $I = 5/2$ nuclear spin of Mn:ZnO. Both spectra were recorded at $T = 50$ K, with B_0 at an angle of $\theta = 45°$ to the anisotropy axis. The red and green arrows mark ν_1 and the ν_2 value chosen for subsequent experiments, respectively.

tune B_0 such that it is excited by microwave frequency ν_1, and set up a tuned Hahn echo on the transition, shown in red. The next step is to apply a second pulse (green) of fixed length, reminiscent of that used in the DEER experiments of chapter 5. However, the experiment here is fundamentally different in that we are aiming to excite an upper transition on the same spin rather than to address a second one. By varying the pulse's frequency, we are now able to test the whole range of available transitions. If we find one that has an energy level in common with the transition at ν_1, we expect that population will be moved from E_2 to E_3. This should be observed as a dip in echo intensity as a function of ν_2, i.e. a 'killing' of the echo.

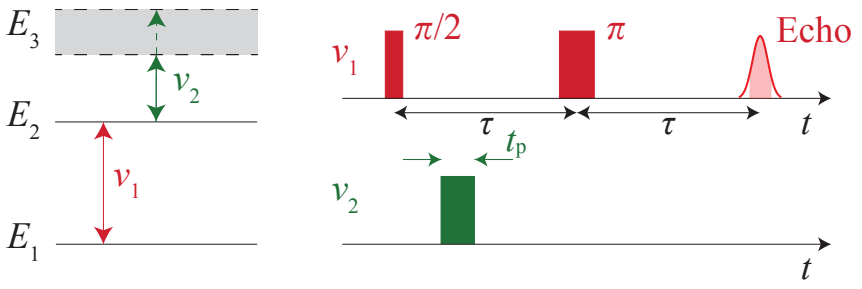

FIGURE 6.12: Schematic showing the 'echo kill' sequence. The unknown frequency, ν_2 (green) is varied, such that we search the range of possible E_3 values, marked left in grey. If a third level satisfying the necessary criteria (discussed in the text) is found, the intensity of the observed echo (red) at ν_1 decreases.

The transition chosen at $\theta = 45°$ is marked with a red arrow on figure 6.11(a) and the results of the echo kill experiment are shown in figure 6.11(b). We note firstly the dip at $\nu_1 - \nu_2 = 0$. This corresponds to both channels, red and green, acting on the E_1, E_2 transition, such that the second pulse reduces population in the superposition state. There is also, however, a second peak, at distinct ν_2. We conclude from our observations that, at this frequency, we have moved population from E_2 to E_3, which reduces the original echo intensity, and forms a coherence between E_2 and E_3. We have therefore identified a three level system which appears to satisfy all of our original constraints. The only issue, however, is that we do not know to which states these levels correspond.

Attempts were made to compare the $\theta = 45°$ data to the simulated EFS, which would allow state identification, however, the density of lines was such that it was not possible to match them up. Furthermore, due to the different frequencies of precession, altering either the power or duration of the applied microwave pulses in the Hahn sequence, increases and decreases the amplitudes of different lines. This points to the possibility that not all allowed transitions are even excited in the observed ESR spectrum. One must also consider sensitivity of the spectrum to error in alignment. As discussed earlier, the sample was mounted onto the flat surface of a quartz rod, such that the rotation axis was perpendicular to the *ac*-plane. The error in this, corresponding to the how close to vertical the rod could be inserted, owing to slight freedom of the rod to move, was approximately 2 degrees. B_0 was aligned with the *c*-axis by identification of the relevant turning points with respect to θ. Error in this was approximately one degree,

corresponding to difficulty in identification of the turning point. Intermediate angles were found through use of a goniometer. Error in rotation from the 'chosen' c-axis position was 0.5 degrees, constrained by accuracy of the goniometer. It was found that the combination of these errors and sensitivity to small changes in power resulting from a slightly altered Q-factor, meant that intermediate angle EFS spectra were not repeatable from session to session. It was, however, on all occasions possible to identify some three level system satisfying our constraints.

It was thought that an alternative way to identify transition character, could be to perform a nutation experiment at some power, as discussed in section 6.2.2, on a given transition and to use the nutation frequency to identify between which states the transition had occurred and to allow us to pick out the desired first transition. This proved highly effective at $\theta = 0°$, with each group of transitions (marked in figure 6.10) exhibiting a distinct nutation frequency. However, there was no correspondence between these frequencies and those observed in nutation experiments performed at $\theta = 45°$. Without a clear expectation of the nutation frequency for each transition type, of which at intermediate angles there are many, this is not a viable method.

6.3.3 Upper Level Nutation Experiments

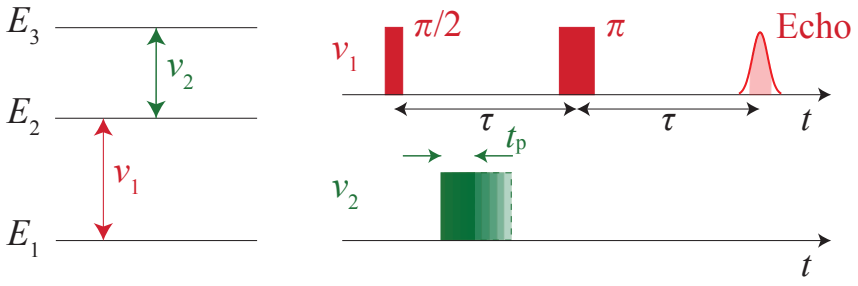

FIGURE 6.13: Schematic showing the upper level nutation sequence. The length of the ν_2 pulse (green), t_p is incremented, such that we perform coherent oscillations between E_2 and E_3. This is observed via an oscillation in the intensity of the observed echo (red).

Now that we have a suitable three level system from the ZnO landscape, we want to perform manipulations within it. Earlier in the chapter, we proved the possibility of coherent manipulation of Cr_7Zn by performing nutation experiments on a given transition.

Analogous to this, we will aim to use nutation experiments to prove the possibility of coherent manipulation up to the third level in our trio of states. All experiments presented in this section were taken in the $\theta = 45°$ position of figure 6.11. The pulse sequence we will use, similar to that in the 'echo kill' experiment, is illustrated by figure 6.13. As before, a Hahn echo is tuned at ν_1, and a pulse at ν_2 is added after the initial $\pi/2$-pulse. This is chosen to correspond to the dip at non-zero $\nu_1 - \nu_2$ in our echo kill spectrum, marked in figure 6.11(b) by a green arrow. Then, rather than sweeping the frequency of this pulse, we increase its length and observe, as a function of this, the intensity of the echo on the ν_1 transition. Note that in contrast to the nutation experiments of section 6.2.2, we are now using an indirect method of detection, measuring coherence on the E_1, E_2 transition to prove nutation between E_2 and E_3.

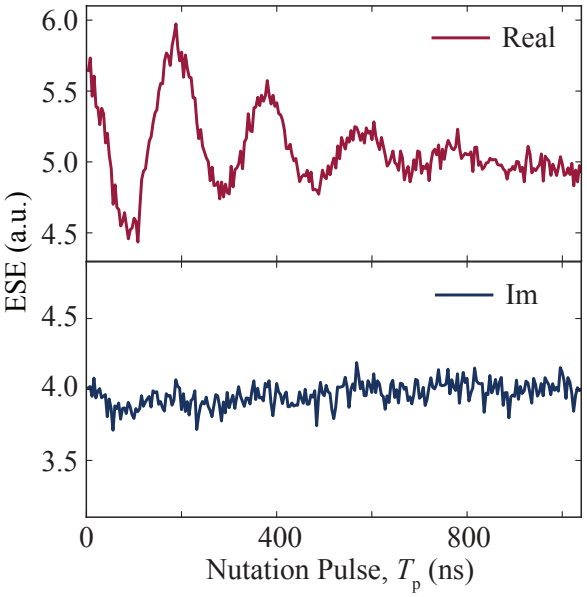

FIGURE 6.14: Real (red) and imaginary (blue) channel results of an upper level nutation experiment (illustrated by figure 6.13) measured at $T = 50$ K, with $B_0 = 376.8$ mT and $\theta = 45°$. $\nu_1 = 9.722$ GHz, $\nu_2 = 9.650$ GHz, length of ν_1 π-pulse = 144 ns and $\tau = 2000$ ns.

Figure 6.14 shows the result of this experiment. We see clear oscillations, much like those obtained in section 6.2.2. Both real and imaginary components of the signal are plotted in order to verify that the result is not merely a 'Bloch-Siegert shift': a change in phase resulting from a small shift in resonance frequency, which can sometimes be induced by an off resonance pulse [92]. Given that oscillation is visible only in the real channel, we conclude that this is not the case and that we do in fact have a changing population.

With our ν_2 pulse, we perform coherent manipulations between E_2 and E_3, generating arbitrary superposition states. This is observed firstly as a dip in the original echo and, after a π pulse on ν_2, the echo's gradual restoration. The cycle then continues. This was observed regardless of whether the pulses at ν_1 and ν_2 were triggered coherently, i.e. whether they began with the same phase relation for every measurement shot.

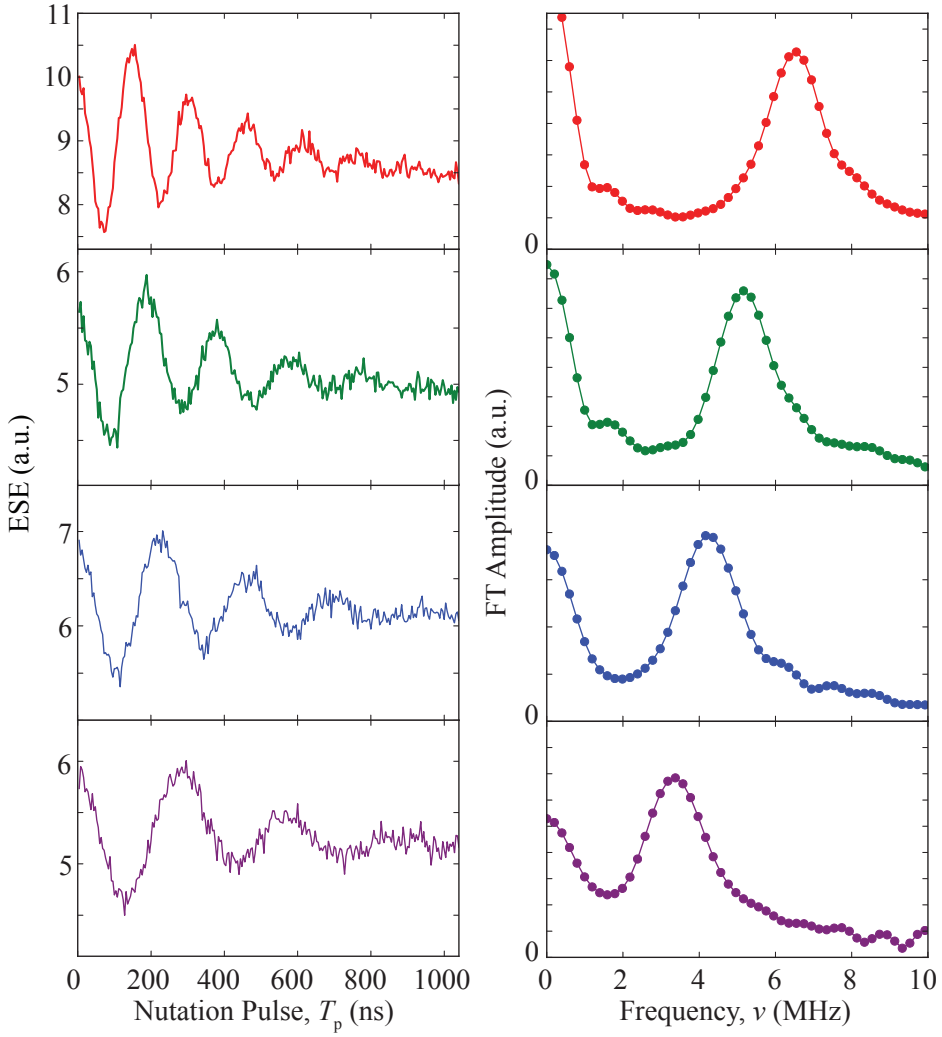

FIGURE 6.15: Left: upper level nutation experiment at $T = 50$ K, with $B_0 = 376.8$ mT and $\theta = 45°$, for a range of attenuation settings (marked). $\nu_1 = 9.722$ GHz, $\nu_2 = 9.650$ GHz, length of ν_1 π-pulse = 144 ns and $\tau = 2000$ ns. Right: Fourier transforms of the nutations.

The next step was to vary the power of the ν_2 pulse in order to vary the frequency of nutation. The range chosen was limited largely by possible pulse lengths. Lower powers resulting in lower nutation frequencies require observation across a larger time window. This increases the required τ time in the ν_1 Hahn sequence and consequently

reduces the signal intensity. The more this is increased, the lower our signal to noise. Figure 6.15 shows the resulting data, along with the corresponding Fourier transforms. We see that the nutation frequency does vary with power and figure 6.16 confirms that the relationship between frequency and B_1 is linear.

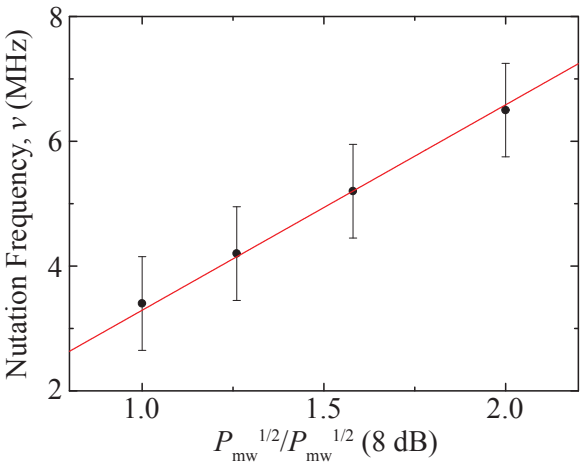

FIGURE 6.16: Upper level nutation frequency as a function of the square root of applied microwave power relative to that when a high power attenuation of 8 dB is applied (black circles; measured at $T = 50$ K, $B_0 = 376.8$ mT, $\theta = 45°$, length of ν_1 π-pulse = 144 ns and $\tau = 2000$ ns). Error bars are derived from the full width at half maximum of the corresponding peaks in the Fourier transformed data (figure 6.15. The linear least squares fit (red line) was constrained to go through the origin.

We note that in this case it is difficult to say conclusively whether oscillations decay on a given timescale or after a fixed number of oscillations, as was the case for $Cr_7Zn@Ga_7Zn$. We no longer expect to suffer from significant D-strain and from the effects of crystal mosaicity. Therefore, likely dominant sources of oscillation decay include B_1 inhomogeneity and intrinsic decoherence on the E_2, E_3 transition.

6.3.4 Initialisation

An important step, when performing quantum information algorithms is the initialisation of the system into a known pure state. The paper of Loss et al. proposes the initial application of a strong magnetic field to force spins into the lowest energy level. Here, we take a different approach. A highly mixed system can be viewed as the sum of a fully mixed component and a small pure component. In terms of density matrices, this is given by

$$\rho = \frac{(1-\epsilon)}{d}\hat{I} + \epsilon\rho_0, \tag{6.3}$$

where $\hat{I}$ is the identity matrix, d is the dimensionality of the system (in the present case, $d = 3$), ρ_0 represents the pure component and ϵ is a constant less than one, giving the fraction of the system in ρ_0. The unitary matrices of ESR manipulations leave the identity component unchanged, and do not produce effects measurable using ESR. We therefore ignore this part and assume any observed results are due entirely to ρ_0. This is known as the 'pseudo pure approximation' [36, 165].

If we begin in a thermal state, as has been the case in all our earlier experiments, ρ_0 in equation 6.3 is still a mixed state, with diagonal elements governed by the Boltzmann distribution:

$$\rho_0 \propto \begin{pmatrix} 1 & 0 & 0 \\ 0 & 1-\delta_1 & 0 \\ 0 & 0 & 1-\delta_2 \end{pmatrix}. \tag{6.4}$$

where δ_1 and δ_2 are the thermally induced population differences. This does not fit into the pseudopure framework. However, if we apply a $\pi/2$ pulse at ν_2, we can equalise the populations of the upper two levels. If we then wait long enough that the coherence between them is destroyed (on the timescale of T_2 for the transition), but not long enough that the states thermalise (on the timescale of T_1), the effect is to form the state:

$$\begin{aligned} \rho_0 &\propto \begin{pmatrix} 1 & 0 & 0 \\ 0 & 1-(\delta_1+\delta_2)/2 & 0 \\ 0 & 0 & 1-(\delta_1+\delta_2)/2 \end{pmatrix} \\ &= \left(1 - \frac{(\delta_1+\delta_2)}{2}\right)\hat{I} + \frac{(\delta_1+\delta_2)}{2}\begin{pmatrix} 1 & 0 & 0 \\ 0 & 0 & 0 \\ 0 & 0 & 0 \end{pmatrix}. \end{aligned} \tag{6.5}$$

The resulting fully mixed component, proportional to $\hat{I}$, is absorbed into the original fully mixed part and we are left with our pseudopure state, upon which our pulse sequence acts. The addition of this initialisation step is shown in figure 6.17 for the upper level nutation experiment.

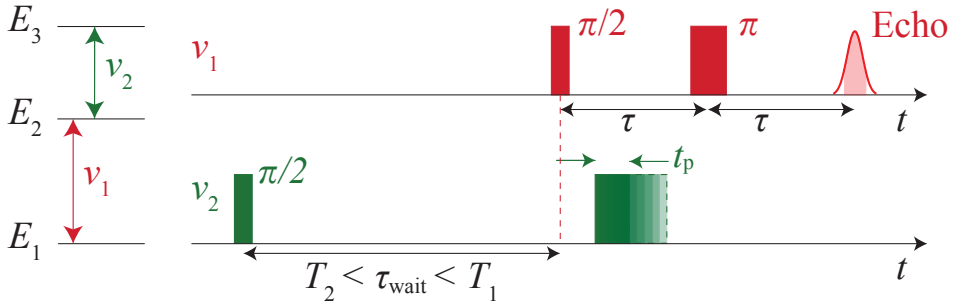

FIGURE 6.17: Schematic showing the upper level nutation sequence with initialisation. An additional $\pi/2$ pulse at ν_2 (green) is added at time $t = 0$ to equalise the populations of E_2 and E_3. We then wait for time τ_{wait} such that the coherence between them is destroyed but that the populations remain roughly equal. The sequence then proceeds as before.

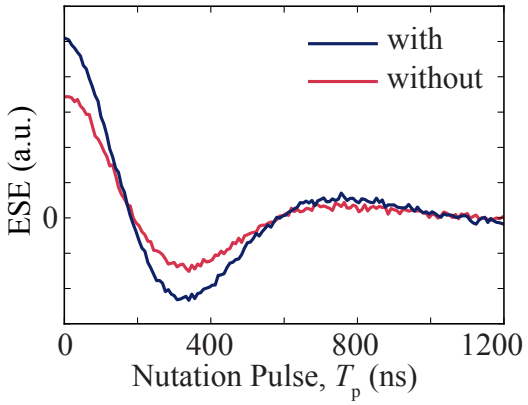

FIGURE 6.18: Results of an upper level nutation experiment with (blue) and without (red) initialisation of the system (illustrated by figure 6.17). Measured at $T = 50$ K, with $B_0 = 355.4$ mT and $\theta = 45°$. $\nu_1 = 9.601$ GHz, $\nu_2 = 9.557$ GHz, length of ν_1 π-pulse = 256 ns and $\tau = 2000$ ns. $\tau_{\text{wait}} = 50$ μs, length of ν_2 $\pi/2$-pulse = 128 ns.

Figure 6.18 shows a comparison of two upper level nutation experiments, with all parameters identical expect for the fact that one was recorded with an initialisation pulse and one without. We see that introduction of this step does not make a significant difference to the observed signal, however, it does enhance the oscillation amplitude slightly. Further enhancement could be achieved by working at a lower temperature such that T_1/T_2 were larger [42]. This would allow a longer wait time, such that unwanted coherence

resulting from the initialisation pulse decayed further, with very little re-thermalisation of the population. This would, however, require a longer shot repetition such that experiments were more time consuming.

6.4 Conclusions

In conclusion, we have explored the use of MNMs of spin $S > 1/2$ for the implementation of quantum algorithms. We first tackled the issue that in order to be useful, we require our molecular magnets to be in a dilute oriented ensemble of spins. By doping Cr_7Zn ($S = 3/2$) into the diamagnetic and isostructural host Ga_7Zn, we were able to perform the first ever coherent manipulations of such a dilute oriented ensemble of MNMs. We presented nutation data over a range of applied powers, proving the potential of high spin MNMs to host quantum algorithms requiring manipulation over multiple levels.

We also explored the manipulation of spins across a three level system, using the test system Mn:ZnO ($S = 5/2$; $I = 5/2$). Although identifying the states involved was not possible, we developed a method to find suitable three level systems within the rich Mn:ZnO landscape of states. We presented data showing indirectly detected nutation between the upper two levels over a range of applied powers. In addition, a method for initialisation of the selected three level system into a pseudopure state was presented and data showed this to enhance the amplitude of observed upper level nutations. It is hoped that the developed methods will in future be applied to a dilute oriented ensemble of MNMs, making a valuable contribution to the field of MNMs for QIP.

Chapter 7

Conclusions

In conclusion, motivated by their potential for use as elements in quantum information processing, we have explored, using the technique of electron spin resonance, a variety of compounds based on the class of molecular nanomagnets, Cr_7M. At temperatures below about $T = 7$ K, these rings of antiferromagnetically exchange coupled ions form a coherent 'giant' ground state spin of size dependent upon the choice of M. They offer long phase memory times (up to 15 μs at 1.5 K), chemically tuneable structures, and identical units on a length scale one could feasibly address with an individual gate.

We began by presenting a study on the effects of replacing H, known to be a dominant source of decoherence, with deuterium, fluorine or chlorine, in Cr_7Ni ($S = 1/2$) rings. This was firstly found to be challenging from a synthetic perspective, with the increased size of the halogens causing instability in some of the resulting compounds in solution. The decoherence mechanisms of those which were stable were dominated by structural effects. In particular, the use of fluorine appeared to hinder decoherence driven by the central templating cation. We concluded that halogenation does not seem to be a productive strategy for phase memory time extension in Cr_7Ni based compounds.

Moving on to tackle the requirement for a scalable architecture, we presented the asymmetric dimer, $N@C_{60}$(py)-Cr_7Ni. It was found that measurement of phase memory time across a range of temperatures for the highly coherent N spin, which is coupled to the ring via a magnetic dipolar interaction, provided insight into the ring's spin dynamics.

We were able to identify three distinct regimes. At high temperature, fluctuations on the ring are so rapid that the N@C_{60} appears magnetically disconnected. As these magnetic fluctuations begin to slow towards the timescale of the dipolar interaction between Cr_7Ni and the N spin, we see a sharp rise in the decoherence rate of the N spin, peaking at $T \approx 5$ K. At the lowest temperatures, a recovery of the relaxation rate reflects the onset of the ring's coherent ground state. It was found that the peak in decoherence rate as a function of temperature was broader in the case of the dimer, reflecting the broader distributions of dipolar interaction energies experienced by the N spins.

In order to explore their potential for the implementation of two qubit gates, we investigated two groups of Cr_7Ni-Cr_7Ni dimers: those threaded on a rigid axle (the rotaxanes) and those linked chemically. Through use of double electron-electron resonance, the strength of the ring-ring dipolar interaction, governing the two qubit gate time, was estimated for each compound. It was found that many exhibited the hierarchy of timescales required for implementation of a two qubit gate: a short single qubit manipulation time (~ 10 ns in ESR), intermediate two-qubit gate time and long phase coherence time. The rotaxanes proved most suitable, with observed ratios of T_{m} to two-qubit gate time of up to 38.9. A possible scheme for the future implementation of a CNOT gate in these systems was presented.

We finally turned to the potential use of rings of spin, $S > 1/2$, as was originally proposed by Loss et al.. In order to exploit the advantage of such spins, their anisotropy requires that they be aligned. The chapter began by presenting the first ever coherent measurements on a dilute oriented ensemble of molecular nanomagnets. Nutations were performed with a range of applied powers on the $S = 3/2$ ring, Cr_7Zn, which had been doped into the isostructural and diamagnetic host crystal, Ga_7Zn. We moved on to consider the test system, Mn:ZnO, whose anisotropic Mn^{2+} ($s = 5/2$, $I = 5/2$) defect ions offer a rich transition landscape, ideal for pulse sequence development. We developed the 'echo kill' method for identification of a three level subsystem whose transition frequencies both fall within the cavity bandwidth. Such a subsystem was then used to perform indirectly detected nutations between the upper two levels over a

range of applied powers. In addition, a method for initialisation of the subsystem into a pseudopure state was presented and shown to enhance nutation amplitude.

Appendix A

Chemical Linkers for Cr_7Ni-Cr_7Ni Dimers

Figure A.1 shows the structures of the three chemical linkers used in the dimer compounds **2A**, **2B** and **2C**.

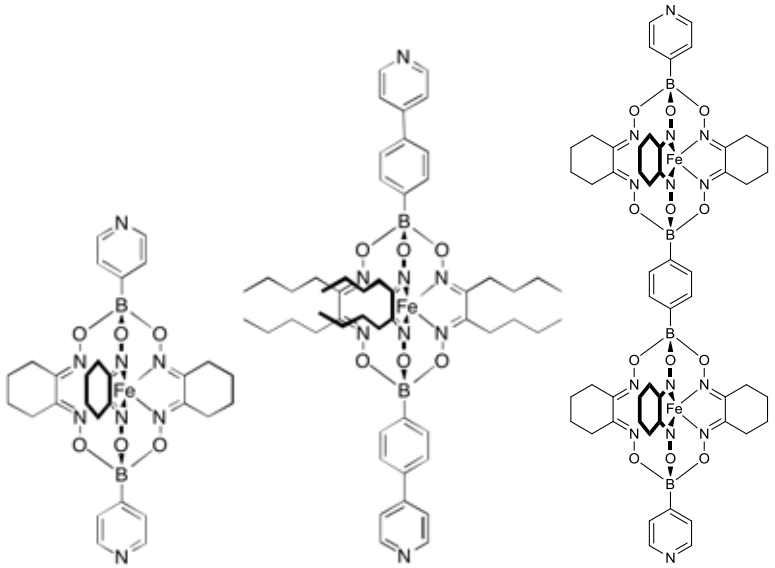

(L1) (L2) (L3)

FIGURE A.1: Structures of the chemical linkers L1, L2 and L3 used in the compounds **2A**, **2B** and **2C**, respectively. Synthesised as described in the relevant publication [166].

Bibliography

[1] M. A. Nielson and I. L. Chuang. *Quantum Computation and Quantum Information*. Cambridge University Press, 2000.

[2] D. Deutsch. Quantum theory, the Church-Turing principle and the universal quantum computer. *P. Roy. Soc. Lond. A Mat.*, 400(July 1984):97–117, 1985.

[3] P. W. Shor. Polynomial-Time Algorithms for Prime Factorization and Discrete Logarithms on a Quantum Computer. *J. Sci. Statist. Comput.*, 26:1484, 1997.

[4] R. L. Rivest, A. Shamir, and L. Adleman. A Method for Obtaining Digital Signatures and Public-Key Cryptosystems. *Communications of the ACM*, 21(2):120, 1978.

[5] L. K. Grover. Quantum Mechanics Helps in Searching for a Needle in a Haystack. *Phys. Rev. Lett.*, 79(2):325–328, 1997.

[6] R. P. Feynman. Simulating physics with computers. *Int. J. Theor. Phys.*, 21(6-7):467–488, June 1982.

[7] J. I. Cirac and P. Zoller. Goals and opportunities in quantum simulation. *Nature Physics*, 8(4):264–266, April 2012.

[8] D. P. DiVincenzo. The Physical Implementation of Quantum Computation. *Fortschr. Phys.*, 48:771–783, February 2000.

[9] D. D. Awschalom, L. C. Bassett, A. S. Dzurak, E. L. Hu, and J. R. Petta. Quantum Spintronics: Engineering and Manipulating Atom-Like Spins in Semiconductors. *Science (New York, N.Y.)*, 339(6124):1174–9, March 2013.

[10] T. D. Ladd, F. Jelezko, R. Laflamme, Y. Nakamura, C. Monroe, and J. L. O'Brien. Quantum computers. *Nature (London)*, 464(7285):45–53, March 2010.

[11] C. Monroe and J. Kim. Scaling the Ion Trap Quantum Processor. *Science (New York, N.Y.)*, 339(6124):1164–9, March 2013.

[12] J. L. O'Brien, G. J. Pryde, A. G. White, T. C. Ralph, and D. Branning. Demonstration of an all-optical quantum controlled-NOT gate. *Nature*, 426(6964):264–267, 2003.

[13] S. J. Devitt, A. D. Greentree, R. Ionicioiu, J. L. O'Brien, W. J. Munro, and L. C. L. Hollenberg. Photonic module: An on-demand resource for photonic entanglement. *Physical Review A - Atomic, Molecular, and Optical Physics*, 76(5):1–7, 2007.

[14] T. E. Northup and R. Blatt. Quantum information transfer using photons. *Nat. Photon.*, 8(5):356–363, 2014.

[15] N. E. Bonesteel, L. Hormozi, G. Zikos, and S. H. Simon. Braid topologies for quantum computation. *Physical Review Letters*, 95(14):1–4, 2005.

[16] A. Stern and N. H. Lindner. Topological Quantum Computation–From Basic Concepts to First Experiments. *Science (New York, N.Y.)*, 339(6124):1179–84, March 2013.

[17] M. H. Devoret, A. Wallraff, and M. Martinis. Superconducting Qubits: A Short Review. *Arxiv preprint cond-mat/0411174*, page 41, 2004.

[18] M. H. Devoret and R. J. Schoelkopf. Superconducting Circuits for Quantum Information: An Outlook. *Science (New York, N.Y.)*, 339(6124):1169–74, March 2013.

[19] C. Chappert, A. Fert, and F. N. Van Dau. The emergence of spin electronics in data storage. *Nature Mater.*, 6(11):813–23, November 2007.

[20] R. Coehoorn. Giant Magnetoresistance and Magnetic Interactions in Exchange-Biased Spin-Valves. In K. H. J. Buschow, editor, *Handbook of Magnetic Materials, Volume 15*, chapter 1, page 6. Elsevier, 2003.

[21] S. A. Wolf, D. D. Awschalom, R. A. Buhrman, J. M. Daughton, S. von Molnár, M. L. Roukes, A. Y. Chtchelkanova, and D. M. Treger. Spintronics: A Spin-Based Electronics Vision for the Future. *Science (New York, N.Y.)*, 294(November):1488–1495, 2001.

[22] J. Zhu and C. Park. Magnetic tunnel junctions. *Materials Today*, 9(11):36–45, 2006.

[23] S. Ikeda, J. Hayakawa, Y. Ashizawa, Y. M. Lee, K. Miura, H. Hasegawa, M. Tsunoda, F. Matsukura, and H. Ohno. Tunnel magnetoresistance of 604% at 300 K by suppression of Ta diffusion in CoFeB/MgO/CoFeB pseudo-spin-valves annealed at high temperature. *Applied Physics Letters*, 93:8–10, 2008.

[24] S. D. Bader and S. S. P. Parkin. Spintronics. *Annual Review of Condensed Matter Physics*, 1:71–88, 2010.

[25] D. Loss and D. P. DiVincenzo. Quantum computation with quantum dots. *Phys. Rev. A*, 57(1):120–126, January 1998.

[26] C. Kloeffel and D. Loss. Prospects for Spin-Based Quantum Computing in Quantum Dots. *Annual Review of Condensed Matter Physics*, 4(1):51–81, April 2013.

[27] M. Atatüre, J. Dreiser, A. Badolato, A. Högele, K. Karrai, and A. Imamoglu. Quantum-Dot Spin-State Preparation. *Science*, 312(April):551–554, 2006.

[28] B. D. Gerardot, D. Brunner, P. A. Dalgarno, P. Ohberg, S. Seidl, M. Kroner, K. Karrai, N. G. Stoltz, P. M. Petroff, and R. J. Warburton. Optical pumping of a single hole spin in a quantum dot. *Nature*, 451(7177):441–444, 2008.

[29] T. M. Godden, S. J. Boyle, A. J. Ramsay, A. M. Fox, and M. S. Skolnick. Fast high fidelity hole spin initialization in a single InGaAs quantum dot. *Applied Physics Letters*, 97(6), 2010.

[30] E. Uccelli, J. Bauer, M. Bichler, D. Schuh, J. J. Finley, G. Abstreiter, and A. F. Morral. Self-assembly of InAs Quantum Dot Structures on Cleaved Facets. In Z. M. Wang, editor, *Self Assembled Quantum Dots*, chapter 2, pages 1–38. 2008.

[31] J. A. Jones. Quantum Computing with NMR. *Progress in Nuclear Magnetic Resonance Spectroscopy*, 59(2):91–120, 2010.

[32] J. A. Jones and M. Mosca. Implementation of a quantum algorithm on a nuclear magnetic resonance quantum computer. *Journal of Chemical Physics*, 109(1998):1648–1653, 1998.

[33] I. L. Chuang, L. M. K. Vandersypen, X. Zhou, D. W. Leung, and S. Lloyd. Experimental realization of a quantum algorithm. *Nature*, 393(6681):143–146, 1998.

[34] S. Meiboom and D. Gill. Modified spin-echo method for measuring nuclear relaxation times. *Review of Scientific Instruments*, 29(8):688–691, 1958.

[35] MIT Department of Chemistry Instrumentation Facility. NMR Frequency Table.

[36] S. Simmons, R. M. Brown, H. Riemann, N. V. Abrosimov, P. Becker, H.-J. Pohl, M. L. W. Thewalt, K. M. Itoh, and J. J. L. Morton. Entanglement in a solid-state spin ensemble. *Nature (London)*, 470(7332):69–72, February 2011.

[37] M. Horodecki, P. Horodecki, and R. Horodecki. Separability of mixed states: necessary and sufficient conditions. *Physics Letters A*, 223(1-2):1–8, 1996.

[38] A. Peres. Seperability Criterion for Density Matrices. *Physical Review Letters*, 77(8):1413, 1996.

[39] S. J. Glaser. NMR quantum computing. *Angewandte Chemie - International Edition*, 40(1):147–149, 2001.

[40] J. J. L. Morton, D. R. McCamey, M. A. Eriksson, and S. A. Lyon. Embracing the quantum limit in silicon computing. *Nature (London)*, 479(7373):345–53, November 2011.

[41] J. J. L. Morton, A. M. Tyryshkin, R. M. Brown, S. Shankar, B. W. Lovett, A. Ardavan, T. Schenkel, E. E. Haller, J. W. Ager, and S. A. Lyon. Solid-state quantum memory using the ^{31}P nuclear spin. *Nature (London)*, 455(7216):1085–1088, October 2008.

[42] R. E. George, J. P. Edwards, and A. Ardavan. Coherent Spin Control by Electrical Manipulation of the Magnetic Anisotropy. *Phys. Rev. Lett.*, 110(2):027601, January 2013.

[43] T. Gaebel, M. Domhan, I. Popa, C. Wittmann, P. Neumann, F. Jelezko, J. R. Rabeau, N. Stavrias, A. D. Greentree, S. Prawer, J. Meijer, J. Twamley, P. R. Hemmer, and J. Wrachtrup. Room-temperature coherent coupling of single spins in diamond. *Nature Physics*, 2(6):408–413, 2006.

[44] P. Neumann, N. Mizuochi, F. Rempp, P. Hemmer, H. Watanabe, S. Yamasaki, V. Jacques, T. Gaebel, F. Jelezko, and J. Wrachtrup. Multipartite Entanglement Among Single Spins in Diamond. *Science*, 320(5881):1326–9, June 2008.

[45] A. Dzurak. Diamond and silicon converge. *Nature (London)*, 479:47, 2011.

[46] A. L. Falk, B. B. Buckley, G. Calusine, W. F. Koehl, V. V. Dobrovitski, A. Politi, C. A. Zorman, P. X.-L. Feng, and D. D. Awschalom. Polytype control of spin qubits in silicon carbide. *Nature communications*, 4(May):1819, 2013.

[47] M. N. Leuenberger and D. Loss. Quantum computing in molecular magnets. *Nature (London)*, 410(6830):789–93, April 2001.

[48] D. Gatteschi, R. Sessoli, and J. Villain. *Molecular Nanomagnets*. Oxford University Press, 2006.

[49] S. J. Blundell and F. L. Pratt. Organic and molecular magnets. *J. Phys.: Condens. Matter*, 16(24):R771–R828, June 2004.

[50] M. Takahashi, P. Turek, Y. Nakazawa, M. Tamura, K. Nozawa, D. Shiomi, M. Ishikawa, and M. Kinoshita. Discovery of a Quasi-1D Organic Ferromagnet, *p*-NPNN. *Phys. Rev. Lett.*, 67(6):746–748, 1991.

[51] P. Hammar, M. Stone, Daniel Reich, C. Broholm, P. Gibson, M. Turnbull, C. Landee, and M. Oshikawa. Characterization of a quasi-one-dimensional spin-1/2 magnet which is gapless and paramagnetic for $g\mu_B H \lesssim J$ and $k_B T \ll J$. *Phys. Rev. B*, 59(2):1008–1015, January 1999.

[52] F. M. Woodward, A. S. Albrecht, C. M. Wynn, C. P. Landee, and M. M. Turnbull. Two-dimensional $S = 12$ Heisenberg antiferromagnets: Synthesis, structure, and magnetic properties. *Phys. Rev. B*, 65(14):144412, March 2002.

[53] T. Lancaster, S. J. Blundell, M. L. Brooks, P. J. Baker, F. L. Pratt, J. L. Manson, C. P. Landee, and C. Baines. Magnetic order in the quasi-one-dimensional spin-1/2 molecular chain compound copper pyrazine dinitrate. *Phys. Rev. B*, 73(2):020410(R), January 2006.

[54] E. Čižmár, S. A. Zvyagin, R. Beyer, M. Uhlarz, M. Ozerov, Y. Skourski, J. L. Manson, J. A. Schlueter, and J. Wosnitza. Magnetic properties of the quasi-two-dimensional S=1/2 Heisenberg antiferromagnet $[Cu(pyz)_2(HF_2)]PF_6$. *Phys. Rev. B*, 81(6):064422, February 2010.

[55] J. L. Manson, J. A. Schlueter, R. D. McDonald, and J. Singleton. Crystal Structure and Antiferromagnetic Ordering of Quasi-2D $[Cu(HF_2)(pyz)_2]TaF_6$ (pyz=pyrazine). *J. Low Temp. Phys.*, 159:15–19, January 2010.

[56] J. L. Manson, S. H. Lapidus, P. W. Stephens, P. K. Peterson, K. E. Carreiro, H. I. Southerland, T. Lancaster, S. J. Blundell, A. J. Steele, P. A. Goddard, F. L. Pratt, J. Singleton, Y. Kohama, R. D. McDonald, R. E. Del Sesto, N. A. Smith, J. Bendix, S. A. Zvyagin, J. Kang, C. Lee, M. Whangbo, V. S. Zapf, and A. Plonczak. Structural, Electronic, and Magnetic Properties of Quasi-1D Quantum Magnets $[Ni(HF_2)(pyz)_2]X$ (pyz = pyrazine; X = PF_6^-, SbF_6^-) Exhibiting Ni-FHF-Ni and Ni-pyz-Ni Spin Interactions. *Inorg. Chem.*, 50(13):5990–6009, July 2011.

[57] P. A. Goddard, J. L. Manson, J. Singleton, I. Franke, T. Lancaster, A. Steele, S. J. Blundell, C. Baines, F. L. Pratt, R. D. McDonald, O. Ayala-Valenzuela, J. Corbey, H. I. Southerland, P. Sengupta, and J. A. Schlueter. Dimensionality Selection in a Molecule-Based Magnet. *Phys. Rev. Lett.*, 108(7):077208, February 2012.

[58] J. L. Manson, K. E. Carreiro, S. H. Lapidus, P. W. Stephens, P. A. Goddard, R. E. Del Sesto, J. Bendix, S. Ghannadzadeh, I. Franke, J. Singleton, T. Lancaster, J. S. Möller, P. J. Baker, F. L. Pratt, S. J. Blundell, J. Kang, C. Lee, and M.-H. Whangbo. Influence of HF_2^- geometry on magnetic interactions elucidated from polymorphs of the metal-organic framework $[Ni(HF_2)(pyz)_2]PF_6$ (pyz = pyrazine). *Dalton Transactions*, 41(24):7235, 2012.

[59] F. M. Woodward, P. J. Gibson, G. B. Jameson, C. P. Landee, M. M. Turnbull, and R. D. Willett. Two-Dimensional Heisenberg Antiferromagnets: Syntheses, X-ray Structures, and Magnetic Behaviour of $[Cu(pz)_2](ClO_4)_2$, $[Cu(pz)_2](BF_4)_2$, and $[Cu(pz)_2(NO_3)](PF_6)$. *Inorg. Chem.*, 46(3):4256–4266, 2007.

[60] C. P. Landee and M. M. Turnbull. Recent Developments in Low-Dimensional Copper(II) Molecular Magnets. *Eur. J. Inorg. Chem.*, (13):2266–2285, May 2013.

[61] A. J. Tasiopoulos, A. Vinslava, W. Wernsdorfer, K. A. Abboud, and G. Christou. Giant single-molecule magnets: A Mn_{84} torus and its supramolecular nanotubes. *Angewandte Chemie - International Edition*, 43(16):2117–2121, 2004.

[62] L. Thomas, F. Lionti, R. Ballou, D. Gatteschi, R. Sessoli, and B. Barbara. Macroscopic quantum tunnelling of magnetization in a single crystal of nanomagnets. *Nature (London)*, 383:145–147, 1996.

[63] B. Barbara, L. Thomas, F. Lionti, I. Chiorescu, and A. Sulpice. Macroscopic quantum tunneling in molecular magnets. *Journal of Magnetism and Magnetic Materials*, 200:167–181, 1999.

[64] D. Gatteschi and R. Sessoli. Quantum tunneling of magnetization and related phenomena in molecular materials. *Angewandte Chemie - International Edition*, 42(3):268–297, 2003.

[65] R. Sessoli, H.-L. Tsai, A. R. Schake, S. Wang, J. B. Vincent, K. Folting, D. Gatteschi, G. Christou, and D. N. Hendrickson. High-Spin Molecules: $[Mn_{12}O_{12}(O_2CR)_{16}(H_2O)_4]$. *J. Am. Chem. Soc*, 115(5):1804–1816, 1993.

[66] J. M. Clemente-Juan, E. Coronado, and A. Gaita-Ariño. Magnetic polyoxometalates: from molecular magnetism to molecular spintronics and quantum computing. *Chemical Society reviews*, 41(22):7464–78, November 2012.

[67] G. Chaboussant, A. Sieber, S. Ochsenbein, H.-U. Güdel, M. Murrie, A. Honecker, N. Fukushima, and B. Normand. Exchange interactions and high-energy spin states in Mn_{12}-acetate. *Physical Review B*, 70(10):104422, 2004.

[68] V. V. Mazurenko, Y. O. Kvashnin, Fengping Jin, H. A. De Raedt, A. I. Lichtenstein, and M. I. Katsnelson. First-principles modeling of magnetic excitations in Mn_{12}. *Physical Review B*, 89:214422, 2014.

[69] Oliver Hanebaum and Jürgen Schnack. Thermodynamic observables of Mn_{12}-acetate calculated for the full spin Hamiltonian. *Physical Review B*, 92(6):064424, 2015.

[70] N. Ishikawa, M. Sugita, T. Ishikawa, S. Y. Koshihara, and Y. Kaizu. Lanthanide double-decker complexes functioning as magnets at the single-molecular level. *Journal of the American Chemical Society*, 125(29):8694–8695, 2003.

[71] P. Zhang, Y. N. Guo, and J. Tang. Recent advances in dysprosium-based single molecule magnets: Structural overview and synthetic strategies. *Coordination Chemistry Reviews*, 257(11-12):1728–1763, 2013.

[72] J. Dreiser. Molecular lanthanide single-ion magnets: from bulk to submonolayers. *Journal of Physics: Condensed Matter*, 27(18):183203, 2015.

[73] L. Sorace, C. Benelli, and D. Gatteschi. Lanthanides in molecular magnetism: old tools in a new field. *Chemical Society reviews*, 40(6):3092–3104, 2011.

[74] V. Bellini, A. Olivieri, and F. Manghi. Density-functional study of the Cr_8 antiferromagnetic ring. *Physical Review B - Condensed Matter and Materials Physics*, 73(18):1–7, 2006.

[75] A. Bencini and D Gatteschi. *EPR of Exchange Coupled Systems*. Dover, 2012.

[76] E. Liviotti, S. Carretta, and G. Amoretti. S-mixing contributions to the high-order anisotropy terms in the effective spin Hamiltonian for magnetic clusters. *Journal of Chemical Physics*, 117(7):3361–3368, 2002.

[77] J. Van Slageren, R. Sessoli, D. Gatteschi, A. A. Smith, M. Helliwell, R. E. P. Winpenny, A. Cornia, A. L. Barra, A. G. M. Jansen, E. Rentschler, and G. A. Timco. Magnetic Anisotropy of the Antiferromagnetic Ring $[Cr_8F_8Piv_{16}]$. *Chemistry-a European Journal*, 8(1):277–285, 2002.

[78] N. V. Gerbeleu, Y. T. Struchkov, F. A. Timko, A. S. Batsanov, K. M. Indrichan, and G. A. Popovich. No Title. *Dokl. Akad. Nauk SSSR*, 313:1459, 1990.

[79] F. K. Larsen, E. J. L. McInnes, H. E. Mkami, J. Overgaard, S. Piligkos, G. Rajaraman, E. Rentschler, A. A. Smith, G. M. Smith, V. Boote, M. Jennings, G. A. Timco, and R. E. P. Winpenny. Synthesis and Characterisation of Heterometallic Cr_7M Wheels. *Angew. Chem.*, 42(1):101–105, 2003.

[80] F. Troiani, A. Ghirri, M. Affronte, S. Carretta, P. Santini, G. Amoretti, S. Piligkos, G. A. Timco, and R. E. P. Winpenny. Molecular Engineering of Antiferromagnetic Rings for Quantum Computation. *Phys. Rev. Lett.*, 94(20):207208, May 2005.

[81] S. Piligkos, H. Weihe, E. Bill, F. Neese, H. El Mkami, G. M. Smith, D. Collison, G. Rajaraman, G. A. Timco, R. E. P. Winpenny, and E. J. L. McInnes. EPR spectroscopy of a family of $Cr^{III}_7M^{II}$ (M = Cd, Zn, Mn, Ni) "wheels": studies of isostructural compounds with different spin ground sta. *Chem. Eur. J.*, 15(13):3152–67, January 2009.

[82] R. Caciuffo, T. Guidi, G. Amoretti, S. Carretta, E. Liviotti, P. Santini, C. Mondelli, G. A. Timco, C. A. Muryn, and R. E. P. Winpenny. Spin dynamics of heterometallic Cr_7M wheels (M=Mn, Zn, Ni) probed by inelastic neutron scattering. *Phys. Rev. B*, 71(17):174407, May 2005.

[83] G. A. Timco, E. J. L. McInnes, and R. E. P. Winpenny. Physical studies of heterometallic rings: an ideal system for studying magnetically-coupled systems. *Chem. Soc. Rev.*, 42(4):1796–806, February 2013.

[84] G. A. Timco, E. J. L. McInnes, R. G. Pritchard, F. Tuna, and R. E. P. Winpenny. Heterometallic Rings Made From Chromium Stick Together Easily. *Angew. Chem., Int. Ed.*, 47(50):9681–9684, December 2008.

[85] G. A. Timco, S. Carretta, F. Troiani, F. Tuna, R. J. Pritchard, C. A. Muryn, E. J. L. McInnes, A. Ghirri, A. Candini, P. Santini, G. Amoretti, M. Affronte, and R. E. P. Winpenny. Engineering the coupling between molecular spin qubits by coordination chemistry. *Nature Nanotech.*, 4(March):173, 2009.

[86] G. A. Timco, T. B. Faust, F. Tuna, and R. E. P. Winpenny. Linking heterometallic rings for quantum information processing and amusement. *Chemical Society reviews*, 40(6):3067–3075, 2011.

[87] J. Tejada, E. M. Chudnovsky, E. del Barco, J. M. Hernandez, and T. P. Spiller. Magnetic qubits as hardware for quantum computers. *Nanotechnology*, 12:181–186, 2001.

[88] A. Ardavan, O. Rival, John J. L. Morton, S. J. Blundell, A. M. Tyryshkin, G. A. Timco, and R. E. P. Winpenny. Will Spin-Relaxation Times in Molecular Magnets Permit Quantum Information Processing? *Phys. Rev. Lett.*, 98(5):057201, January 2007.

[89] C. J. Wedge, G. A. Timco, E. T. Spielberg, R. E. George, F. Tuna, S. Rigby, E. J. L. McInnes, R. E. P. Winpenny, S. J. Blundell, and A. Ardavan. Chemical Engineering of Molecular Qubits. *Phys. Rev. Lett.*, 108(10):107204, March 2012.

[90] Bruker. Basic Concepts of EPR Resonators. In *User Service Training Course*, pages 1–26. Bruker.

[91] G. R. Eaton, S. S. Eaton, D. P. Barr, and R. T. Weber. *Quantitative EPR: A practitioners guide*. 2010.

[92] A. Schweiger and G. Jeschke. *Principles of Pulse Electron Paramagnetic Resonance*. Oxford University Press, 2001.

[93] O. Rival. *Organic Materials for Quantum Computation*. PhD thesis, University of Oxford, 2009.

[94] D. N. Stamires and J. Turkevich. Electron Paramagnetic Resonance in Some Molecular Charge Transfer Complexes. *Journal of the American Chemical Society*, 85(17):2557–2561, 1963.

[95] J. R. Klauder and P. W. Anderson. Spectral Diffusion Decay in Spin Resonance Experiments. *Physical Review*, 125(3):912–932, 1962.

[96] C. Cohen-Tannoudji, B. Diu, and F. Laloe. *Quantum Mechanics (Vol. 2)*. WILEY-VCH Verlag GmbH & Co., 1991.

[97] M. Matsushita, T. Momose, and T. Shida. Internal rotation of the methyl group in the radical cation of dimethyl ether. *Journal of Chemical Physics*, 92(1990):4749, 1990.

[98] S. Kubota, M. Matsushita, T. Shida, A. Abu-Raqabah, M. C. R. Symons, and J. L. Wyatt. Internal Rotation of the Methyl Groups in the *t*-Butyl Radical as Studied by ESR. *Bull. Chem. Soc. Jpn.*, 68:140–145, 1995.

[99] S. S. Eaton and G. R. Eaton. Relaxation Times of Organic Radicals and Transition Metal Ions. In G. R. Eaton, S. S. Eaton, and L. J. Berliner, editors, *Biological Magnetic Resonance*, chapter 2, page 29. Springer-Verlag, Berlin, 2000.

[100] D. Kaminski, A. L. Webber, C. J. Wedge, J. Liu, G. A. Timco, I. J. Vitorica-Yrezabal, E. J. L. McInnes, R. E. P. Winpenny, and A. Ardavan. Quantum spin coherence in halogen-modified Cr_7Ni molecular nanomagnets. *Physical Review B*, 90(18):1–4, 2014.

[101] J. H. Freed. Quantum Effects of Methyl-Group Rotations in Magnetic Resonance: ESR Splittings and Linewidths. *The Journal of Chemical Physics*, 43(5):1710–1720, 1965.

[102] J. L. Carolan, S. Clough, N. D. McMillan, and B. Mulady. Proton relaxation and hyperfine structure due to tunnelling methyl groups. *Journal of Physics C: Solid State Physics*, 5(5):631–640, 2001.

[103] I. M. Brown. Electron Spin-Echo Studies of Relaxation Processes in Molecular Solids. In L. Kevan and R. N. Schwartz, editors, *Time Domain Electron Spin Resonance*, chapter 6. Wiley Interscience, New York, 1979.

[104] K. M. Salikhov and Y. D. Tsvetkov. Electron Spin-Echo Studies of Spin-Spin Interactions in Solids. In L. Kevan and R. N. Schwartz, editors, *Time Domain Electron Spin Resonance*, chapter 7. Wiley Interscience, New York, 1979.

[105] M. Affronte, F. Troiani, A. Ghirri, A. Candini, M. Evangelisti, S. Carretta, P. Santini, G. Amoretti, S. Piligkos, G. A. Timco, and R. E. P. Winpenny. AF molecular rings for quantum computation. *Polyhedron*, 24(16-17):2562–2567, 2005.

[106] J. F. Annett. *Superconductivity, Superfluids and Condensates*. Oxford University Press, 2003.

[107] H. Amiri, A. Lascialfari, Y. Furukawa, F. Borsa, G. A. Timco, and R. E P Winpenny. Comparison of the magnetic properties and the spin dynamics in heterometallic antiferromagnetic molecular rings. *Physical Review B - Condensed Matter and Materials Physics*, 82(14):1–13, 2010.

[108] R. Dubey, M. S. Pavan, and G. R. Desiraju. Structural landscape of benzoic acid: using experimental crystal structures of fluorobenzoic acids as a probe. *Chem. Commun. (Cambridge, U.K.)*, 48(72):9020–2, September 2012.

[109] F. Diederich and R. L. Whetten. Beyond C_{60}: the higher fullerenes. *Accounts of Chemical Research*, 25(3):119–126, 1992.

[110] H.W. Kroto, J. R. Heath, S.C. O'Brien, R.F. Curl, and R.E. Smalley. C_{60}: Buckminsterfullerene. *Nature*, 318:162–163, 1985.

[111] R. D. Johnson, D. S. Bethune, and C. S. Yannoni. Fullerene Structure and Dynamics: A Magnetic Resonance Potpourri. *Accounts of Chemical Research*, 25(3):169–175, 1992.

[112] K. Kikuchi, S. Suzuki, Y. Nakao, N. Nakahara, T. Wakabayashi, H. Shiromaru, K. Saito, I. Ikemoto, and Y. Achiba. Isolation and characterization of the metallofullerene LaC_{82}. *Chemical Physics Letters*, 216(1-2):67–71, 1993.

[113] S. Nagase and K. Kobayashi. Metallofullerenes MC_{82} (M = Sc, Y, and La). A theoretical study of the electronic and structural aspects. *Chemical Physics Letters*, 2(1):57–63, 1993.

[114] S. Hino, H. Takahashi, K. Iwasaki, K. Matsumoto, T. Miyazaki, S. Hasegawa, K. Kikuchi, and Y. Achiba. Electronic Structure of Metallofullerene LaC_{82}: Electron Transfer from Lanthanum to C_{82}. *Phys. Rev. Lett.*, 71(25), 1993.

[115] J. J. L. Morton, A. M. Tyryshkin, A. Ardavan, K. Porfyrakis, S. A. Lyon, and G. A. D. Briggs. A new mechanism for electron spin echo envelope modulation. *Journal of Chemical Physics*, 122(17), 2005.

[116] S. C. Benjamin, A. Ardavan, G. A. D. Briggs, D. A. Britz, D. Gunlycke, J. Jefferson, M. A. G. Jones, D. F. Leigh, B. W. Lovett, A. N. Khlobystov, S. A. Lyon, J. J. L. Morton, K. Porfyrakis, M. R. Sambrook, and A. M. Tyryshkin. Towards a fullerene-based quantum computer. *J. Phys.: Condens. Matter*, 18(21):S867–S883, May 2006.

[117] J. J. L. Morton, A. M. Tyryshkin, A. Ardavan, K. Porfyrakis, S. A. Lyon, and G. A. D. Briggs. Environmental effects on electron spin relaxation in $N@C_{60}$. *Phys. Rev. B*, 76(8):085418, August 2007.

[118] B. Pietzak, M. Waiblinger, T. Almeida Murphy, A. Weidinger, M. Höhne, E. Dietel, and A. Hirsch. Buckminsterfullerene C_{60}: a chemical Faraday cage for atomic nitrogen. *Chemical Physics Letters*, 279(5-6):259–263, 1997.

[119] J. J. L. Morton, A. M. Tyryshkin, A. Ardavan, S. C. Benjamin, K. Porfyrakis, S. A. Lyon, and G. A. D. Briggs. The $N@C_{60}$ nuclear spin qubit: Bang-bang decoupling and ultrafast phase gates. *Phys. Stat. Sol. (b)*, 243(13):3028–3031, November 2006.

[120] R. M. Brown, A. M. Tyryshkin, K. Porfyrakis, E. M. Gauger, B. W. Lovett, A. Ardavan, S. A. Lyon, G. A. D. Briggs, and J. J. L. Morton. Coherent State Transfer between an Electron and Nuclear Spin in $^{15}N@C_{60}$. *Phys. Rev. Lett.*, 106(11):110504, March 2011.

[121] B. J. Farrington, M. Jevric, G. A. Rance, A. Ardavan, A. N. Khlobystov, G. A. D. Briggs, and K. Porfyrakis. Chemistry at the nanoscale: synthesis of an $N@C_{60}$-$N@C_{60}$ endohedral fullerene dimer. *Angew. Chem., Int. Ed. Engl.*, 51(15):3587–90, April 2012.

[122] G. Liu, A. N. Khlobystov, G. Charalambidis, G. Coutsolelos, G. A. D. Briggs, and K. Porfyrakis. $N@C_{60}$-Porphyrin: A Dyad of Two Radical Centers. *J. Am. Chem. Soc.*, 134:1938–1941, 2012.

[123] P. Santini, S. Carretta, E. Liviotti, G. Amoretti, P. Carretta, M. Filibian, A. Lascialfari, and E. Micotti. NMR as a Probe of the Relaxation of the Magnetization in Magnetic Molecules. *Phys. Rev. Lett.*, 94(7):077203, February 2005.

[124] A. Keren. Muons as probes of dynamical spin fluctuations: some new aspects. *J. Phys.: Condens. Matter*, 16(40):S4603–S4618, October 2004.

[125] T. Lancaster, S. J. Blundell, F. L. Pratt, I. Franke, A. J. Steele, P. J. Baker, Z. Salman, C. Baines, I. Watanabe, S. Carretta, G. A. Timco, and R. E. P. Winpenny. Relaxation of muon spins in molecular nanomagnets. *Phys. Rev. B*, 81(14):140409, April 2010.

[126] A. J. Steele, T. Lancaster, S. J. Blundell, P. J. Baker, F. L. Pratt, C. Baines, M. M. Conner, H. I. Southerland, J. L. Manson, and J. A. Schlueter. Magnetic order in quasi-two-dimensional molecular magnets investigated with muon-spin relaxation. *Phys. Rev. B*, 84(6):1–21, August 2011.

[127] A. I. Larkin and A. A. Varmalov. Fluctuation Phenomena in Superconductors. In K. H. Bennenmann and J. B. Ketterson, editors, *Superconductivity*, chapter 10. Springer-Verlag, Berlin, 2008.

[128] A. V. Chubukov, D. Pines, and J. Schmalian. A Spin Fluctuation Model for d-Wave Superconductivity. In K. Bennenmann and J. Ketterson, editors, *Superconductivity*, chapter 22. Springer-Verlag, Berlin, 2008.

[129] M. Vojta. Cuprate superconductivity: Magnetic fluctuations revealed. *Nature Phys.*, 7(9):674–675, September 2011.

[130] M.-S. Nam, C. Mézière, P. Batail, L. Zorina, S. Simonov, and A. Ardavan. Superconducting fluctuations in organic molecular metals enhanced by Mott criticality. *Sci. Rep.*, 3:3390, January 2013.

[131] J. D. Wright, M. J. Pitcher, W. Trevelyan-Thomas, T. Lancaster, P. J. Baker, F. L. Pratt, S. J. Clarke, and S. J. Blundell. Magnetic fluctuations and spin freezing in nonsuperconducting LiFeAs derivatives. *Phys. Rev. B*, 88(6):060401(R), August 2013.

[132] V. P. S. Awana, I. Nowik, Anand Pal, K. Yamaura, E. Takayama-Muromachi, and I. Felner. Magnetic phase transitions in SmCoAsO. *Phys. Rev. B*, 81(21):212501, June 2010.

[133] B. J. Farrington. *A Tale of Two Spins: Electron Spin Centre Assemblies with N@C_{60} for use in QIP*. PhD thesis, University of Oxford, 2013.

[134] B. Goedde, N. Weiden, and K.-P. Dinse. Light-induced release of nitrogen from fullerene cages. *AIP Conference Proceedings*, 486:144–147, 1999.

[135] G. Liu, A. N. Khlobystov, A. Ardavan, G. A. D. Briggs, and K. Porfyrakis. Photochemical stability of N@C_{60} and its pyrrolidine derivatives. *Chemical Physics Letters*, 508(4-6):187–190, 2011.

[136] B. J. Farrington, T. J. Hingston, G. A. D. Briggs, M. R. Sambrook, and K. Porfyrakis. Photostability of N@C_{60} in common solvents. *ECS Transactions*, 35(25):113–117, 2011.

[137] T. Almeida Murphy, Th. Pawlik, A. Weidinger, M. Höhne, R. Alcala, and J.-M. Spaeth. Observation of Atomlike Nitrogen in Nitrogen-Implanted Solid C_{60}. *Phys. Rev. Lett.*, 77(6):1075–1078, 1996.

[138] J. Zhang, J. J.L. Morton, M. R. Sambrook, K. Porfyrakis, A. Ardavan, and G. A. D. Briggs. The effects of a pyrrolidine functional group on the magnetic properties of N@C_{60}. *Chem. Phys. Lett.*, 432(4-6):523–527, December 2006.

[139] R. M. Brown, Y. Ito, J. H. Warner, A. Ardavan, H. Shinohara, G. A. D. Briggs, and J. J. L. Morton. Electron spin coherence in metallofullerenes: Y, Sc, and La@C_{82}. *Phys. Rev. B*, 82(3):033410, July 2010.

[140] S. H. Baek, M. Luban, A. Lascialfari, E. Micotti, Y. Furukawa, F. Borsa, J. Van Slageren, and A. Cornia. Scaling behavior of the proton spin-lattice relaxation rate in antiferromagnetic molecular rings. *Phys. Rev. B*, 70(13):1–5, 2004.

[141] A. D. Milov, A. B. Ponomarev, and Yu. D. Tsvetkov. Electron-electron double resonance in electron spin echo: Model biradical systems and the sensitized photolysis of decalin. *Chemical Physics Letters*, 110(1):67–72, 1984.

[142] M. Pannier, S. Veit, A. Godt, G. Jeschke, and H. W. Spiess. Dead-time free measurement of dipole-dipole interactions between electron spins. *Journal of magnetic resonance (San Diego, Calif. : 1997)*, 142(2):331–340, 2000.

[143] O. Schiemann and T. F. Prisner. Long-range distance determinations in biomacromolecules by EPR spectroscopy. *Quarterly reviews of biophysics*, 40(1):1–53, 2007.

[144] G. Jeschke. DEER distance measurements on proteins. *Annu. Rev. Phys. Chem.*, 63:419–46, January 2012.

[145] G. Jeschke and Y. Polyhach. Distance measurements on spin-labelled biomacromolecules by pulsed electron paramagnetic resonance. *Physical chemistry chemical physics : PCCP*, 9(16):1895–1910, 2007.

[146] A. Ardavan, A. Bowen, A. Fernandez, A. Fielding, D. Kaminski, F. Moro, C. A. Muryn, M. D. Wise, A. Ruggi, E. J. L. McInnes, K. Severin, G. A. Timco, C. R. Timmel, F. Tuna, G. F. S. Whitehead, and R. E. P. Winpenny. Engineering coherent interactions in molecular nanomagnet dimers. *Submitted*, 2015.

[147] T. B. Faust, V. Bellini, A. Candini, S. Carretta, G. Lorusso, D. R. Allan, L. Carthy, D. Collison, R. J. Docherty, J. Kenyon, J. MacHin, E. J. L. McInnes, C. A. Muryn, H. Nowell, R. G. Pritchard, S. J. Teat, G. A. Timco, F. Tuna, G. F. S. Whitehead, W. Wernsdorfer, M. Affronte, and R. E. P. Winpenny. Chemical control of spin propagation between heterometallic rings. *Chemistry - A European Journal*, 17(50):14020–14030, 2011.

[148] J. E. Lovett, B. W. Lovett, and J. Harmer. DEER-Stitch: Combining three- and four-pulse DEER measurements for high sensitivity, deadtime free data. *Journal of Magnetic Resonance*, 223:98–106, 2012.

[149] G. Jeschke, V. Chechik, P. Ionita, A. Godt, H. Zimmermann, J. Banham, C. R. Timmel, D. Hilger, and H. Jung. DeerAnalysis2006 - a comprehensive software package for analyzing pulsed ELDOR data. *Appl.*, 30:473–498, 2006.

[150] D. Bruss and C. Macchiavello. Optimal eavesdropping in cryptography with three-dimensional quantum states. *Physical review letters*, 88(12):127901, 2002.

[151] N. J. Cerf, M. Bourennane, A. Karlsson, and N. Gisin. Security of quantum key distribution using d-level systems. *Physical review letters*, 88(12):127902, 2002.

[152] A. Klimov, R. Guzmán, J. Retamal, and C. Saavedra. Qutrit quantum computer with trapped ions. *Phys. Rev. A*, 67(6):062313, June 2003.

[153] D. Mc Hugh and J. Twamley. Trapped-ion qutrit spin molecule quantum computer. *New Journal of Physics*, 7:174–174, August 2005.

[154] L. Bartůšková, A. Černoch, R. Filip, J. Fiurášek, J. Soubusta, and M. Dušek. Optical implementation of the encoding of two qubits to a single qutrit. *Phys. Rev. A*, 74(2):022325, August 2006.

[155] B. P. Lanyon, M. Barbieri, M. P. Almeida, T. Jennewein, T. C. Ralph, K. J. Resch, G. J. Pryde, J. L. O'Brien, A. Gilchrist, and A. G. White. Simplifying quantum logic using higher-dimensional Hilbert spaces. *Nature Phys.*, 5(2):134–140, December 2008.

[156] V. E. Zobov and V. P. Shauro. On Time Optimal NMR Control of States of Qutrits Represented by Quadrupole Nuclei with the Spin $I = 1$. *J. Exp. Theor. Phys.*, 113(2):181–191, 2011.

[157] S. Takahashi, J. Van Tol, C. C. Beedle, D. N. Hendrickson, L. C. Brunel, and M. S. Sherwin. Coherent manipulation and decoherence of $S = 10$ single-molecule magnets. *Physical Review Letters*, 102(8):1–4, 2009.

[158] S. Takahashi, I. S. Tupitsyn, J. van Tol, C. C. Beedle, D. N. Hendrickson, and P. C. E. Stamp. Decoherence in crystals of quantum molecular magnets. *Nature*, 476(7358):76–79, 2011.

[159] F. Moro, D. Kaminski, F. Tuna, G. F. S. Whitehead, G. A. Timco, D. Collison, R. E. P. Winpenny, A. Ardavan, and E. J. L. McInnes. Coherent electron spin manipulation in a dilute oriented ensemble of molecular nanomagnets: pulsed EPR on doped single crystals. *Chem. Commun. (Cambridge, U.K.)*, 50(1):91–3, November 2014.

[160] G. Mitrikas, Y. Sanakis, C. P. Raptopoulou, G. Kordas, and G. Papavassiliou. Electron spin-lattice and spin-spin relaxation study of a trinuclear iron(III) complex and its relevance in quantum computing. *Physical chemistry chemical physics: PCCP*, 10(5):743–748, 2008.

[161] C. Schlegel, J. Van Slageren, M. Manoli, E. K. Brechin, and M. Dressel. Direct observation of quantum coherence in single-molecule magnets. *Physical Review Letters*, 101(14):1–4, 2008.

[162] S. Bertaina, S. Gambarelli, T. Mitra, B. Tsukerblat, A. Müller, and B. Barbara. Quantum oscillations in a molecular magnet. *Nature (London)*, 453(7192):203–6, May 2008.

[163] H. Morkoç and Ü. Özgüy. *ZnO: Fundamentals, Materials and Device Technology.* WILEY-VCH Verlag GmbH & Co., 2009.

[164] A. Hausmann and H. Huppertz. Paramagnetic resonance of ZnO:Mn^{++} single crystals. *J. Phys. Chem. Solids*, 29(8):1369–1375, August 1968.

[165] E. Knill, I. Chuang, and R. Laflamme. Effective Pure States for Bulk Quantum Computation. *Phys. Rev. A*, 57(5):24, 1998.

[166] M. D. Wise, A. Ruggi, M. Pascu, R. Scopelliti, and K. Severin. Clathrochelate-based bipyridyl ligands of nanoscale dimensions: easy-to-access building blocks for supramolecular chemistry. *Chemical Science*, 4(4):1658, 2013.